ETH zürich QUDEV

Semester Report

Improving Infrared-Blocking Microwave Filters

Graham J. Norris

October 2, 2017

Supervisor: Dr. Sebastian Krinner

Principal Investigator: Prof. Dr. Andreas Wallraff

Current Filter Specifications

There is currently one final filter design: the Low-Frequency Threaded End-Fill Eccosorb Filter (LF-TE). This filter is available in different lengths to tune the attenuation for various applications (*e.g.* to use it for high-frequency drive lines). However, due to the type of Eccosorb that we have, it is only impedance-matched at low frequencies (below 1 GHz), and is most suited for use in flux lines.

A typical example would be LF-TE10, which has an Eccosorb length of approximately 10 mm, pictured below in Figure 1. Physically, LF-TE10 has an outer-diameter of 8 mm and a length of 36 mm (including the connectors).

The typical room-temperature electrical performance of LF-TE10 from 0 GHz to 20 GHz is presented below in Figure 2. The reflected power as a function of frequency is plotted in blue; the predicted reflected power is plotted in gray; and the transmitted power is plotted in red and orange. The reflected power beats theoretical expectations, always remaining below −9 dB, and, for frequencies below 1 GHz, remaining below −20 dB. Attenuation increases linearly at 4.3 dB GHz^{-1}, reaching 60 dB at 14 GHz. Attenuation is around 0.5 dB at 500 MHz and 20 dB at 5 GHz. More information on LF-TE10 can be found in section 3.1.4.

A second design, HF-TE, is planned for when we acquire a second type of Eccosorb that allows for impedance-matching in the 5 GHz to 8 GHz range.

Figure 1: Image of current low-frequency filter (LF-TE10 04). Body length of 15.0 mm, total length of 36 mm.

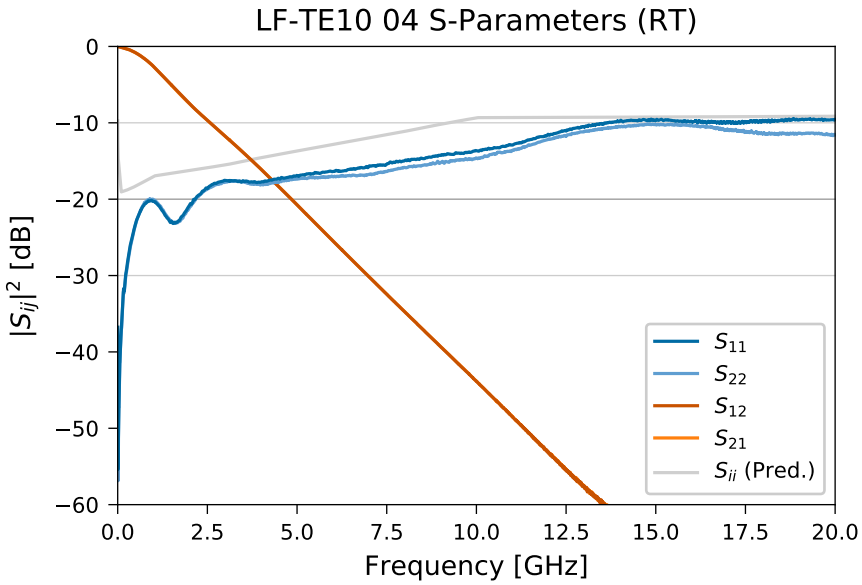

Figure 2: Room-temperature scattering parameters of LF-TE10 04 from 0 GHz to 20 GHz at room temperature. Reflected power plotted in blue and light-blue; predicted reflected power plotted in gray; transmitted power plotted in red and orange.

Contents

List of Figures

List of Tables

Acknowledgements

I thank Sebastian, Philipp, Paul, Simone, Johannes, and Yves for helpful discussions and answering my plentiful questions. Adrian generously taught me how to use the 4 K cryostat and dipstick. Melvin, Raphael, Karl, and Janis were indispensable for their advice and help in realizing the tangible components of this project.

Chapter 1

Introduction

1.1 Purpose of Infrared-Photon Blocking Filters

Superconducting quantum circuits, where many electrons collectively exhibit macroscopic quantum behavior, are extremely sensitive to environmental perturbations [1]. One of these environmental perturbations is due to *quasiparticles*—broken Cooper pairs—in the superconductor, created by photons with energies above the energy gap of the superconductor (2Δ in BCS theory) [2]. These quasiparticles may reduce the coherence time—roughly speaking, the time for which an object preserves quantum-mechanical properties like energy excitation or superposition—of our superconducting quantum circuits, limiting our ability to use them for quantum computation or simulation.

To protect the quantum circuit from environmental disturbances, we use extensive filtration on all cables that connect the quantum circuit to classical devices (such as microwave pulse generators and measurement equipment). In particular, to reduce the number of quasiparticles in the superconductor, we can use low-pass infrared-photon blocking filters, which I will discuss in this Report.

The exact effect of quasiparticles on the coherence times of superconducting quantum circuits, and in particular, the effect on the sort of quantum circuit that we utilize—the transmon quantum bit (qubit)—is contested in the literature. In the larger superconducting quantum circuit community, Kreikebaum *et al.* found that, without photon-blocking metal cans around their sample below the 2.7 K stage of their dilution refrigerator, the quality factor of their Al (but not their TiN) resonators was reduced, an effect they attributed to quasiparticles producted by infrared photons [6]. Barends *et al.* showed that stray infrared light inside the sample area of their dilution refrigerator limited the resonator quality factor that they could achieve [7]. For capacitively shunted flux qubits, both Birenbaum and Yan *et al.* claim that quasiparticles are the predominant limiting factor on coherence times of this qubit design [8, 9]. Risté *et al.* investigated the timescales of

quasiparticle tunneling in transmon qubits and found them to be on the order of one millisecond, meaning that quasiparticles are not the limiting factor for transmon qubits with coherence times on the order of tens of microseconds [3]. Sun *et al.* report that, while they could not claim that quasiparticles were the dominant source of decoherence for their qubits, their estimates of the quasiparticle tunneling rate would limit transmon qubits to coherence times of approximately 100 µs [4]. Catelani *et al.* studied the issue of quasiparticle relaxation theoretically and found that, in order to reproduce experimental parameters, either thermal quasiparticles are not limiting coherence times, or the quasiparticles are non-equilibrium in nature (either due to the quasiparticle population beging driven externally, or due to the sample being an order of magnitude warmer than expected) [5].

Based on the above information reported in the literature, it is not clear whether infrared-photon blocking filters for coaxial lines are needed for our qubits. However, such filters can also be used to fulfill other requirements, such as attenuation and thermalization of the input signal. Typical experimental setups have approximately 60 dB of attenuation from the microwave sources to the sample, broken up into several stages of attenuation at successively lower temperature stages in the dilution refrigerator. Vion *et al.* have done extensive calculations on the optimal amount of attenuation depending on the sample and filter temperatures [10]. This attenuation allows us to operate the microwave sources in a power regime where the desired signal dominates over other noise in the source, such as Johnson–Nyquist noise, and reduces the signal to a level appropriate for the circuit [11]. These attenuation stages also help to thermalize the blackbody radiation that is present in the coaxial lines; each attenuator can be thought of as a beam splitter that transmits some fraction of the incoming signal while adding the remaining fraction of unity of noise photons at the temperature of the attenuator [12, p. 31].

1.2 Previous Infrared-Photon Blocking Filters

Aluminum and niobium, common superconductors used in our circuits, have superconducting energy gaps of 3.5×10^{-4} eV and 30.5×10^{-4} eV, respectively, corresponding to frequencies of 82 GHz and 737 GHz [2]. Frequencies this high are difficult to reach with LC or other lumped-element filters as small stray capacitances or inductances cause such filters to become transparent at higher frequencies. Fortunately, infrared-blocking filters are needed in other fields studying cryogenic physics, and suitable designs have been found.

Bladh *et al.* list many of the relevant historical designs for cryogenic, infrared-photon blocking filters [13]. Importantly, powder filters, a predecessor of current filters, containing a spiraling central conductor surrounded by

fine copper or stainless steel powder, were first mentioned in the context of superconducting quantum systems by Martinis *et al.* [11]. Epoxy was sometimes added to improve thermal conductivity and seal the filter, and Wollack *et al.* demonstrated a mixture of stainless steel particles and epoxy with a thermal expansion coefficient that matches metals like copper or aluminum [14]. Santavicca and Prober switched to commercial magnetically loaded dielectric materials produced by Emerson & Cuming Microwave Products (now Laird Technologies, Inc.) [15]. These magnetically loaded, high-loss dielectrics go under the brand name ECCOSORB® (henceforth referred to as Eccosorb), and they come in several different types, depending on the magnetic material and support matrix. In 2015, Fang demonstrated the use of Eccosorb CR in the production of high-performance, high-density filter blocks designed for attenuating and thermalizing many coaxial lines simultaneously [16].

1.3 Previous Infrared-Photon Blocking Filters in the Quantum Device Laboratory

Eccosorb was initially investigated in the Qudev lab by Michael Peterer in the form of coatings for the sample holder to reduce infrared radiation [17]. Available information points to the next use of Eccosorb being infrared-photon blocking filters by Mintu Mondal and Yves Salathé [18]. As is common when designing such filters [16], two variants were produced: one version for the flux bias lines (that I shall refer to as *low-frequency*, since the frequency range of interest is lower, from 0 MHz to 500 MHz); and a second version for the microwave drive lines (which I shall call *high-frequency*, since the frequency range of interest is higher, approximately from 4 GHz to 8 GHz). These filters featured sub-miniature series A (SMA) connectors, for easy integration with existing coaxial lines and other microwave filters.

Figure 1.1: Mintu/Yves low-frequency Eccosorb filter. Note that the left connector has completely broken off the filter but has been placed nearby for this image. Mechanical information about these filters can be found in Table 3.2.

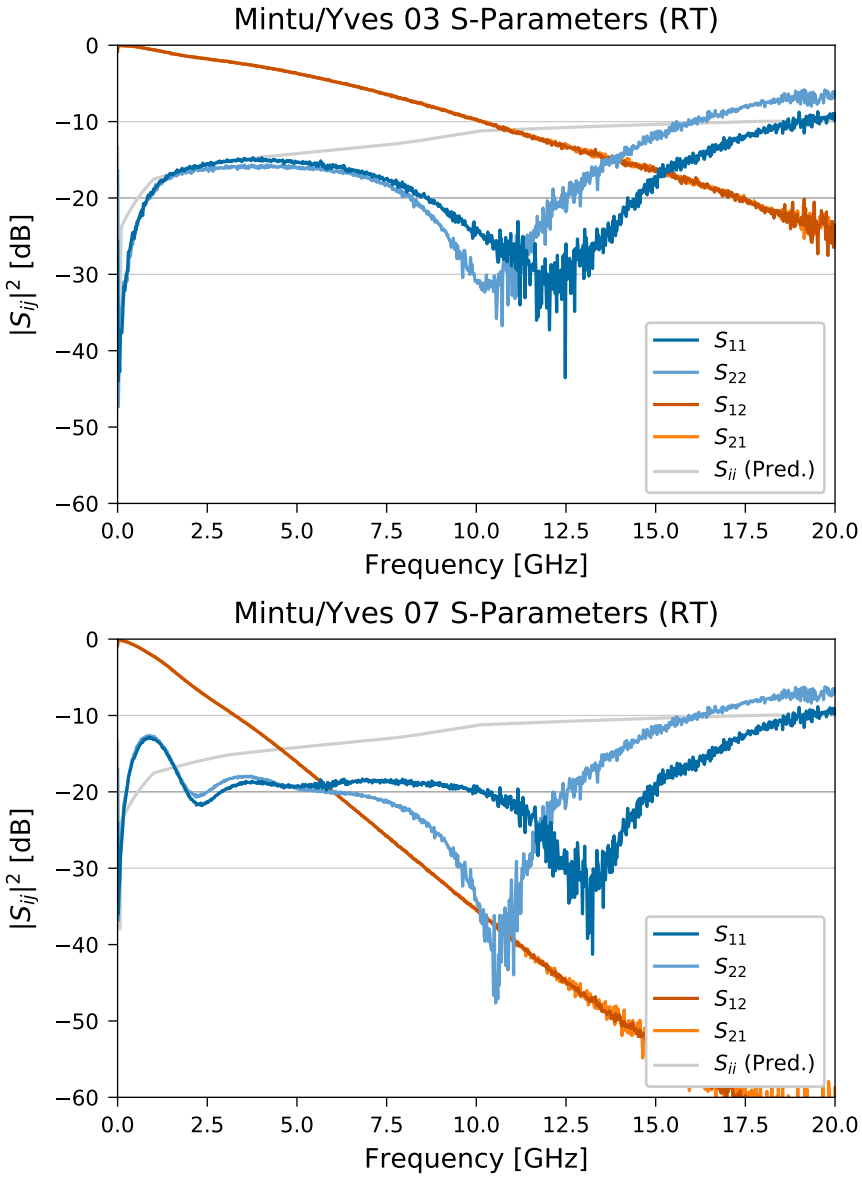

Figure 1.2: Room temperature scattering parameters S_{ij} of the Mintu/Yves filters plotted for frequencies from 0 GHz to 20 GHz. The blue lines are reflected power, $|S_{ii}|^2$; the gray line is the reflected power predicted by impedance calculations (see section 2.2); the orange-red lines are the transmitted power, $|S_{ij}|^2$. *Top*: filter designed for microwave drive-line. Eccosorb length of 3 mm *Bottom*: filter designed for flux-line. Eccosorb length of 7 mm.

The Mintu/Yves filter design is pictured above in Figure 1.1. These filters offered satisfactory electrical performance (see Figure 1.2) and were largely consistent between different samples. However, as evident in Figure 1.1, this design means that the soldered joint experiences strain every time a connector is attached or removed, inevitably resulting in gross mechanical failure of the filter.

1.4 Goals

With previous filter designs, both within the Qudev group and elsewhere in mind, it is now possible to state the goals for this project. Replacements for both the low-frequency and high-frequency filters are required that will show sufficient attenuation of infrared-photons without unduly attenuating the relevant signals. These filters should have the lowest possible reflected power ($|S_{ii}|^2$), should show consistent electrical performance, and should have good mechanical strength. Ideally, the filters would be easy to manufacture and small because future experiments with larger number of qubits will require more control lines and space inside the dilution refrigerator is limited.

Chapter 2

Designing Eccosorb Filters

2.1 Computing Scattering Parameters for Coaxial Filters

2.1.1 Impedance

The *characteristic impedance* of a transmission line is given by the following equation [19, p. 50]:

$$Z \equiv \sqrt{\frac{R + i\omega L}{G + i\omega C}} \tag{2.1}$$

where R is the resistance of the line per unit length, L is the series inductance of the line per unit length, G is the conductance of the line per unit length, C is the series capacitance of the line per unit length, $i \equiv \sqrt{-1}$ is the imaginary unit, and ω is the angular frequency $\omega = 2\pi\nu$. For a coaxial line with complex permittivity $\epsilon = \epsilon' - i\epsilon''$, permeability μ, surface resistance R_s, and an outer conductor of inner radius b and an inner conductor with an outer radius of a, these parameters are [19, p. 54]:

$$\begin{aligned} R &= \frac{R_s}{2\pi}\left(\frac{1}{a} + \frac{1}{b}\right) \\ L &= \frac{\mu}{2\pi}\log\left(\frac{b}{a}\right) \\ G &= \frac{2\pi\omega\epsilon''}{\log\left(\frac{b}{a}\right)} \\ C &= \frac{2\pi\epsilon'}{\log\left(\frac{b}{a}\right)} \end{aligned} \tag{2.2}$$

where log denotes the standard logarithm with base e.

Plugging Equation 2.2 into Equation 2.1 and simplifying in the high-frequency limit, where $i\omega L \gg R$ and $i\omega C \gg G$, yields the following characteristic impedance for a coaxial line of possibly complex permittivity, ϵ^*, and

possibly complex permeability, μ^*[1]:

$$Z = \frac{1}{2\pi}\sqrt{\frac{\mu^*}{\epsilon^*}}\log\left(\frac{b}{a}\right). \tag{2.3}$$

For a system with complex permittivity $\epsilon^* = \epsilon_0(\epsilon_r' - i\epsilon_r'')$ and complex permeability $\mu^* = \mu_0(\mu_r' - i\mu_r'')$, we may write Equation 2.3 in terms of real and imaginary components of the relative permittivity and permeability

$$Z = \frac{Z_0}{2\pi}\sqrt{\frac{\mu_r' - i\mu_r''}{\epsilon_r' - i\epsilon_r''}}\log\left(\frac{b}{a}\right), \tag{2.4}$$

where Z_0 is the impedance of the vacuum $\sqrt{\frac{\mu_0}{\epsilon_0}} \approx 377\,\Omega$. Alternatively, defining the *magnetic loss tangent* as $\tan(\delta_m) \equiv \frac{\mu_r''}{\mu_r'}$ and the *dielectric loss tangent* as $\tan(\delta_e) \equiv \frac{\epsilon_r''}{\epsilon_r'}$, we may write:

$$Z = \frac{Z_0}{2\pi}\sqrt{\frac{\mu_r'[1 - i\tan(\delta_m)]}{\epsilon_r'[1 - i\tan(\delta_e)]}}\log\left(\frac{b}{a}\right). \tag{2.5}$$

2.1.2 Scattering Parameters

The *voltage reflection coefficient*, or, more simply, *reflection coefficient*, Γ, of a transmission line is defined as [19, p. 57]:

$$\Gamma = \frac{V^+}{V^-} \tag{2.6}$$

where V^+ is the amplitude of the incident voltage and V^- is the amplitude of the reflected voltage. For a system of two connected transmission lines of different impedances (or a transmission line connected to a coaxial filter), this can be reformulated as [19, p. 62]

$$\Gamma = \frac{Z - Z_c}{Z + Z_c} \tag{2.7}$$

where Z is the impedance of the connected device or load, and Z_c is the characteristic impedance of the feed transmission line. In this context, *return loss* is defined as [19, p. 58]

$$\text{Return Loss [dB]} = -10\log_{10}(|\Gamma|^2) = -20\log_{10}(|\Gamma|)$$

which is measured in decibels (dB). However, in order to facilitate easier plotting with other parameters, I will define *return gain* (or *reflected power*) as

$$\text{Reflected Power [dB]} = 20\log_{10}(|\Gamma|). \tag{2.8}$$

[1]Note that * in this case does not denote complex conjugation but is simply a label to distinguish a complex permittivity or permeability from a real permittivity or permeability

The *scattering matrix* or S matrix of a system of N ports is defined as [19, p. 178]:

$$\begin{bmatrix} V_1^- \\ V_2^- \\ \vdots \\ V_N^- \end{bmatrix} = \begin{bmatrix} S_{11} & S_{12} & \cdots & S_{1N} \\ S_{21} & S_{22} & \cdots & S_{2N} \\ \vdots & \vdots & \ddots & \vdots \\ S_{N1} & S_{N2} & \cdots & S_{NN} \end{bmatrix} \begin{bmatrix} V_1^+ \\ V_2^+ \\ \vdots \\ V_N^+ \end{bmatrix} \tag{2.9}$$

where V_i^- is the amplitude of reflected voltage at port i and V_i^+ is the amplitude of the incident voltage at port i. Comparing Equation 2.9 and Equation 2.6 reveals that each S_{ii} is equivalent to Γ for port i. However, we also have terms S_{ij} with $i \neq j$ which correspond to *transmission coefficients* from port i to port j:

$$S_{ij} = \frac{V_i^-}{V_j^+}.$$

These transmission coefficients may also be reformulated as *attenuations* for signals travelling from port i to port j through

$$\text{Attenuation [dB]} = -20 \log_{10} \left(|S_{ij}| \right).$$

Transmitted power has the same form as the above equation, but without the minus sign.

More generally, the magnitude of the scattering matrix elements, S_{ij}, also referred to as *S-parameters*, can be expressed in terms of decibels as

$$|S_{ij}|^2 \text{ [dB]} = 20 \log_{10} \left(|S_{ij}| \right). \tag{2.10}$$

2.2 Computing Scattering Parameters for Different Grades of Eccosorb

Laird Technologies, Inc., the manufacturer of Eccosorb, produces technical bulletins for the different types of Eccosorb available that list the electromagnetic properties (real and imaginary components of permittivity and permeability, etc.) [20, 21]. Importantly, Equation 2.4 and Equation 2.5 match the equations in the guide Laird published about designing products using their electromagnetic data [22].

Combining Equation 2.5, Equation 2.7, and Equation 2.8, it is possible to compute the reflected power for different types of Eccosorb at different frequencies. Plots of the data provided by Laird are presented in Appendix D. Since these data are given only at select frequencies, linear interpolation of these data in linear frequency space was used when computing across continuous frequency ranges. This interpolation method was selected to provide a balance between avoiding assumptions about the form of the electromagnetic parameters, and physically reasonable interpolations of the data that would accurately predict performance.

As we have selected Eccosorb CR for our filters (which will be discussed in more detail in section 2.3), all of the plots below will refer to this type of Eccosorb or to Eccosorb MF as Laird states that the electromagnetic properties of each grade of Eccosorb CR are equivalent to the matching grade of Eccosorb MF (*e.g.* Eccosorb CR-110 has equivalent electromagnetic properties to Eccosorb MF-110).

2.2.1 Reflected Power as a Function of Cavity Size

As evident in Equation 2.3, one of the ways of achieving a good impedance match between a filter with given electromagnetic properties and the characteristic impedance of the coaxial lines to which the filter will be attached is to vary the outer-conductor inner-radius to center-conductor outer-radius ratio, referred to as the conductor radius ratio (CRR). However, the range of possible CRRs is limited by practical considerations. Many SMA microwave connectors are designed for a connector or hole diameter of between 200 mils and 210 mils (0.200 in to 0.210 in, 5.08 mm to 5.33 mm). As it is difficult to machine a solid filter body with a cavity that expands in the middle, this sets an upper limit on the inner diameter of the outer conductor. Center conductors smaller than 20 mils (0.51 mm) are available, but become more difficult to physically handle, setting a lower bound on the center conductor outer diameter. Thus, the attainable range of CRRs is approximately from 1 to 10.

Plots of reflected power versus CRR and frequency for the two chosen grades of Eccosorb are given in Figure 2.1 (More details as to why these grades were chosen are presented in section 2.3). Note that Eccosorb MF-110 shows a region of good impedance matching (where the reflected power is below −30 dB) from 4 GHz to 10 GHz at conductor radius ratios of around 4.2. Meanwhile, Eccosorb MF-124 shows worse impedance matching as there is only a small region with a reflected power of less than −20 dB from 0 GHz to 2 GHz at conductor radius ratios between 6 and 10. Similar plots for all grades of Eccosorb are available in section D.3. In general, only the "weaker" grades of Eccosorb (such as MF-110 and MF-112) can be properly impedance matched at practical conductor radius ratios, while the "stronger" grades (such as MF-124, MF-175, MF-190) can only be approximately impedance matched.

Plots of reflected power versus frequency at the "optimal" conductor radius ratio are presented in Figure 2.2 below. Optimal is this case means that the conductor radius ratio was selected to give the largest region of low reflected power. For MF-110, this optimal ratio was 4.2 and this leads to a calculated reflected power that is less than −30 dB from 2.5 GHz to 12.5 GHz. For MF-124, there is no practical conductor radius ratio that results in ideal impedance matching, however a CRR of approximately 8 results in a calculated reflected power that is generally less than −10 dB,

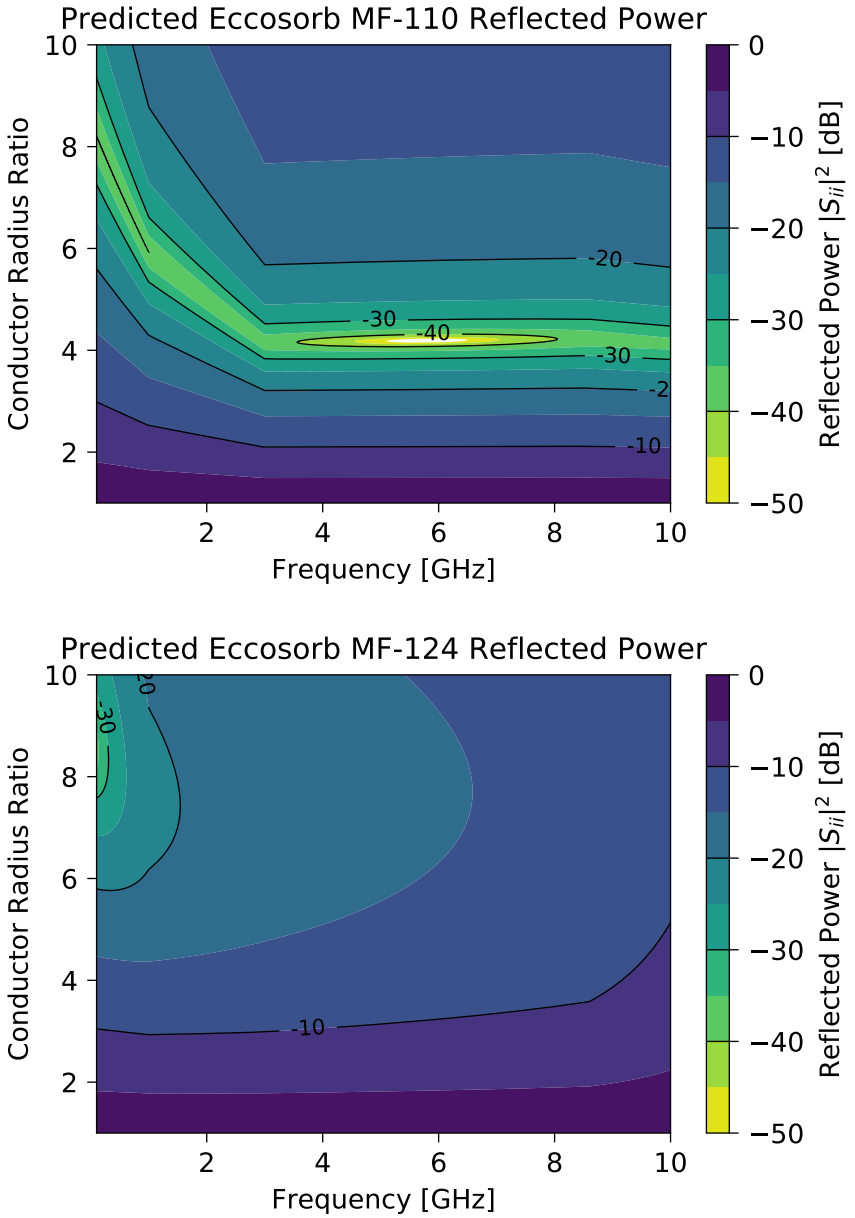

Figure 2.1: Predicted reflected power versus conductor radius ratio calculated for frequencies from 0 GHz to 10 GHz. Better performance indicated by lighter colors. *Top*: Eccosorb MF-110, which shows a region of good impedance matching (reflected power below −30 dB, green and yellow-green) from 4 GHz to 10 GHz at an outer conductor inner diameter to inner conductor outer diameter ratio of approximately 4.2. *Bottom*: Eccosorb MF-124, which shows a smaller region of impedance matching than MF-110, at conductor radius ratios between 8 and 10, and for frequencies below 1 GHz (green and blue-green region).

reaching below $-20\,\mathrm{dB}$ for frequencies below $1\,\mathrm{GHz}$. Similar plots for all grades of Eccosorb are presented in section D.4.

2.3 Eccosorb Selection

As our filter design involve filling cavities of arbitrary size, we need a castable microwave absorber. There are two Eccosorb products fitting this criterion: Eccosorb CR and Eccosorb CRS. Each grade of Eccosorb CRS is identical to the corresponding grade of MFS, as Eccosorb CR is identical to Eccosorb MF. Eccosorb MF shows a thermal expansion coefficient of $30 \times 10^{-6}\,\mathrm{K}^{-1}$ while Eccosorb MFS shows a thermal expansion coefficient of $63 \times 10^{-6}\,\mathrm{K}^{-1}$ [21, 23]. Thus, Eccosorb MF is better matched to copper, which has a thermal expansion coefficient of $16.6 \times 10^{-6}\,\mathrm{K}^{-1}$. Previous research in the Qudev lab by Michael Peterer indicated that this mismatch of expansion coefficients led to mechanical failure of Eccosorb CRS at low temperatures [17]. Eccosorb MF also shows better thermal conductivity than Eccosorb MFS, at $1.44\,\mathrm{W\,mK}^{-1}$ compared to $0.865\,\mathrm{W\,mK}^{-1}$, which is important if the filters are also used to thermalize the coaxial lines. For these reasons, we selected Eccosorb CR as the lossy dielectric in our infrared-blocking filters.

Since the Eccosorb must simultaneously block the maximum number of infrared photons in the 80 GHz range while allowing the desired signal to pass with as little disturbance as possible, it is important to choose the correct grade of Eccosorb MF (or CR) for each filter. The predicted attenuation per unit length of the different grades of Eccosorb MF are presented in Table 2.1. This table was prepared using the data in [21] along with linear interpolation of the data at the frequencies of interest. Attenuation increases with increasing grade number.

	Predicted Attenuation $[\mathrm{dB\,cm}^{-1}]$	
Grade	500 MHz	5 GHz
MF-110	0.046	0.881
MF-112	0.082	2.13
MF-114	0.288	5.27
MF-116	0.628	10.7
MF-117	1.39	23.5
MF-124	3.16	35.4
MF-175	4.31	38.6
MF-190	6.32	42.4

Table 2.1: Predicted attenuation per centimeter at 500 MHz and 5 GHz for different grades of Eccosorb MF.

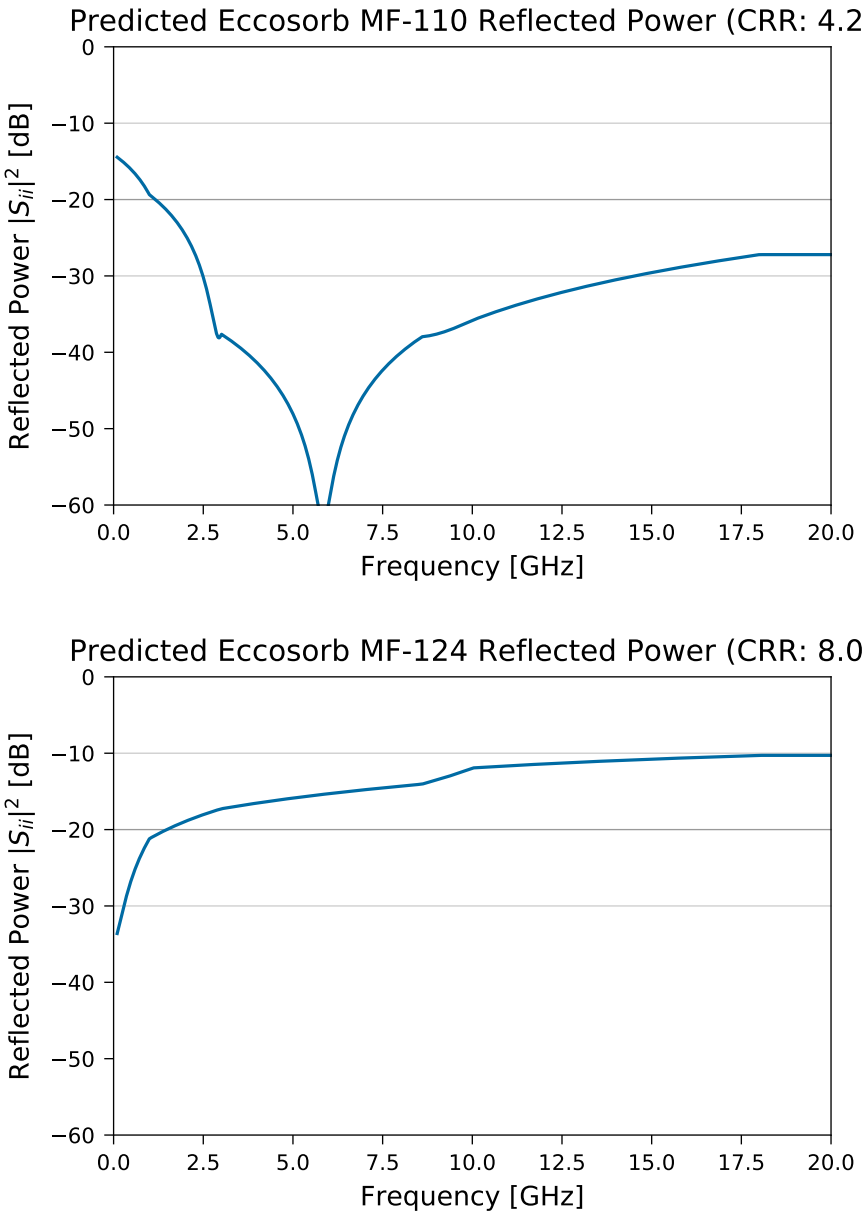

Figure 2.2: Predicted reflected power for frequencies from 0 GHz to 10 GHz at conductor radius ratios chosen to minimize reflected power. Better performance indicated by lower numbers. *Top*: Eccosorb MF-110 at a conductor radius ratio of 4.2. This combination shows excellent performance, with a calculated reflected power of less than −30 dB from 2.5 GHz to 12.5 GHz. *Bottom*: Eccosorb MF-124 at a conductor radius ratio of 8.0, although CRRs between 8.0 to 10 show fairly similar results. Performance is worse than MF-110, with reflected power less than −20 dB only for frequencies below approximately 1 GHz.

2.3.1 High-Frequency Filters

High-frequency filters must, in the frequency range of interest (approximately 4 GHz to 8 GHz), have low attenuation to avoid requiring higher drive powers that would lead to higher thermal loads on the fridge. Ideally, they would also have a flat frequency response, to avoid dephasing caused by attenuation of some drive frequencies more than others. At the same time, they should attenuate signals above 80 GHz by 60 dB or more to reduce quasiparticle populations. In addition to these attenuation properties, the filters should have a low reflection coefficient so that they do not contribute to standing waves that modify the local environmental impedance (or, equivalently, the environmental density of states) and generally complicate experimental efforts. Looking at Table 2.1, 2 dB of attenuation at 5 GHz in a filter with a length of approximately 1 cm means using either Eccosorb MF-110 or MF-112. However, MF-110 shows a region of extremely low reflected power between 4 GHz to 6 GHz while, for MF-112, this region is from 2 GHz to 4 GHz, which is less convenient for our experiments (see Figure D.6 and Figure D.7). CR-110 was also used by Fang and showed good performance [16]. Therefore, CR-110 was selected for the high-frequency filter designs.

2.3.2 Low-Frequency Filters

In our experiments, low-frequency Eccosorb filters are used in conjunction with LC low-pass filters with a cutoff frequency of 780 MHz (Mini-Circuits VLFX-780). However, as discusssed by Martinis, such filters become transparent at higher frequencies (in our case, approximately 20 GHz) due to stray capacitance in the filters [11]. Therefore, the low-frequency Eccosorb filters need to have low attenuation at 500 MHz, but otherwise should have the highest possible attenuation. Consulting Table 2.1, in order to achieve approximately 2 dB of attenuation at 500 MHz in a filter length of around 1 cm, either Eccosorb MF-117 or MF-124 would be suitable. As CR-124 was already used for previous filters and provided good performance (see Figure 1.2), we elected to use this for the low-frequency designs.

Chapter 3

Filter Specifications

Before I dive into the filter specifications, a brief note on the structure of the following chapters: In the following sections, I give the mechanical specifications of the different filters that were produced as a part of this Report, including some discussion of manufacturing difficulties and why different designs were tested. In chapter 4, I provide the electromagnetic measurements of all the filters and a discussion of the merits and faults of different versions. Finally, in chapter 5, I provide some more general discussion of the filter performance along with an outlook for future designs.

Naming Convention

All of the filters produced during this project have a name that describes the relevant properties and a unique serial number to distinguish them from other filters of the same type.

Table 3.1: Naming convention for filters

Frequency	-	Connector Type	Fill Type	Length	Number
LF, HF	-	F, P, T	S, E	03-36	01-99

I have given a breakdown of the naming scheme in Table 3.1. *Frequency* refers to the frequency range for which the filter is impedance-matched. This is largely a function of the type of Eccosorb used as a fill. All current designs are "LF" as with Eccosorb CR-124, the only type that we currently have, we can only achieve good impedance matching at low frequencies (below 1 GHz). In the future, once our Eccosorb CR-110 arrives, there will be "HF" models that are impedance-matched from 4 GHz to 8 GHz. This label does not, for example, preclude using LF filters for microwave drive lines, as long as the filter meets the desired specifications. *Connector type* refers to the type of connector (in particular, to how it connects to the filter body). Current filters use either flanged connectors ("F"), press-fit connectors ("P"), or threaded

connectors ("T"). *Fill type* refers to the method by which the filter is filled with Eccosorb. Side filling ("S") and end filling ("E") are the two methods used. *Length* refers to the Eccosorb fill length (in mm), to distinguish filters of the same overall design but with different attenuations (and hence lengths). Finally, *number* is a unique number within each filter type and length so that different examples of the same design can be distinguished. This number is placed after a space or on a separate line so that it can be distinguished from the length. All of these labels are also present on the filter body, with the addition of labels "α " and "β" to distinguish the two ports for measurement purposes.

As an example, a low-frequency (Eccosorb CR-124), flanged connector, side-fill filter with a length of 36 mm would be called LF-FS36, and the first two filters of this type would be LF-FS36 01 and LF-FS36 02.

3.1 Low-Frequency Filters

3.1.1 M/Y LF

Table 3.2: Mechanical properties of Mintu-Yves LF filter.

Property	**Value**
Body Size	6.0 mm Round
Body Material	OFHC Copper
Connectors	AEP Radiall 9402–1583–010 (Modified)
Connector Type	Solder
Center Conductor	0.085" Coaxial Cable Center Conductor
Center Conductor OD	0.51 mm
Cavity ID	4.2 mm
Conductor Radius Ratio	8.24
Dielectric Fill	Eccosorb CR-124
Fill Mode	Side Fill

The previous filter design in the QUDEV lab was due to Mintu and Yves. This design came in two variants: one shorter filter (body length of 5 mm and Eccosorb fill length of 2 mm) designed for use in microwave drive lines, and a longer filter (body length of 10 mm and fill length of 7 mm) designed for use in flux lines. The remaining mechanical parameters for this design are presented in Table 3.2 and an image of the longer variant is presented in Figure 1.1.

Figure 3.1: Image of LF-FS36 01. Body length of 36.0 mm.

Table 3.3: Mechanical properties of LF-FS36 filter.

Property	**Value**
Body Length	36 mm
Fill Length	36 mm
Body Size	12.0 mm Square
Body Material	OFHC Copper
Connectors	RND 205–00498 (Modified)
Connector Type	Flange-Mount
Center Conductor	Connectors
Center Conductor OD	1.3 mm
Cavity ID	5.1 mm
Conductor Radius Ratio	3.92
Dielectric Fill	Eccosorb CR-124
Fill Mode	Side Fill

3.1.2 LF-FS

The first filter produced as part of this project was a low-frequency, flanged connector, side-fill design—LF-FS, with the goal of testing connectors similar to those used by Fang [16] and determining if our Eccosorb still worked, three years after its stated expiration date. The chosen connectors were flange-mount SMA connectors with an extended dieletric (RND 205–00498), modified to remove the extra dielectric from the center conductor (see Figure 3.2). These connectors have a center-conductor outer-diameter of 1.3 mm and attach to the filter body with a small screw in each corner of the flange. This provides high mechanical strength, but means that the filters require more work to produce.

In order to use two of these connectors, the filter body is made out of 12 mm square oxygen-free high-conductivity (OFHC) copper (ordered from the ETH D-PHYS shop), with a length of 36.0 mm and an outer-conductor inner-diameter of 5.1 mm and a body length of 36.0 mm. In order to solder

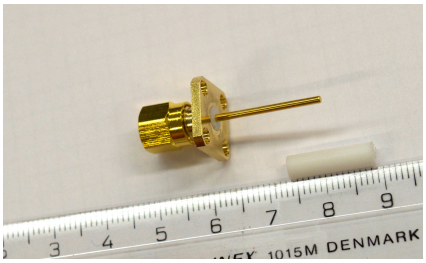

Figure 3.2: Modified RND 205–00498 for use in LF-FS filter. Extended dielectric (white) has been removed from the center conductor down to the flange of the filter.

the connectors together and fill the cavity with Eccosorb, a 5 mm hole was drilled from one face into the central cavity. This design results in an Eccosorb length of 36 mm, leading to the full name of this model: LF-FS36[1]), depicted in Figure 3.1.

With the ability to adjust the mounting of both connectors due to the flanges, it was easy to line up the two center conductors almost perfectly before soldering. Similarly, the large side hole made soldering and Eccosorb filling easy.

A destructive autopsy of LF-FS36 01 revealed that the Eccosorb completely filled the cavity, possibly with some smaller bubbles in the bulk Eccosorb (see Figure B.2). This matches nicely with my observation of average S-parameters (see Figure 4.1)

3.1.3 LF-PS

After LF-FS36 was tested to be working, the next step in replicating the work of Fang was to investigate press-fit connectors, leading to two LF-PS designs. These press-fit connectors should provide good mechanical strength, with the knurls on the press-fit section resisting torquing stresses, and also be easy to assemble (see Figure 3.4).

LF-PS36

The first variant, designed for flux-line use, featured extended center conductors (as in LF-FS36), resulting in the LF-PS36 filter (Figure 3.3 and Table 3.4). One of the only readily-available such connectors with an extended center conductor (and dielectric, which is removed) is Johnson model

[1] Formerly known as LF-A, being the first design produced.

Figure 3.3: Image of LF-PS36 01. Body length of 42.2 mm

Table 3.4: Mechanical properties of LF-PS36 filter.

Property	**Value**
Body Length	42.2 mm
Fill Length	35.8 mm
Body Size	8.0 mm Round
Body Material	OFHC Copper
Connectors	Johnson 142–1721–051 (Modified)
Connector Type	Press-Fit
Center Conductor	Connectors
Center Conductor OD	1.3 mm
Cavity ID	5.1 mm
Conductor Radius Ratio	3.92
Dielectric Fill	Eccosorb CR-124
Fill Mode	Side Fill

142–1721–051 (see Figure 3.4). As with the connectors in LF-FS, these connectors have a central-conductor outer-diameter of 1.3 mm.

Two of these connectors dictated a filter body with a length of 42.2 mm and a 5.1 mm central cavity diameter. The 5 mm side hole for soldering the central conductors and injecting the Eccosorb on LF-FS was felt to be excessive, so this was reduced to 3.0 mm for LF-PS. We also had concerns that the large hole could be reducing performance below the theoretical performance, although later COMSOL simulations indicated that the side hole is probably not an issue section C.2. As the press-fit connectors consume part of the filter length, the fill length is 35.8 mm, similar to LF-FS, leading to the model name LF-PS36.

During manufacturing, it was easy to insert one connector using a vise, but during the insertion of the second connector, the previously inserted connector would sometimes be pushed further into the filter body instead of the desired second connector. Additionally, for a narrow filter, it is difficult to precisely guide the central conductors to meet perfectly in the middle, and

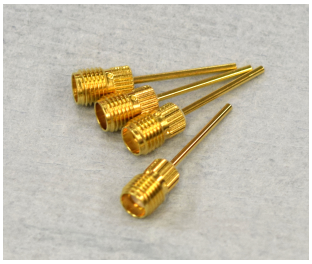

Figure 3.4: Modified RND 205–00498 for use in LF-FS filter. Extended dielectric (white) has been removed from the center conductor down to the flange of the filter.

in our case, the conductors ended up meeting side-on rather than head-on (see Figure 3.5). The 3 mm side hole meant that it was difficult to correct this issue. The small side hole also made Eccosorb filling extremely difficult.

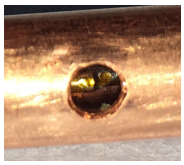

Figure 3.5: Misaligned center conductors on LF-PS36.

After this model showed poor S_{11} performance, a destructive autopsy of this filter model revealed that Eccosorb only partially filled the center cavity and confirmed that the center conductors did not meet head-on (see Figure B.3).

LF-PS03

Figure 3.6: Image of LF-PS03 01. Body length of 9.0 mm.

The second variant featuring press-fit connectors, LF-PS03, was designed for drive line use in parallel with LF-PS36 (see Figure 3.6). Delta RF model 1320–000–K911–32 connectors were used as these were available in

Table 3.5: Mechanical properties of LF-PS03 filter.

Property	**Value**
Body Length	9.0 mm
Fill Length	3.15 mm
Body Size	10.0 mm Round
Body Material	OFHC Copper
Connectors	Delta RF 1320–000–K911–32
Connector Type	Press-Fit
Center Conductor	Connector
Center Conductor OD	0.50 mm
Cavity ID	6.78 mm
Conductor Radius Ratio	13.56
Dielectric Fill	Eccosorb CR-124
Fill Mode	Side Fill

the QUDEV lab. The connectors dictate a cavity inner diameter of 6.78 mm and a total length of 9.0 mm. With a center pin diameter of 0.50 mm, these connectors result in a conductor radius ratio of 13.56. A 3.0 mm side hole was placed over the center of the filter for soldering and Eccosorb filling.

The hard stop present on the press-fit connectors solved the problem with LF-PS36, where the connector that was inserted first could be pushed past the ideal depth while inserting the second connector, and possibly helped to ensure that the central conductors were parallel with the body cavity. The center pins on each connector met perfectly end-to-end in the middle of the filter cavity, although this is largely due to the short length of the pins (see Figure 3.7).

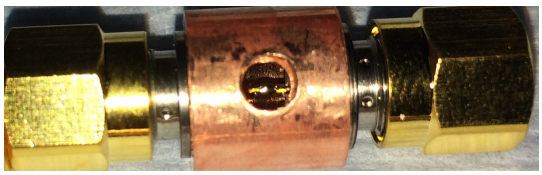

Figure 3.7: Aligned center conductors on LF-PS03.

Figure 3.8: Image of LF-TE35 01. Body length of 40.0 mm.

Table 3.6: Mechanical properties of LF-TE35 filter.

Property	**Value**
Body Length	40.0 mm
Fill Length	35.2 mm
Body Size	8.0 mm Round
Body Material	OFHC Copper
Connectors	RND 205–00500
Connector Type	Threaded
Center Conductor	Silver-Plated Copper Wire
Center Conductor OD	0.90 mm
Cavity ID	4.6 mm
Conductor Radius Ratio	5.11
Dielectric Fill	Eccosorb CR-124
Fill Mode	End Fill

3.1.4 LF-TE

LF-TE35

After the unsatisfactory performance of LF-PS, a new design was investigated. This model, LF-TE, replaced the push-fit connectors with threaded SMA female-to-female couplers (RND 205–00500) (see Figure 3.8). With these connectors, a separate center conductor with a diameter identical to that of a SMA male pin (between 0.902 mm and 0.940 mm). In this case, a flexible coaxial cable with a solid 0.90 mm silver-plated copper center conductor was used (Ceam M-17/84 RG223). In this design, the length was not fixed by connectors, but was selected to be convenient and have a fill length comparable with previous filters. The fill length in this case is only approximate, including the length of the body cavity and the 1.93 mm of space in the threaded couplers per the SMA standard. The threaded connectors allowed a maximum cavity size of 4.6 mm leading to a conductor radius ratio of 5.11.

Due to the necessity of threading the filters with the uncommon 1/4”–36 UNS 2B thread used by SMA connectors, this filter design was fabricated by the ETH central workshop from OFHC copper stock. Great care was taken when sizing the center conductor with this filter design. The conductor was initially longer than required and gradually shortened until both connectors could just barely thread to the stop. This ensured that the center conductor fully filled the connector at each end.

This design of filter also offered the advantage that the Eccosorb could be filled from one open side after a connector and the center conductor were inserted. This should eliminate partial filling problems as the center cavity is large and, with the filter vertical on the sealed end, gravity assists in filling the filter from the bottom up. This intuition was supported by good electrical performance (see Figure 4.6), and by an autopsy of the filter, which found only a small air bubble at the end from which Eccosorb was filled (see Figure B.4.

The mechanical strength of this design is quite good. Manually applying significant torque (greater than specified for making proper SMA connections) to the connectors with a 5.5 mm wrench and pliers deformed the flat sections on the coupler without the coupler unscrewing.

LF-TE10 01–03

Figure 3.9: Image of LF-TE10 01. Body length of 15.0 mm.

Table 3.7: Mechanical properties of LF-TE10 01–03 filters.

Property	**Value**
Body Length	15.0 mm
Fill Length	10.2 mm
Remaining	See Table 3.6

During the redesign of LF-PS36 into LF-TE35 using threaded SMA female-to-female couplers, LF-PS03 was redesigned to become LF-TE10, a shorter variant of LF-TE35 (see Figure 3.9). The body length of this filter was chosen to be a convenient length of 15.0 mm, leading to an estimated fill

length of 10.2 mm. The center conductor for this filter was prepared in the same way as for LF-TE35.

Although this filter was initially intended for microwave drive-line use, LF-TE10 01 was found to have sufficient attenuation for flux line use. Two additional filter bodies (LF-TE10 02 and 03) were produced. As bubble formation was observed in both Eccosorb and Stycast (see Appendix B), the Eccosorb was vacuum degassed for approximately two minutes after mixing but before injection into the filter bodies.

LF-TE10 04–

Figure 3.10: Image of LF-TE10 04. Body length of 15.0 mm.

Table 3.8: Mechanical properties of LF-TE10 04– filters.

Property	**Value**
Body Length	15.0 mm
Fill Length	10.2 mm
Connectors	Amphenol SMA7071A2-3GT50G-50
Remaining	See Table 3.6

The most recent variant of LF-TE10 is an updated version that uses larger SMA to SMA connectors that avoid the mechanical deformation issues of the RND connectors (see Figure 3.11). This is the current design that will be used for all future flux-line filters, and which can also be used as a microwave drive-line filter. Vacuum degassed Eccosorb was used for these filters.

After production, it was noticed that is was possible to partially unscrew one of the couplers (on the side that was initially facing down during Eccosorb filling) from the body, although unscrewing and re-attaching the coupler did not change the electrical performance. To fix this, filters from LF-TE10 06 and onwards use Loctite 290 threadlocker on the α port.

Figure 3.11: Comparison of threaded SMA female-female couplers. *Left*: RND 205–00500, *right*: Amphenol SMA7071A2-3GT50G-50. The Amphenol coupler has a larger flat section that is separated from the threads, making it easier to access with a wrench when the coupler is threaded into a filter body.

Figure 3.12: Image of LF-TE06 02. Body length of 10.0 mm.

LF-TE06

After the good performance of LF-TE10 01, and with the adoption of LF-TE10 as a flux-line filter, a shorter version was prepared to bring the attenuation in line with the ideal values for a high-frequency filter (see Figure 3.12). This model also features vacuum degassed Eccosorb.

Table 3.9: Mechanical properties of LF-TE06 filter.

Property	**Value**
Body Length	10.6 mm
Fill Length	5.8 mm
Remaining	See Table 3.6

Figure 3.13: Image of LF-TS35 01. Body length of 40.0 mm.

Table 3.10: Mechanical properties of LF-TS35 filter.

Property	**Value**
Body Length	40.0 mm
Fill Length	35.2 mm
Fill Mode	Side Fill
Remaining	See Table 3.6

3.1.5 LF-TS

LF-TS35

LF-TS35 is a variant of LF-TE35 that features two 3.0 mm side holes located 6.82 mm from the ends of the filter for Eccosorb filling (see Figure 3.13). This design was produced in parallel with LF-TE35 in case the end-fill mechanism was unsuccessful.

This filter does not have the same mechanical integrity of LF-TE35. It is possible to unscrew one of the end connectors, although this was not experienced during measurements of the filter, but rather when the strength of the filter was investigated.

LF-TS10

LF-TS10 is a side-fill variant of LF-TE10 01 that was contemplated but never produced, due to the good performance of LF-TE35 and LF-TE10 01 and the lackluster mechanical strength of LF-TE35. This design has only a single 3.0 mm fill hole centered in the filter body.

Table 3.11: Mechanical properties of HF-TE filter.

Property	**Value**
Body Size	8.0 mm Round
Body Material	OFHC Copper
Connectors	Amphenol SMA7071A2-3GT50G-50
Connector Type	Threaded
Center Conductor	SpC Wire
Center Conductor OD	0.90 mm
Cavity ID	3.8 mm
Conductor Radius Ratio	4.2
Dielectric Fill	Eccosorb CR-110
Fill Mode	End Fill

3.2 High-Frequency Filters

3.2.1 HF-TE

HF-TE is a planned filter for our Eccosorb CR-110 once it arrives. This filter is designed for use in microwave drive lines, and has a smaller conductor radius ratio to better match the Eccosorb CR-110 (see Figure 2.1). The length will have to be determined after attenuation measurements can be performed. All other properties should be identical to LF-TE10 06 (vacuum degassed Eccosorb, thread locker, *etc.*).

Chapter 4

Filter Measurements

4.1 VNA Parameters

All measurements below were performed on an Agilent N5230C Vector Network Analyzer (VNA) using the settings in Table 4.1 (except for the measurements of LF-FS36, where an unknown IF bandwidth was used). Prior to measuring the scattering parameters of LF-FS36, manual calibration was performed using a Rhode and Schwarz ZV-Z32 calibration kit. Before all later measurements, electronic calibration was performed using an Agilent N4433A electronic calibration module.

Table 4.1: VNA Settings

Property	**Value**
Frequency Range	300.0 kHz to 20.0 GHz
Sweep Points	5000
Power	−8.0 dBm
IF Bandwidth	10 kHz
Averaging Factor	50

4.2 Low-Frequency Filters

The measured attenuation and averaged return-loss for the different low-frequency filters are presented in Table 4.2. The temperature at which the measurement was performed is listed, with RT corresponding to room temperature (approximately 298 K) and LN_2 corresponding to liquid nitrogen temperature (approximately 77 K). The attenuation at the given frequencies was computed from the measured data using linear interpolation to get the attenuation at the exact frequencies listed. Return losses were averaged over the listed frequency ranges as reflected power ratios (*i.e.* $|S_{ij}|^2$) before

taking the logarithm to convert to decibels. This more accurately reflects the attenuation that a power source spread across those frequencies would experience. The frequency regions for averaging were selected to correspond to the useful regions for both low-frequency (flux line) and high-frequency (microwave drive line) use cases.

Table 4.2: Measured Attenuation and Return Loss for Low-Frequency Filters

		Attenuation [dB]		**Average Return Loss** [dB]	
Model	**T**	500 MHz	5 GHz	0 MHz to 780 MHz	4 GHz to 8 GHz
FS36 01	RT	2.14	67.2	18.3	9.61
FS36 01	LN_2	1.56	59.7	21.0	10.7
PS36 01	RT	0.846	41.4	19.1	5.85
PS36 02	RT	0.964	47.6	13.4	6.35
PS03 01	RT	0.340	8.13	17.2	14.6
PS03 02	RT	0.440	7.90	16.4	13.1
TE35 01	RT	2.86	63.0	24.5	19.1
TE10 01	RT	1.75	18.6	27.3	20.8
TE10 02	RT	1.25	25.2	7.95	15.5
TE10 03	RT	1.21	25.0	8.37	17.0
TE10 04	RT	0.832	20.7	24.5	16.6
TE10 05	RT	0.501	14.7	29.5	18.6
TE10 06	RT	0.964	24.8	18.2	14.5
TE10 07	RT	0.629	22.6	19.2	17.4
TE10 08	RT	1.11	28.3	17.7	13.8
TE10 09	RT	0.866	22.0	16.6	15.3
TE10 10	RT	0.952	25.0	18.7	16.1
TE10 11	RT	0.967	25.4	18.4	15.0
TE10 12	RT	0.876	23.4	18.9	16.8
TE10 13	RT	0.523	19.6	17.2	16.1
TE06 01	RT	0.449	11.3	27.5	17.0
TE06 02	RT	0.815	13.5	8.03	16.0
TS35 01	RT	2.30	51.0	22.1	20.4
M/Y 07	RT	0.853	16.1	16.3	19.4
M/Y 03	RT	0.194	3.68	24.8	16.4

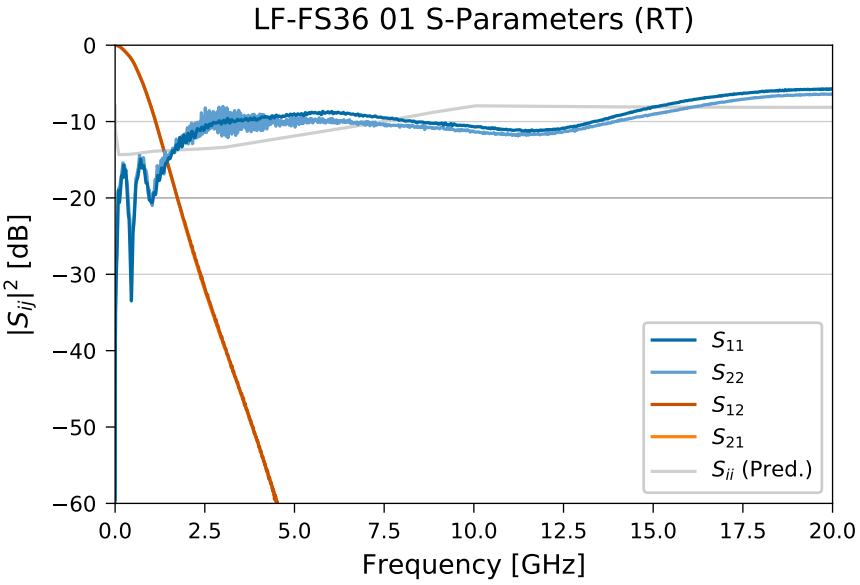

Figure 4.1: Room temperature scattering parameters, S_{ij}, of LF-FS36 01 from 300 kHz to 20 GHz. Reflected power plotted in blue, transmitted power plotted in red-orange, and theoretical reflected power prediction plotted in light gray.

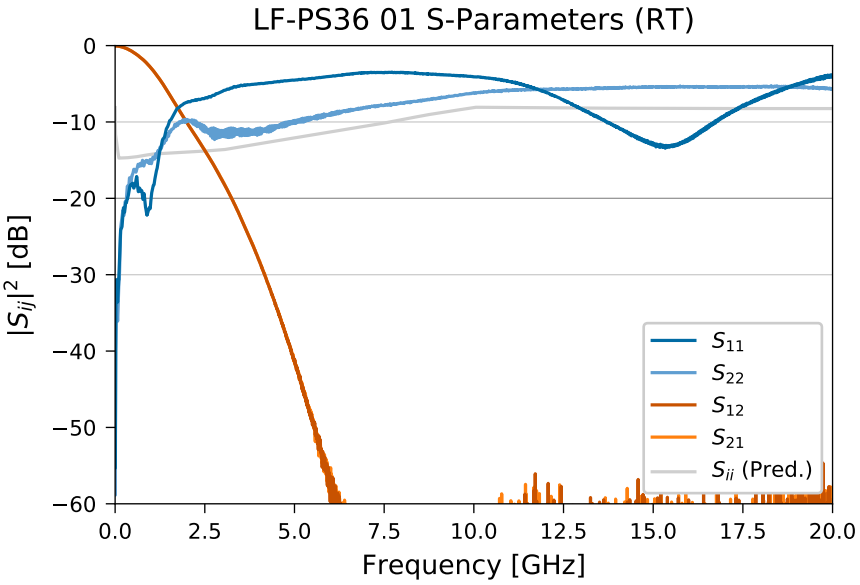

Figure 4.2: Room temperature scattering parameters, S_{ij}, of LF-PS36 01 from 300 kHz to 20 GHz. Reflected power plotted in blue, transmitted power plotted in red-orange, and theoretical reflected power prediction plotted in light gray.

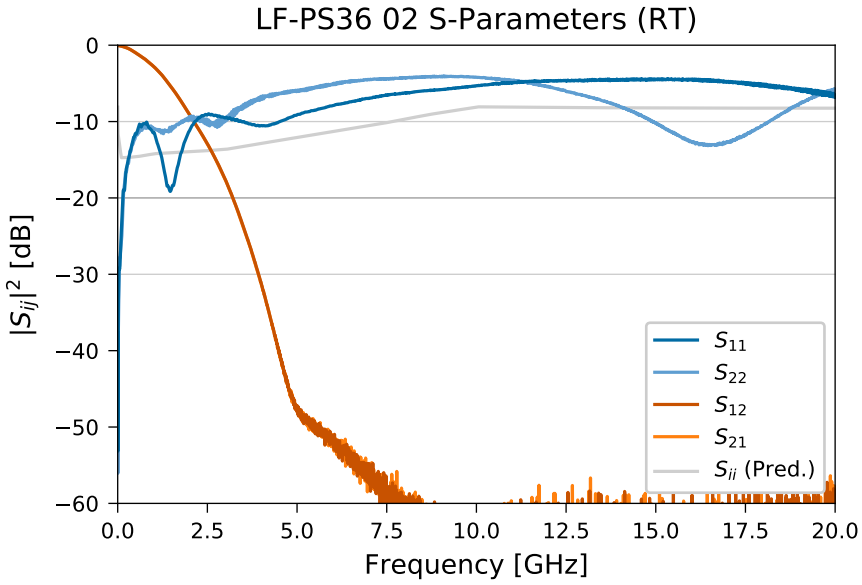

Figure 4.3: Room temperature scattering parameters, S_{ij}, of LF-PS36 02 from 300 kHz to 20 GHz. Reflected power plotted in blue, transmitted power plotted in red-orange, and theoretical reflected power prediction plotted in light gray.

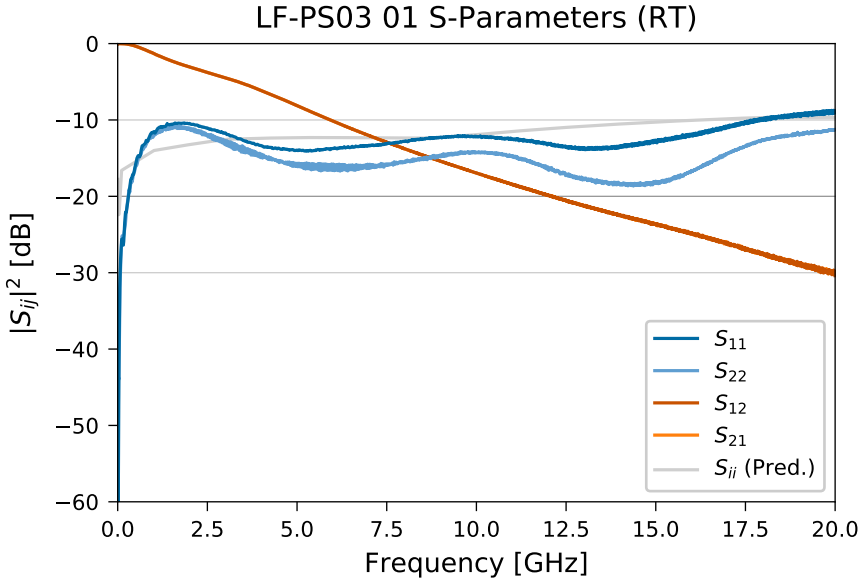

Figure 4.4: Room temperature scattering parameters, S_{ij}, of LF-PS03 01 from 300 kHz to 20 GHz. Reflected power plotted in blue, transmitted power plotted in red-orange, and theoretical reflected power prediction plotted in light gray.

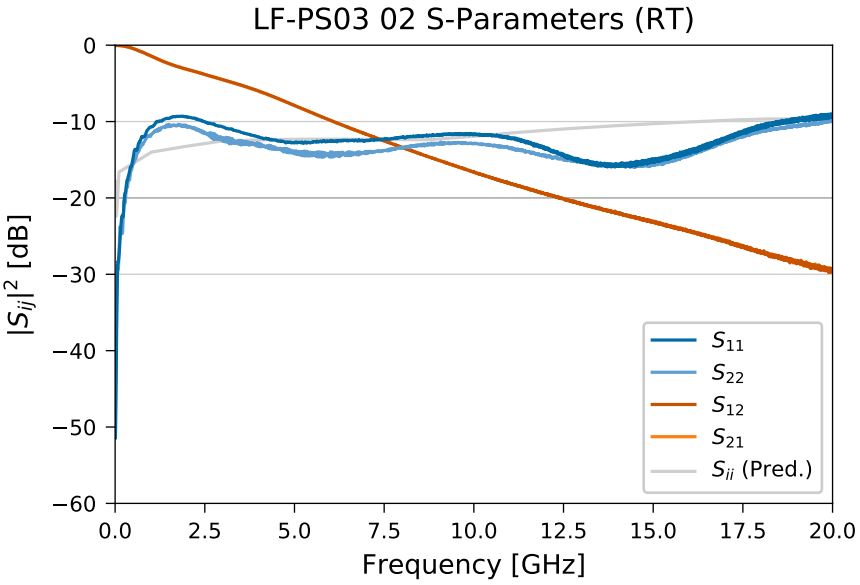

Figure 4.5: Room temperature scattering parameters, S_{ij}, of LF-PS03 02 from 300 kHz to 20 GHz. Reflected power plotted in blue, transmitted power plotted in red-orange, and theoretical reflected power prediction plotted in light gray.

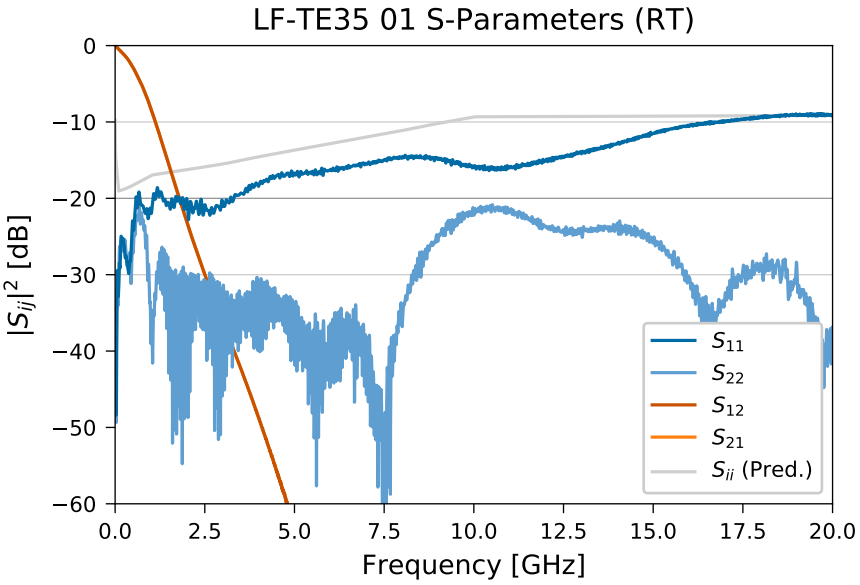

Figure 4.6: Room temperature scattering parameters, S_{ij}, of LF-TE35 01 from 300 kHz to 20 GHz. Reflected power plotted in blue, transmitted power plotted in red-orange, and theoretical reflected power prediction plotted in light gray.

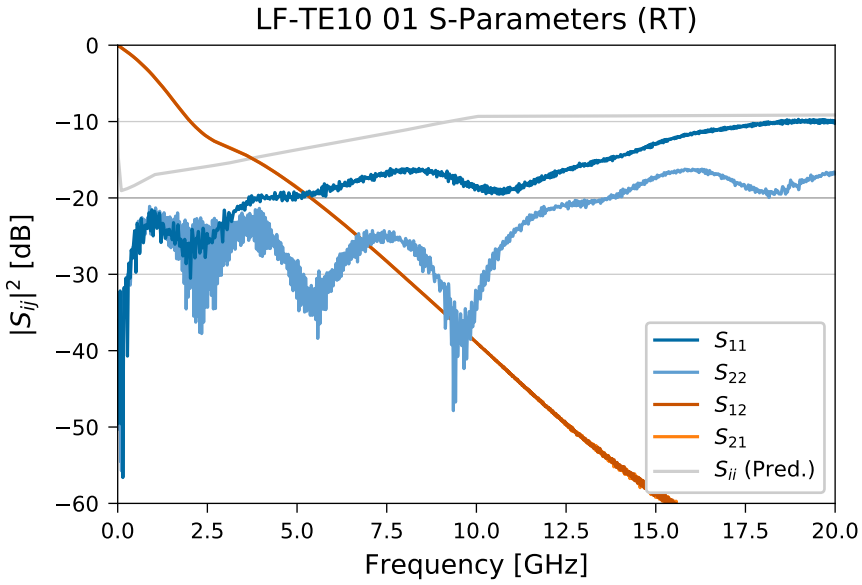

Figure 4.7: Room temperature scattering parameters, S_{ij}, of LF-TE10 01 from 300 kHz to 20 GHz. Reflected power plotted in blue, transmitted power plotted in red-orange, and theoretical reflected power prediction plotted in light gray.

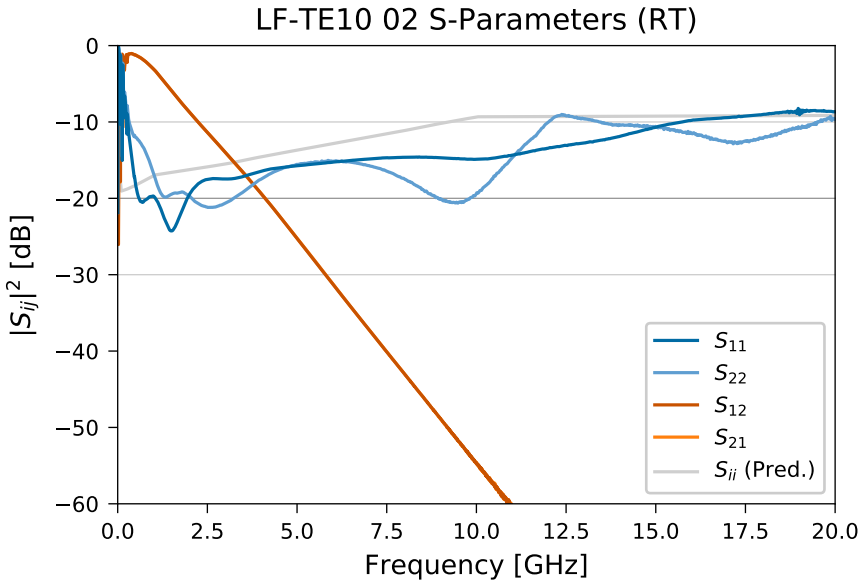

Figure 4.8: Room temperature scattering parameters, S_{ij}, of LF-TE10 02 from 300 kHz to 20 GHz. Reflected power plotted in blue, transmitted power plotted in red-orange, and theoretical reflected power prediction plotted in light gray.

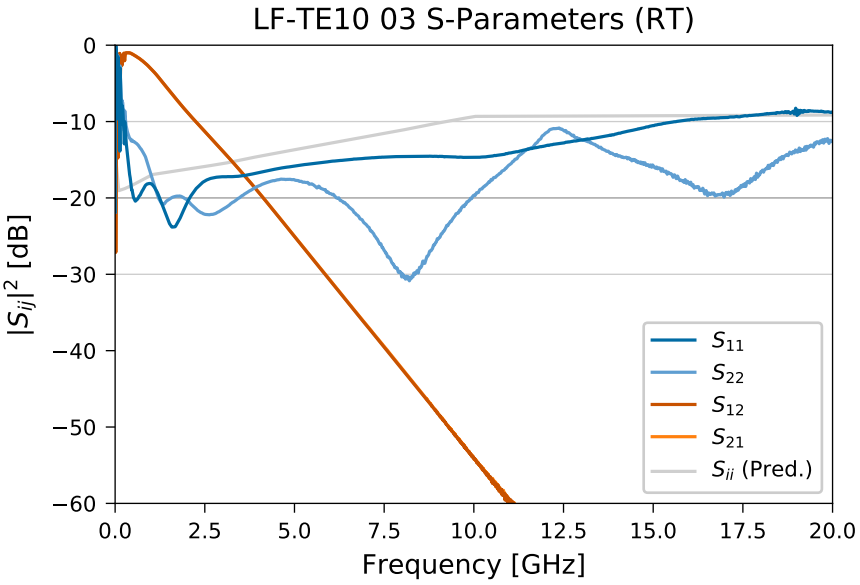

Figure 4.9: Room temperature scattering parameters, S_{ij}, of LF-TE10 03 from 300 kHz to 20 GHz. Reflected power plotted in blue, transmitted power plotted in red-orange, and theoretical reflected power prediction plotted in light gray.

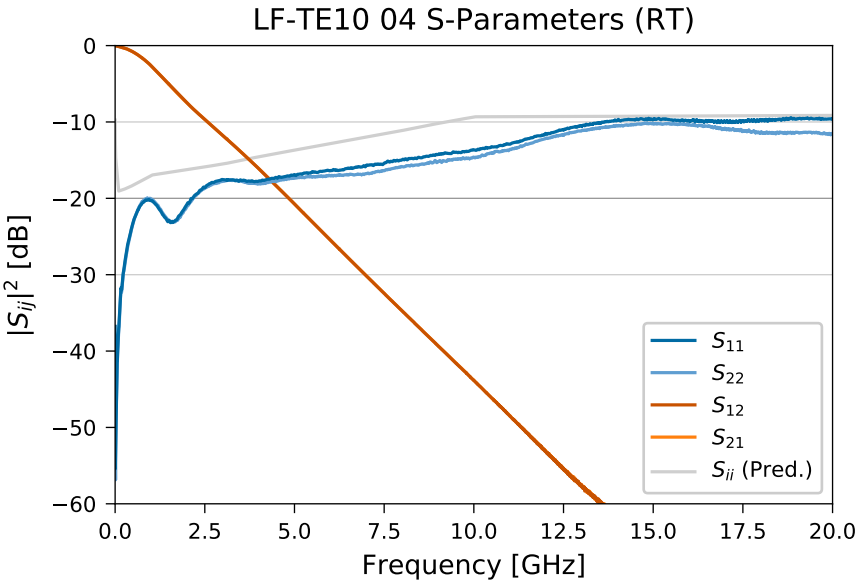

Figure 4.10: Room temperature scattering parameters, S_{ij}, of LF-TE10 04 from 300 kHz to 20 GHz. Reflected power plotted in blue, transmitted power plotted in red-orange, and theoretical reflected power prediction plotted in light gray.

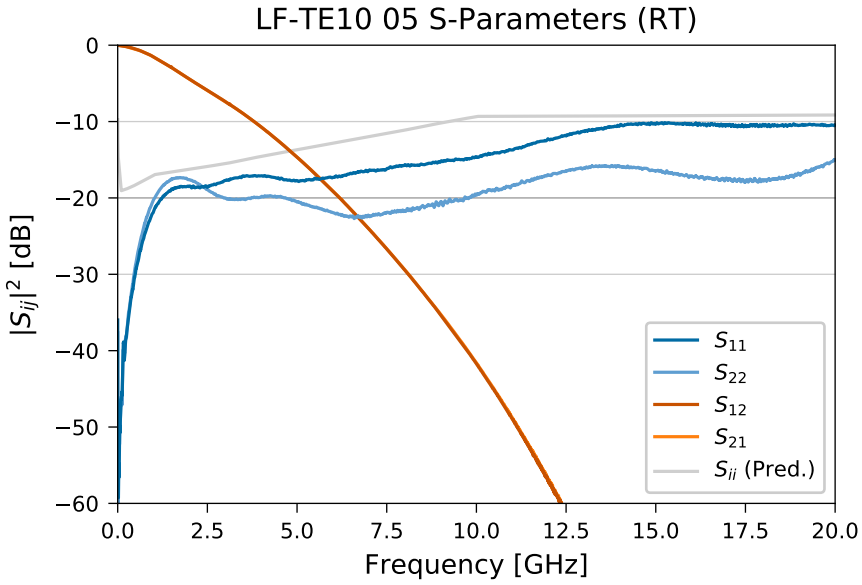

Figure 4.11: Room temperature scattering parameters, S_{ij}, of LF-TE10 05 from 300 kHz to 20 GHz. Reflected power plotted in blue, transmitted power plotted in red-orange, and theoretical reflected power prediction plotted in light gray.

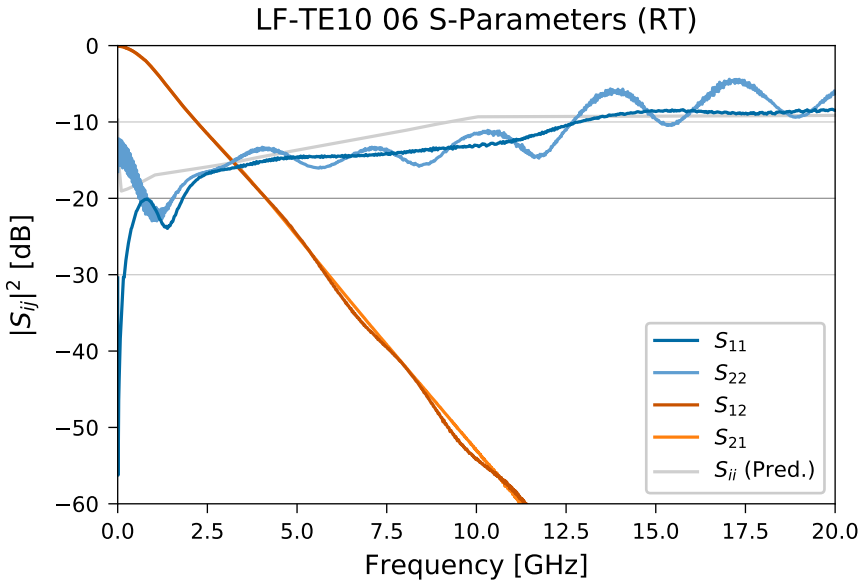

Figure 4.12: Room temperature scattering parameters, S_{ij}, of LF-TE10 06 from 300 kHz to 20 GHz. Reflected power plotted in blue, transmitted power plotted in red-orange, and theoretical reflected power prediction plotted in light gray.

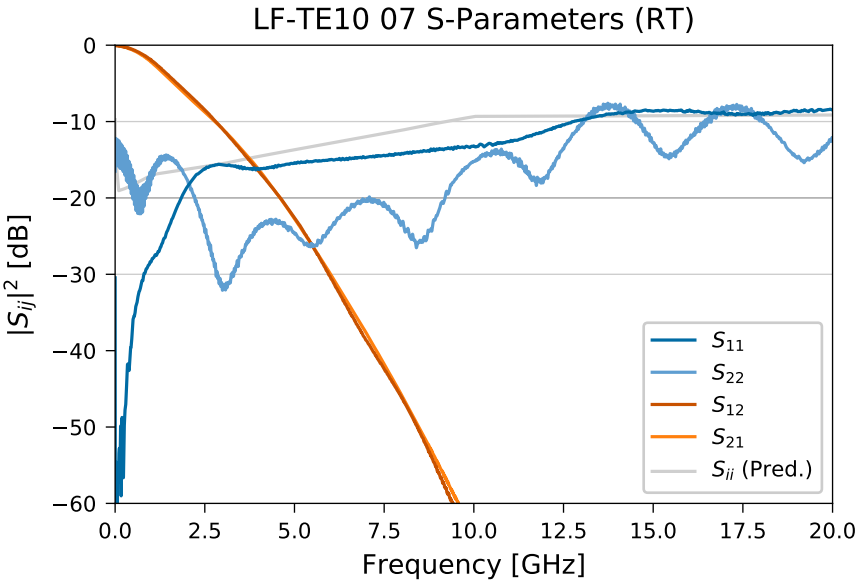

Figure 4.13: Room temperature scattering parameters, S_{ij}, of LF-TE10 07 from 300 kHz to 20 GHz. Reflected power plotted in blue, transmitted power plotted in red-orange, and theoretical reflected power prediction plotted in light gray.

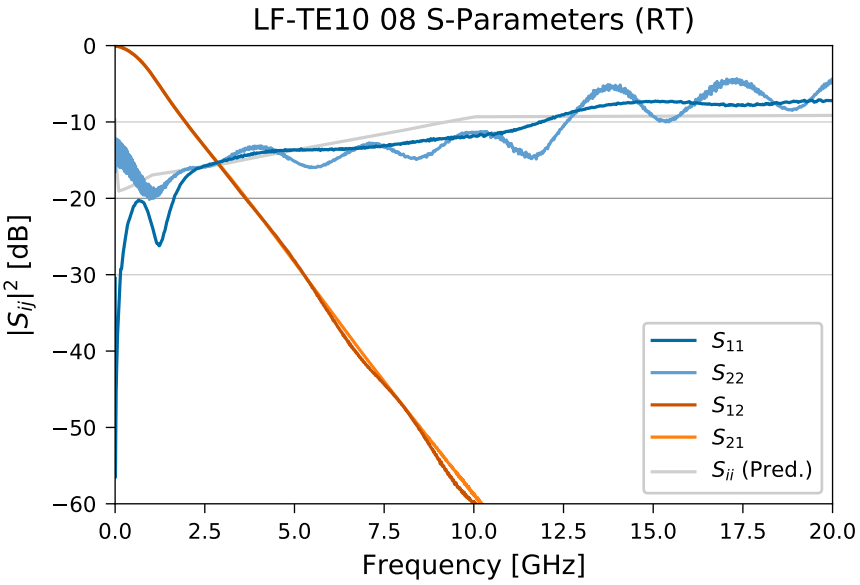

Figure 4.14: Room temperature scattering parameters, S_{ij}, of LF-TE10 08 from 300 kHz to 20 GHz. Reflected power plotted in blue, transmitted power plotted in red-orange, and theoretical reflected power prediction plotted in light gray.

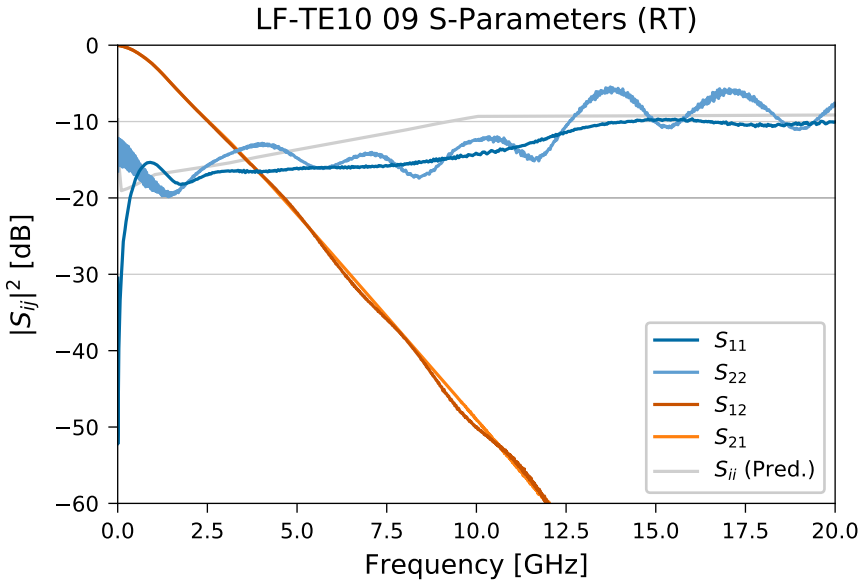

Figure 4.15: Room temperature scattering parameters, S_{ij}, of LF-TE10 09 from 300 kHz to 20 GHz. Reflected power plotted in blue, transmitted power plotted in red-orange, and theoretical reflected power prediction plotted in light gray.

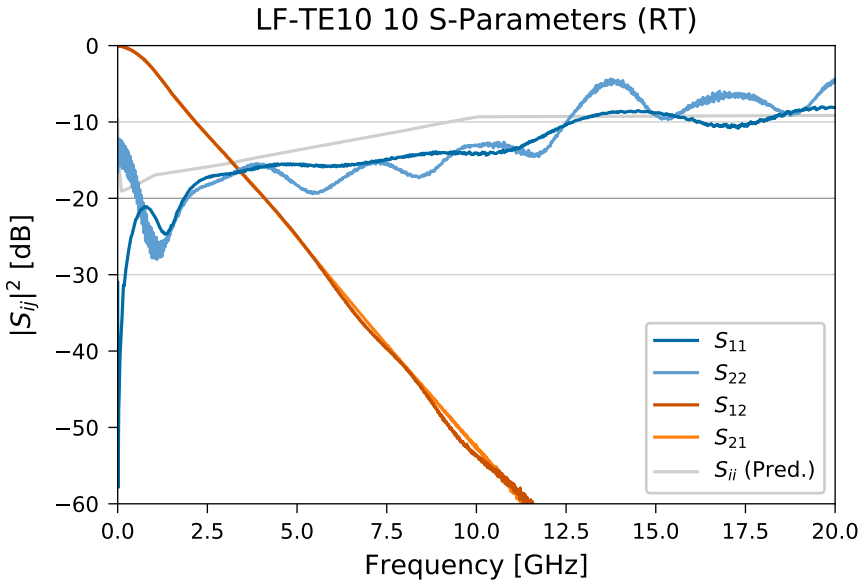

Figure 4.16: Room temperature scattering parameters, S_{ij}, of LF-TE10 10 from 300 kHz to 20 GHz. Reflected power plotted in blue, transmitted power plotted in red-orange, and theoretical reflected power prediction plotted in light gray.

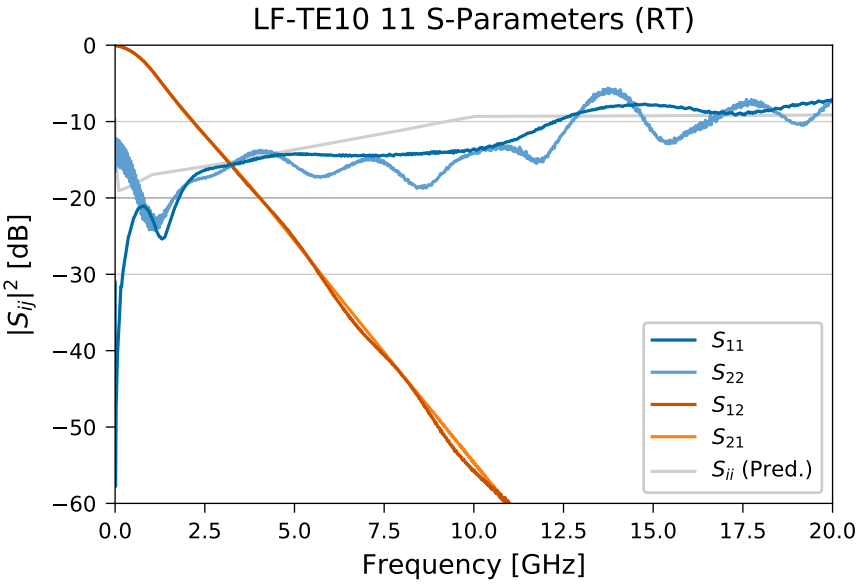

Figure 4.17: Room temperature scattering parameters, S_{ij}, of LF-TE10 11 from 300 kHz to 20 GHz. Reflected power plotted in blue, transmitted power plotted in red-orange, and theoretical reflected power prediction plotted in light gray.

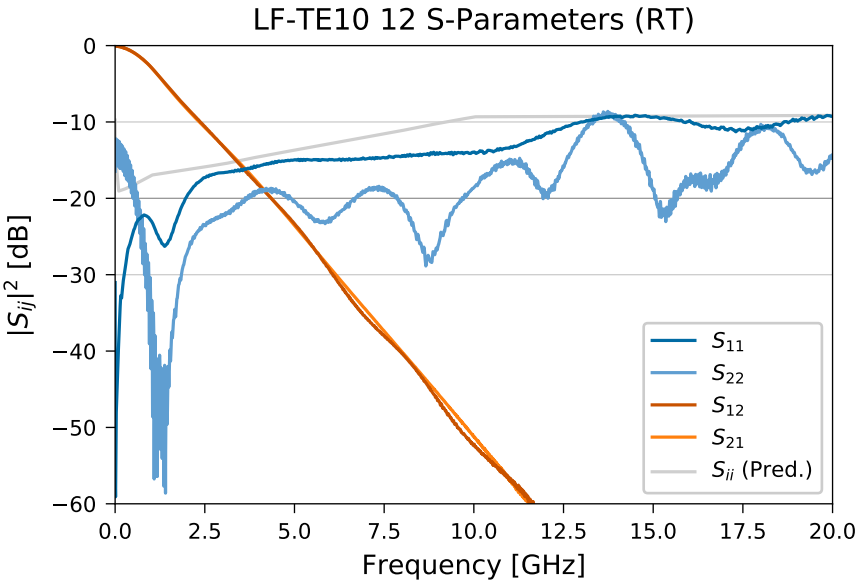

Figure 4.18: Room temperature scattering parameters, S_{ij}, of LF-TE10 12 from 300 kHz to 20 GHz. Reflected power plotted in blue, transmitted power plotted in red-orange, and theoretical reflected power prediction plotted in light gray.

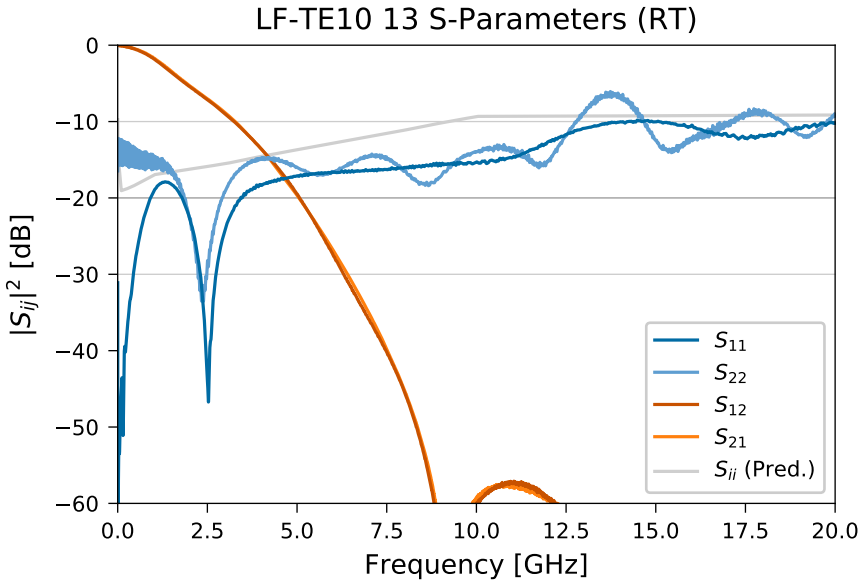

Figure 4.19: Room temperature scattering parameters, S_{ij}, of LF-TE10 13 from 300 kHz to 20 GHz. Reflected power plotted in blue, transmitted power plotted in red-orange, and theoretical reflected power prediction plotted in light gray.

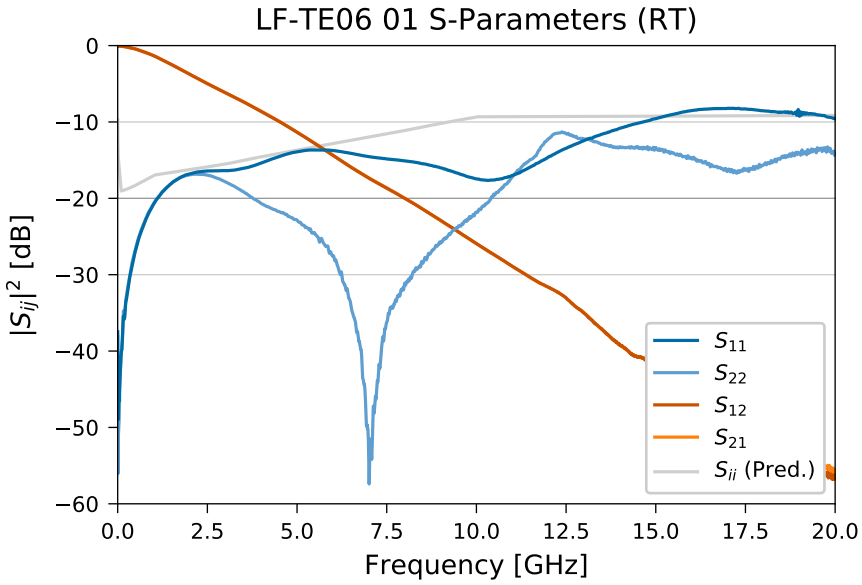

Figure 4.20: Room temperature scattering parameters, S_{ij}, of LF-TE06 01 from 300 kHz to 20 GHz. Reflected power plotted in blue, transmitted power plotted in red-orange, and theoretical reflected power prediction plotted in light gray.

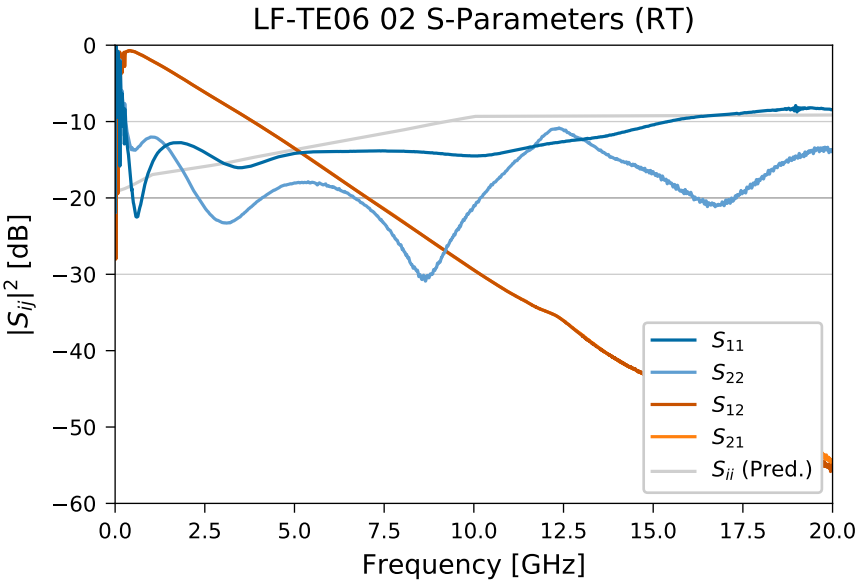

Figure 4.21: Room temperature scattering parameters, S_{ij}, of LF-TE06 02 from 300 kHz to 20 GHz. Reflected power plotted in blue, transmitted power plotted in red-orange, and theoretical reflected power prediction plotted in light gray.

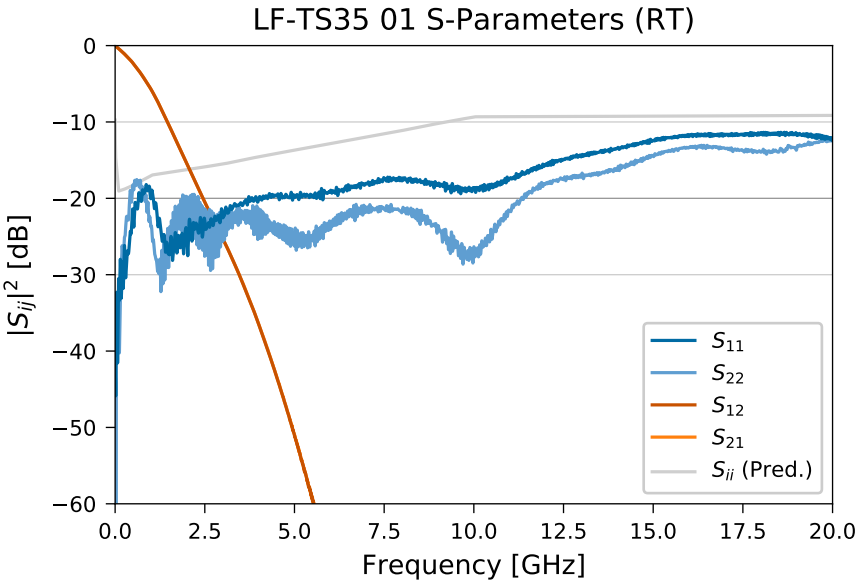

Figure 4.22: Room temperature scattering parameters, S_{ij}, of LF-TS35 01 from 300 kHz to 20 GHz. Reflected power plotted in blue, insertion gain plotted in red-orange, and theoretical reflected power prediction plotted in light gray.

4.3 Discussion

4.3.1 LF-FS

The scattering parameters of LF-FS36, plotted in Figure 4.1, reveal that our Eccosorb CR-110, despite being thre years past its state expiration date, still functions as expected and that the actual filters perform similarly to the theoretical expectations. This filter was thermally cycled down to liquid nitrogen temperatures and back to room temperature several times without any ill effects. Liquid nitrogen temperatures slightly reduced the attenuation and the average return loss.

4.3.2 LF-PS

LF-PS36

Both LF-PS36 01 (Figure 4.2) and LF-PS36 02 (Figure 4.3) display worse scattering parameters than LF-FS36 outside of very low frequencies. The reflected power across much of the spectrum is above the theoretical expectations, and there is an asymmetry between the two ports. In addition, both filters showed nonlinear behavior of the attenuation with changing frequency (*i.e.* attenuation does not increase in an approximately linear fashion with increasing frequency). At the very least, this design is consistently bad, with both filters showing similar performance.

The degraded performance (relative to LF-FS36) was initially blamed on central conductors that did not line up perfectly end-to-end during manufacturing, but an autopsy of LF-PS36 01 revealed that the Eccosorb did not fill the entire cavity, meaning that the filter is no longer even approximately impedance-matched to $50\,\Omega$ coaxial lines (see Appendix B).

LF-PS03

LF-PS03 01 (Figure 4.4) and LF-PS03 02 (Figure 4.5) show similar performance that is, unfortunately, not terribly better than that of LF-FS36. Compared to LF-PS36, the slope of the attenuation has increased, from approximately $-10\,\mathrm{dB\,GHz^{-1}}$ to $-1.5\,\mathrm{dB\,GHz^{-1}}$, as expected, given the shorter length of the filter. However, the reflected power performance, while slightly better than LF-PS36, is not great, averaging around $-13\,\mathrm{dB}$ across much of the spectrum. Both filters (01 and 02) show some asymmetry between the two ports.

4.3.3 LF-TE

LF-TE35

LF-TE35 01 (Figure 4.6) demonstrated the potential of the threaded coupler design with end-filling. The attenuation is similar to LF-FS36 and LF-PS36, which is expected given that they have similar lengths. However, the reflected power is significantly better than either of those designs, with both ports beating the theoretical expectations. Low-frequency performance is similar to the previous designs, with reflected power below $-20\,\mathrm{dB}$ up to around $1\,\mathrm{GHz}$ in both directions. One port has a reflected power that is below $-30\,\mathrm{dB}$ for almost the entire range between $2\,\mathrm{GHz}$ to $7.5\,\mathrm{GHz}$ and is *always* below $-20\,\mathrm{dB}$.

The cause for this super-theoretical performance was initially vexing. Swapping the cables in the VNA switched which port had better reflected power, so this is performance does not arise from an issue with one channel of the VNA. After the filter autopsies, a possible cause was revealed: LF-TE35 01 has an air bubble near one of the connectors (see Figure B.4). My records from that period were not detailed enough to distinguish exactly which side corresponded to which port on the VNA measurement, however, I suspect that this bubble acted as an impedance matching region, much like an anti-reflective coating in optics or the angled lossy attenuators used in waveguides. Unfortunately, this performance did not appear in other variants of the LF-TE filter, but this is one area where a larger-scale project might improve on this design.

LF-TE35 01 was thermally cycled down to liquid nitrogen temperatures and back to room temperature three times without significant change in the measured performance.

LF-TE10

LF-TE10 01 (Figure 4.7) shows similar performance to LF-TE35 01 (they were manufactured at the same time using the same procedures). The attenuation is lower than the longer designs, approximately $-4\,\mathrm{dB\,GHz^{-1}}$. The reflected power at both ports is consistently better than the theoretical prediction. Again, as with LF-TE35 01, there is asymmetry between the two ports, with one port showing better performance and some sort of resonance effect in the reflected power. The exact reasons for this are unclear, but I suspect either a bubble near the end of the filter, as with LF-TE35.

LF-TE10 02 (Figure 4.8) and 03 (Figure 4.9) show performance that is worse than the previous LF-TE10 filters. The filters both have linear attenuation slopes of approximately $-5.5\,\mathrm{dB\,GHz^{-1}}$, which is lower than the $-5\,\mathrm{dB\,GHz^{-1}}$ and $-4\,\mathrm{dB\,GHz^{-1}}$ of other LF-TE10s. For frequencies above $2\,\mathrm{GHz}$, the reflected power performance largely beats theoretical expectations. At low frequencies, however, these two filters show strange performance,

where the reflected power is rather large, starting at around 0 dB at 0 GHz and decreasing to −20 dB at around 2 GHz, rather than starting at better than −30 dB at very low frequencies. In addition to this, both filters show asymmetric reflected power, and one port shows some unusual peaking around 11 GHz.

While all of these features are strange and undesirable, they are consistent for the two filters, so this must come from some construction detail of the filters. The major change that I recall from LF-TE10 01 to 02 and 03 was that less effort was used in sizing the center conductors to be the full length of the cavity plus the couplers. However, there is no clear physical motivation for how an air gap in the back of the connector would increase the reflected power, given that the filters have DC conductivity. Therefore, the most plausible explanation is that there is some unfilled region. The other possible cause is a minor mistake in the Eccosorb recipe for these filters: 0.87 g of Part B was added instead of 0.78 g. Unfortunately, due to limited time, an autopsy was not performed on these filters.

LF-TE10 04 (Figure 4.10) and 05 (Figure 4.11) largely remedied the issues with LF-TE10 02 and 03. Both filters demonstrate good low-frequency reflected power, and in general beat the theoretical expectations across the spectrum. Attenuation is slightly reduced compared to LF-TE10 02 and 03, but is greater than LF-TE10 01 at approximately $-5\,\mathrm{dB\,GHz^{-1}}$. For filter 05, this attenuation is nonlinear with frequency, reducing the attenuation at low frequencies, but still reaches greater than −60 dB for frequencies above 12.5 GHz. LF-TE10 05 also displays some asymmetry between the two ports, and it is possible that this is linked to the nonlinear attenuation. It seems that with Eccosorb filters, although devices of the same design may perform similarly, there is still the possibility of minor variations.

LF-TE10 04 was thermally cycled to liquid nitrogen temperatures without any major change in electrical performance. In this case, the filter was also measured at 4 K temperatures in a liquid helium dipstick. The S-parameters at this temperature are presented in Figure 4.23, and a comparison of the attenuation at room temperature and 4 K is presented in Figure 4.24. A through coupler was measured at 4 K as a background for the attenuation. However, it was not possible to completely calibrate out the dipstick cables, so a direct comparison of the reflected power is not possible. At a minimum, the reflected power has not increased above the theoretical value for this design. The attenuation is reduced at low temperatures, going from approximately $-5.5\,\mathrm{dB\,GHz^{-1}}$ at room temperature to approximately $-4.8\,\mathrm{dB\,GHz^{-1}}$ at 4 K.

During this thermal cycling, I noticed that it was possible to unscrew one of the threaded couplers from the filter body. Unscrewing this as far as possible and then screwing it back on several times, I found no major changes in the scattering parameters. The difference between the initial and final S-parameters are presented below in Figure 4.25. The largest differences are

in the scattering parameters of port 1, which is the port that was targeted in this testing. At worst, these changes resulted in an additional 2 dB in reflected power and a slight decrease in attenuation at around 10 GHz. The large feature on the right is due to the attenuation reaching the noise floor of the VNA. In this sense, this filter design is very robust against mechanical damage.

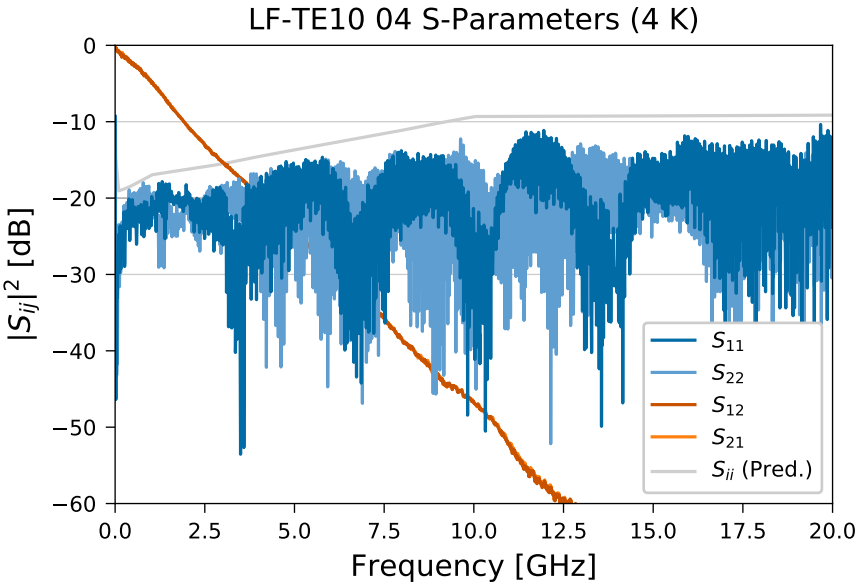

Figure 4.23: 4 K scattering parameters, S_{ij}, of LF-TE10 04 from 300 kHz to 20 GHz. Reflected power plotted in blue, transmitted power plotted in red-orange, and theoretical reflected power prediction plotted in light gray.

LF-TE10 06–13 (Figure 4.12 through Figure 4.19) demonstrate the variability of this design in mass production. In all of these plots, the oscillations in S_{22} are due to either an issue calibrating the VNA for the dipstick cables or the dipstick connectors themselves, as they are not present at room temperature or expected based on the simple nature of the filters. The filters still generally beat the theoretical expectation for reflected power.

LF-TE06

LF-TE06 01 (Figure 4.20) and 02 (Figure 4.21) are similar to LF-TE10 02 and 03, with the exception that LF-TE06 01 has good low-frequency performance on both ports and a region of good reflected-power performance on on port at around 7 GHz. The attenuation of this design is reduced to $-2.9\,\mathrm{dB\,GHz^{-1}}$. Both filters have asymmetries of between the two ports and the same resonance effects around 10 GHz seen in LF-TE10 02 and 03. The

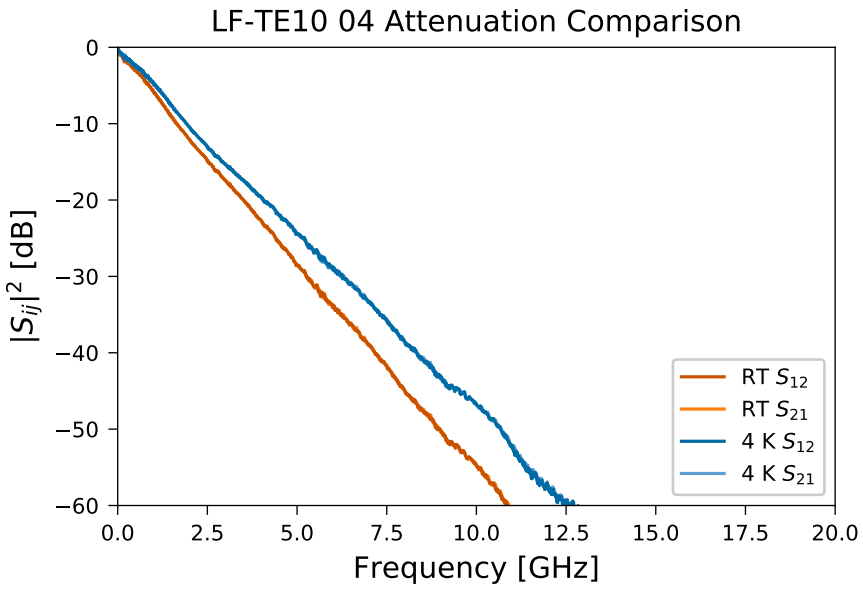

Figure 4.24: Comparison of attenuation for LF-TE10 04 at 4 K (blue) and at room temperature (red).

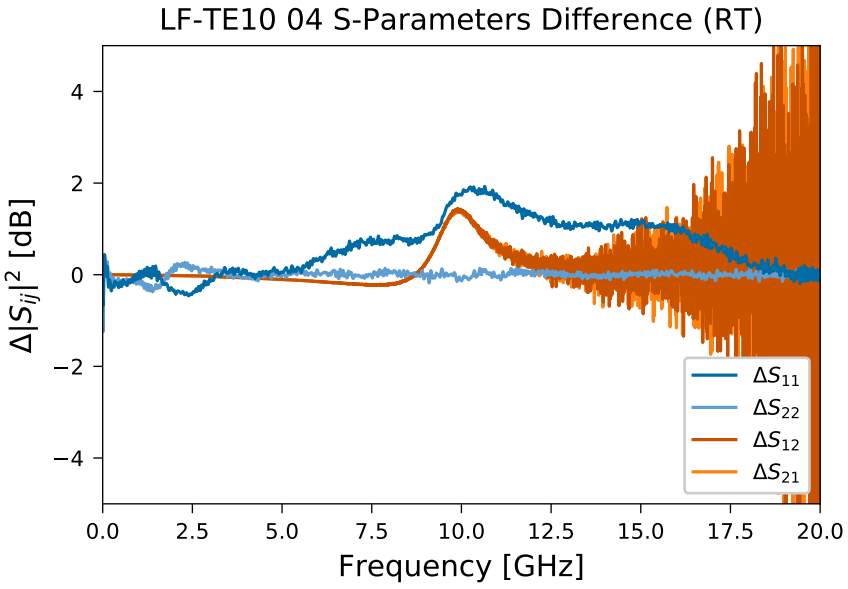

Figure 4.25: Difference in S-Parameters of LF-TE10 04 between initial testing and after partially removing and then re-inserting one of the threaded couplers several times.

main suspect for this poor performance is again some air bubble at one end of the filter.

4.3.4 LF-TS

LF-TS35 01 (Figure 4.22) shows performance that is largely comparable to LF-TE35 and LF-TE10. The attenuation is similar to LF-TE35 at around $-11\,\mathrm{dB\,GHz^{-1}}$, and the reflected power is similar to the "normal" performance, slightly beating theoretical performance throughout the range, and with very good performance at low frequencies. This design was discontinued largely because of the ease of end-filling and the boost to the mechanical strength provided by Eccosorb pressing into the threads of the coupler and filter body.

Chapter 5

Discussion

5.1 Remarks

Attenuation

Although the attenuation of similar filters may differ (*cf.* Table 4.2), looking at all of the filters, we can analyze the measured attenuation and compare it to the value provided for Eccosorb CR-124 by Laird. The attenuation of all of the filters produced during this project at 500 MHz and 5 GHz are plotted versus their Eccosorb fill length in Figure 5.1. Averaging these results reveals that in our filter designs, we have $20.7\,\mathrm{dB\,cm^{-1}}$ of attenuation at 5 GHz and $0.88\,\mathrm{dB\,cm^{-1}}$ of attenuation at 500 MHz. Laird quotes $0.48\,\mathrm{dB\,cm^{-1}}$ at 100 MHz, $6.5\,\mathrm{dB\,cm^{-1}}$ at 1 GHz, $20\,\mathrm{dB\,cm^{-1}}$ at 3 GHz, and $63\,\mathrm{dB\,cm^{-1}}$ at 8.6 GHz for Eccosorb CR-124 (see Figure D.5), leading to a predicted attenuation of approximately $35\,\mathrm{dB\,cm^{-1}}$ at 5 GHz and $3\,\mathrm{dB\,cm^{-1}}$ at 500 MHz [21]. Thus, our filters have lower attenuation than predicted, possibly due to the fact that the filters are small compared to the wavelength (especially at 500 MHz). While the electric field inside a coaxial cable is not uniformly radially distributed, this should not affect the attenuation, as long as the attenuation remains constant at different input powers. One note is that, while some filters may have attenuation that varies from this average, the attenuation is usually similarly affected at 500 MHz and 5 GHz, *i.e.* only the slope of the attenuation is affected.

Assuming that a similar relation also holds for the attenuation of Eccosorb CR-110 in filters versus on the data sheet, the predicted values in Table 2.1 should be reduced to approximately $0.013\,\mathrm{dB\,cm^{-1}}$ at 500 MHz and $0.51\,\mathrm{dB\,cm^{-1}}$ at 5 GHz (and hence 0.013 dB at 500 MHz and 0.51 dB at 5 GHz for a HF-TE10 filter). These values are similar to those given by Fang for his "HF" filters that have an Eccosorb fill length of 9.5 mm [16].

In these experiments, I have only measured the attenuation of Eccosorb up to 20 GHz. While commercial VNAs that measure up to 100 GHz exist, I was not able to locate any at ETH. However, Eccosorb has been studied in

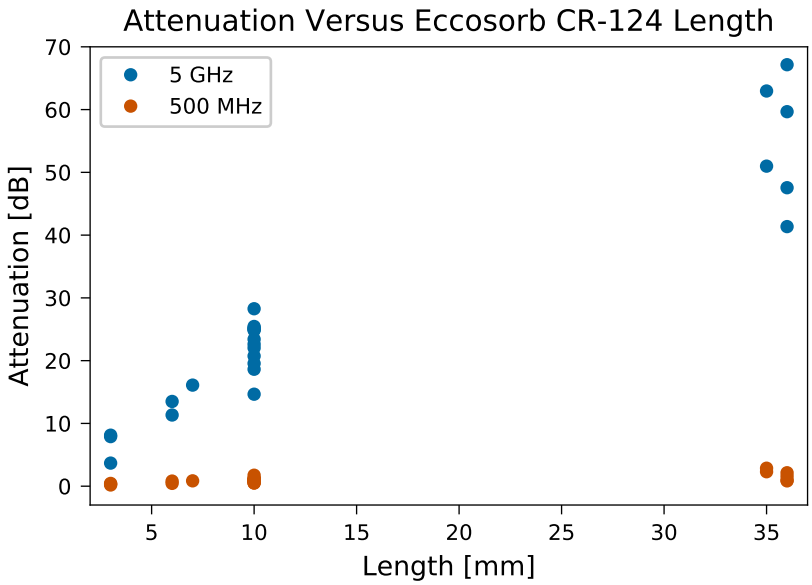

Figure 5.1: Attenuation of different filters versus the length of Eccosorb CR-124 in the filter. Attenuation at 5 GHz plotted in blue; attenuation at 500 MHz plotted in red-orange.

the far infrared, at millimeter and submillimeter wavelengths. Halpern *et al.* measured the absorption coefficient of Eccosorb CR-110 at 300 K, finding that it increased linearly from 2 cm^{-1} at 75 GHz to 25 cm^{-1} at 900 GHz [24]. Hemmati *et al.* extended this measurement out to 2700 GHz, finding that the attenuation of a 6.35 mm sample of CR-110 increased to 37 dB at 2700 GHz, with stronger grades of Eccosorb being even more attenuating [25]. Thus, although I was not able to measure out to extremely high frequencies, I am confident that Eccosorb filters remain attenuating out to thousands of gigahertz.

Labeling

Initially, I labeled filters with a unique number using a permanent marker. However, the marker is easily scratched off the filter by mechanical handling and is dissolved by many solvents. Filters with asymmetric performance revealed the need for labeling of the individual ports and tracking of the filter orientation during manufacturing. With these points in mind, recent labeling using the Arkograf has been largely successful. The only issue is that the mechanical tightening of the filters using pliers can partially remove the shallow marks produced by the Arkograf. This might be improved by

using mechanical engraving or by adding the permanent labels after final assembly and curing.

Thermalization

Eccosorb filters may also be used to improve the thermalization of the center conductor of coaxial cables. As previously mentioned, Eccosorb has a thermal expansion coefficient that better matches metals like copper. In addition, at cryogenic temperatures, the thermal conductivity of the Eccosorb is significantly greater than that of PTFE. Based on data from Wikus *et al.* Eccosorb CR-124 has a thermal conductivity of $4.0\,\mathrm{W\,m^{-1}\,K^{-1}}$ at 4 K and $0.38\,\mathrm{W\,m^{-1}\,K^{-1}}$ at 1 K [26]. Correspondingly, PTFE has thermal conductivities of $0.046\,\mathrm{W\,m^{-1}\,K^{-1}}$ at 4 K and $0.011\,\mathrm{W\,m^{-1}\,K^{-1}}$ at 1 K, based on data from the NIST cryogenics database. An Eccosorb filter should thus provide order of magnitude better thermalization of the center conductor than simply clamping the coaxial cable and relying on thermal conductivity through the PTFE dielectric, especially for cables with a reduced density (foam) dielectric.

Thermal Photons

In order to measure the need for Eccosorb filters, one issue that became interesting during the progression of this project was how many thermal photons at frequencies above the gap frequency are arriving at the sample. The coaxial cables themselves are attenuating for high frequency photons, but also have many modes available to extremely high frequency photons (>1000 GHz). To answer this question, numerical simulations were performed (as discussed in Appendix E). Based on this simulation, given our current cabeling and attenuation configuration without Eccosorb filters, we expect on the order of $5.5 \times 10^5\,\mathrm{photons\,s^{-1}}$ above the energy gap of aluminum and below the frequency at which the dielectric becomes strongly absorbing. As discussed in Appendix E, this simulation makes many assumptions, so this number is only a rough estimate. However, even assuming an additional 20 or 30 dB of attenuation from the cables at high frequencies, quasiparticle-inducing photon numbers this large indicate that Eccosorb filters may be required for experiments pursuing high coherence times.

Reflected Power

Bulk Eccosorb appears to behave reliably, handling thermal and mechanical cycling without issue. However, the connectors are a different issue. It seems that the reflected power is sensitive to small changes in how connections are formed, with air bubbles at the β side of the filter as the most likely culprit. The β-side coupler is inserted after filling the body with Eccosorb, making it difficult to guarantee that it is fully filled. Just as when trying to push

an inverted cup from air down into water, the coupler may force Eccosorb out through the threads without itself filling with Eccosorb. This could be remedied by pouring some Eccosorb into the empty space in the coupler before threading it into the filled body.

Another possibility would be that the reflected power depends on the sizing of the center wire. There is no clear reason why this would increase the reflected power, but it could be tested by deliberately shortening a wire and measuring the performance.

Given all of this, it may be interesting to again consider a side-fill design using a large side hole (5 mm). Since the COMSOL simulations showed no major difference between a LF-FS36 design with and without a hole, side filling should not negatively impact the electrical performance of the filters. For shorter lengths, uneven Eccosorb filling should not be a problem, even under the more difficult conditions of filter mass production.

5.2 Conclusion

After several variations, I have produced Eccosorb filters that demonstrate repeatable performance and beat the theoretical expectations. With some minor additional modifications, the LF-TE10 design should prove to be an ideal infrared-blocking filter for flux-line use. A future version, HF-TE, should provide similar performance for microwave drive-line use. These filters have improved mechanical strength over previous designs, and are easier to manufacture. Numerical simulations confirm the necessity of Eccosorb filters or other infrared-blocking filters to block quasiparticle-inducing photons that would otherwise reach the sample under current attenuation schemes.

5.3 Outlook

If adding Eccosorb to the second coupler before attaching it does not improve repeatability or reduce the reflected power, then future designs might look into other connector types. There are a number of small flange-mount designs that accept coaxial cable center conductors (some of which are made by Southwest Microwave). Other options would be to investigate using hermetic launch pins so that the center conductor could be soldered to something designed to fit into the connector at each end.

Ideally, some company would produce Eccosorb filters for cryogenic use. Several “miracle” filters showed extremely good performance, however these were probably accidental, as subsequent filters have not shown similar performance. With a bit more work, it would be possible to create some impedance-transforming region at each end of the filter to achieve stellar reflected power performance.

Appendix A

Filter Production Instructions

A.1 Filter Body Machining

Filter production begins by selecting the desired properties of the filter, usually its attenuation and frequency range. Once these are known, and a grade of Eccosorb—which affects both parameters—is selected, the attenuation is tuned by changing the length of the filter and the frequency range is tuned by changing the diameter of the hole in the filter body (see considerations in chapter 2). After this design work, a CAD model and a drawing must be produced. In order to fit the threaded couplers, the interior threads at the end of the filter body must match the SMA specifications. This dictates 1/4"–36 UNS 2B interior threads and a stop lip with a depth of 4.3 mm and a diameter of 4.6 mm. The threads should be as deep as possible, but do not need to be the full 4.3 mm deep (and this would be impossible or extremely difficult to physically machine). To specify this, the attribute "Norm Gewindehinterstich" can be applied to each of the threads to specify that they should have the normal region carved out behind the end of the threads, leaving a flat surface for the threaded coupler to press against. Note that the filled Eccosorb length will be approximately 3.8 mm greater than the distance between the stops due to the female SMA connector (which has male threads) having approximately 1.9 mm of empty space between the end of the dielectric and the end of the metal rim. An example drawing, scaled down, is presented in Figure A.1.

The filter bodies are ordered from the ETH central workshop by providing a complete drawing and specifying the material, quantity, and finish of the filters. It is helpful to provide a previously made filter as an example and a SMA coupler as a test piece. The physics workshop lacks the necessary 1/4"–36 UNS tap. Project turnaround time for the central workshop is normally a few days, even for normal-priority projects. Costs for medium-sized batches

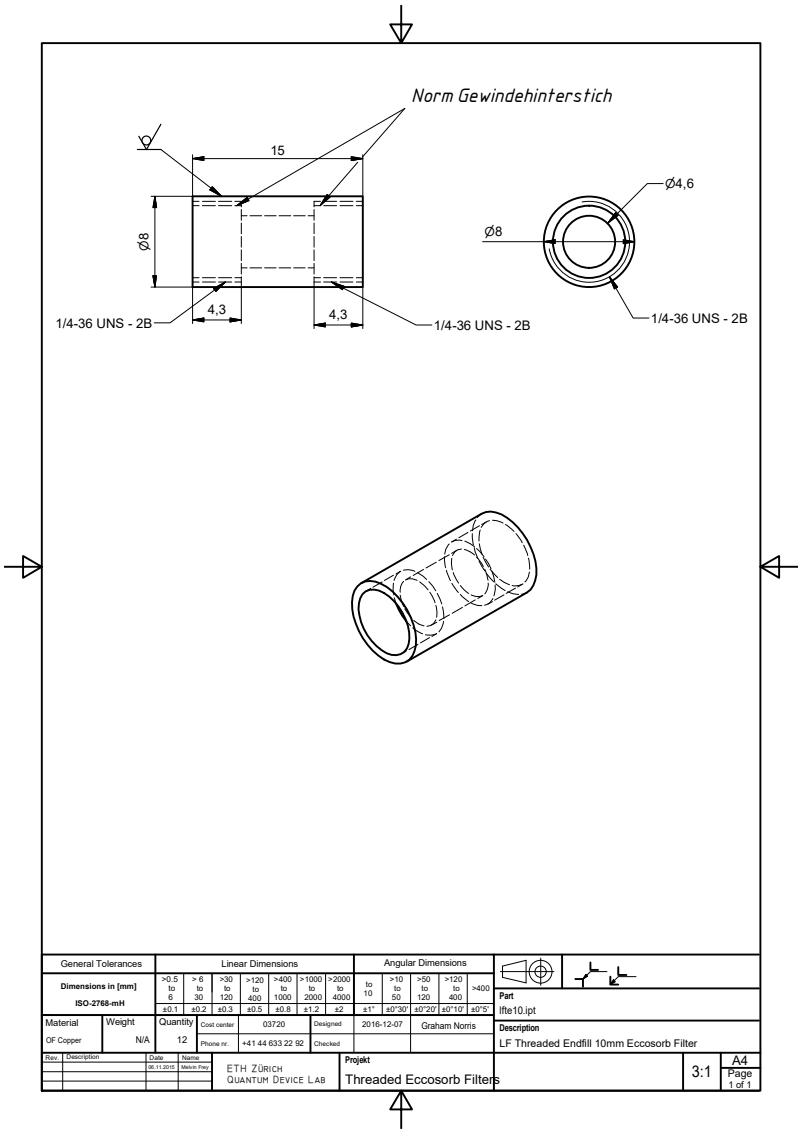

Figure A.1: CAD drawing of LF-TE10 filter body. Scale in this case is 1.5:1 rather than the 3:1 specified in the drawing.

of filters bodies can be around 10 CHF per body, although this is determined primarily by labor costs, so it is beneficial to order a number of identical filter bodies at the same time.

SMA couplers can be ordered through Distrelec (and the D-PHYS Distrelec omnibus order), but this also has a lead time of several days to a week, so it is advised to order the connectors (and wire, if needed) at the same time as the filter bodies. Ordering multiple couplers also lowers the cost-per-filter due to volume discounts.

A.2 Center Conductor Preparation

The center conductor of CEAM M-17/84 RG223, commercial RG223 flexible coaxial cable, is a perfect fit for the female socket of the SMA connector and is silver-plated for better conductivity. However, the fact that this wire is part of a pre-existing cable means that we have to first extract the part that we want. First cut a section of wire that is longer than the filter body and connectors. Then, remove the outer plastic insulation by slicing it with a razor blade and peeling it off. The two layers of stranded mesh conductor can be removed by pressing inward at the two ends to enlarge the mesh and then sliding it off, sort of like the solution to a "Chinese finger trap". The inner polyethylene dielectric is harder to remove. The easiest method that I found was to carve away the dielectric at one end of the wire using a knife and then pull the center wire out using pliers while twisting the dielectric (see Figure A.2). Try not to bend the wire during this process.

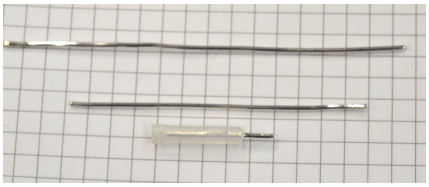

Figure A.2: Center conductor and polyethylene dielectric from CEAM RG223 coaixal cable.

Next, gently file and round the ends so that they fit—with some effort—into a SMA coupler. Insert the wire as far as possible into one coupler and thread this coupler into the filter body. *The following steps are crucial to filter performance, so go slowly!* Insert the end of the wire into the other coupler and try to thread the coupler into the body. If the coupler does not come close at all to threading, trim off 1 mm, round the end, and try again. Once the filter begins threading onto the filter, trim in smaller increments. Once the coupler stops, to see whether this is due to the wire reaching the end of the socket in the coupler, or the coupler reaching the stop, unscrew the other coupler slightly and then try to thread this coupler slightly farther.

If, on the final iteration, the coupler reaches the stop before resistance or effort is felt, start again. Wires of the correct length usually stick several mm out of the filter body (see Figure A.3). Be wary of the wire getting "stuck" in one of the couplers, try to wiggle the wire to check that it is really inserted to the maximum depth. It is best to keep each filter body and its matching center conductor and couplers separate from the others in case there are minor differences between these.

Figure A.3: Center conductor protruding out of LF-TE06 filter body.

A.3 Filter Assembly

A.3.1 Labeling

After manufacturing, all filter bodies are sanded to remove oxide coating and labeled with their model name, a serial number, and port labels (α and β). Current labeling is done using an electric scribe, the "Arkograph", present in the central workshop. These markings survive subsequent cleaning steps, do not out-gas in a vacuum, and are generally more durable than permanent marker labels. In the future, we may use a mechanical engraver to get deeper marks.

A.3.2 Preparation

When it is time to assemble the filters, the first step is to prepare the correct equipment. Table A.1 lists the equipment that is needed to assemble filters using the current procedure. Note that it is useful to have backups for items like syringes and paper towels in case of mistakes.

Table A.1: Equipment used for filter assembly. n is the number of filters. Items above the middle line can be purchased in D-PHYS shop; items below the line should be in our workshop already.

Equipment	Quantity
1.2 mm by 40 mm Needle	1
1.5 mm by 5 mm NBR O-Rings	$2n$
250 ml Plastic Beaker	1
Plastic Tweezers	1
Threaded SMA Covers	n
10 ml Syringe	1
2 ml Syringe	1
Wooden Spatulas	Several
10 cm by 10 cm Aluminum Foil	1
Aluminum U-Channel	1
Glass Beaker	1
Hotplate	1
Paper Towels	Several
Pliers	2
Scale	1

Lay out paper towels to form a work space where the filters will be filled and assembled, usually next to the hotplate. Also place filters between the hotplate and the scale in case of spills. Remove the syringes from their packages and attach the needle to the 2 ml syringe. See Figure A.4 for an example image.

A.3.3 Cleaning

Prior to assembly, all parts are cleaned to remove contaminants and enhance galvanic contact between all parts. The copper filter bodies, which are usually somewhat oxidized, are soaked in a 10% citric acid solution for 5 min and then rinsed in distilled (DI) water and isopropanol (IPA) and then set on a clean paper towel to dry. The silver-plated center conductor are usually prepared immediately before filter assembly and as such are not substantially oxidized. Thus, they and all remaining parts are cleaned of oils by rinsing in DI water and IPA. Keep each filter body and its center conductor and couplers separate from all others.

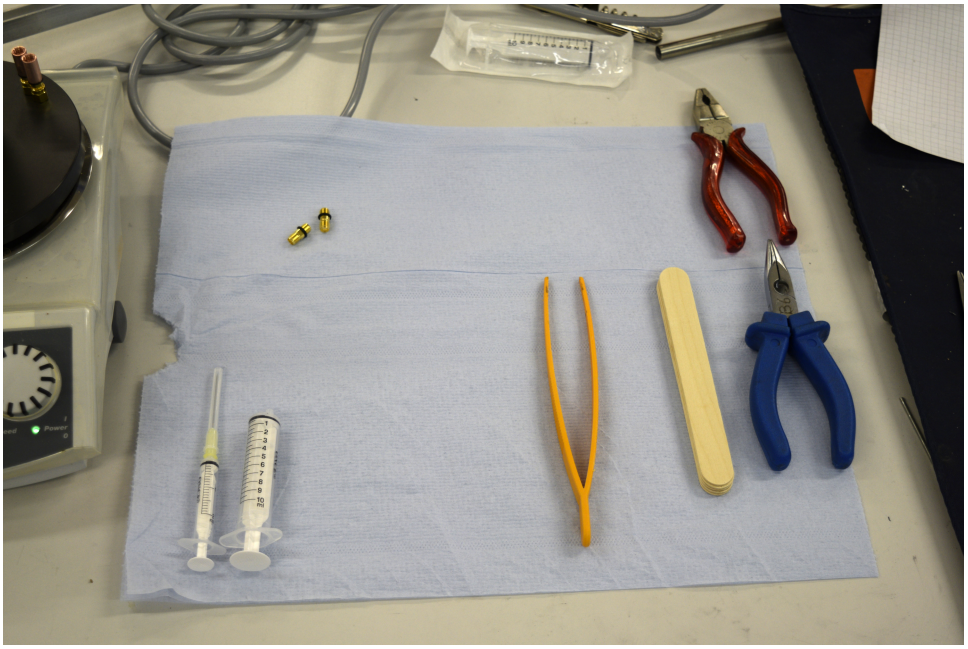

Figure A.4: Image of filter assembly preparation. Not all equipment listed above is shown here. The object at the left edge of the frame is the hotplate.

A.3.4 Eccosorb Filling Preparation

After the filter parts have dried, don clean gloves and place an o-ring on one side of each coupler, between the threads and the center section. Insert the center conductor into the o-ring side of the coupler, apply a drop of thread locker (Loctite 240) to the threads on the o-ring side, and thread this assembly into the α side of the filter body, wiping up any excess thread locker. Place a SMA cap (Amphenol 132360) on the other end of the inserted coupler. The o-ring is to direct any Eccosorb that leaks out between the coupler and the filter body towards the sides rather than onto the threads.

A.3.5 Eccosorb Filling

According to the Eccosorb CR-124 specification sheet, parts A and B should be mixed in a 100 : 2.6 ratio. In a convenient batch size, this amounts to 30 g of part A and 0.78 g of part B. Note that both parts A and B are slightly dangerous, so wear nitrile gloves, safety glasses, and a lab coat if possible.

Fill the glass beaker partially with water and begin heating this to 85 °C on the hotplate. This is done to avoid uneven heating or melting the plastic beaker. Extract 30 g of Eccosorb CR-124 Part A from the tin and place

it in a plastic beaker. A plastic beaker is used because it is disposable; the cured Eccosorb is extremely tough and difficult to remove from most materials. The cold part A is extremely viscous, so this will be difficult. I have found the best method to be a slow stirring or scooping motion with a wooden spatula. Place the plastic beaker in the glass beaker with hot water to begin warming the Eccosorb part A. Also place the partially-assembled filters onto the hotplate, α (cap) side down, so that they begin warming up to the working temperature. The water bath is used here to protect the plastic beaker from any temperature swings of the hotplate and make sure that it does not melt. Pre-heating the filters helps keep the Eccosorb flowing when it contacts the filter body, otherwise, the large heat capacity of the filter body quickly cools the Eccosorb, stopping any flow and resulting in partially filled filters.

Once the Eccosorb part A is warm, which should greatly reduce its viscosity, the next step is to add the part B. Part B, the activator, is already a liquid at room temperature, and the easiest way to add it is to use the 2 ml syringe with a needle. Place the plastic beaker on the scale, zero it, draw approximately 1 ml of part B into the syringe, and then slowly add it to the plastic beaker until it reads 0.78 g.

Before mixing, place the beaker back in the water bath for a minute to re-warm the epoxy. Once the mixture has warmed up again, mix with a wooden spatula. The working time of the mixed epoxy varies based on temperature, but is approximately 20 min.

To degas the mixture in order to reduce the chances of bubble formation, first open the vacuum chamber lid by applying lateral force. Place the aluminum foil on the bottom of the chamber to protect it against any spillage, replace the lid, close any fill valves and open valves to the vacuum pump. Turn on the vacuum pump and observe the pressure decreasing in the vacuum gauge. Allow the sample to de-gas for several minutes, noting the foam that forms on the top of the mixture as bubbles are drawn out, before reversing the procedure above (see Figure A.5).

Return the plastic beaker to the water bath and allow it to warm again for several minutes. In the meantime, move the filter bodies over to the work area, still vertically aligned with the α side down. Gently mix the epoxy (to avoid mixing in extra air), tip the beaker slightly, and collect it in one side. Draw as much of the Eccosorb into the 10 ml syringe as possible and then begin filling the filter bodies (see Figure A.6). Go slowly, giving the Eccosorb time to reach the bottom of the filter and spread out. Continue filling until the Eccosorb level is approximately 1 mm to 2 mm above the stop on the inside of the filter body (see Figure A.7). This is to ensure that there is enough Eccosorb to fill the empty space in the second conductor. Thread the second coupler, o-ring side first, into the filled filter as far as possible. Do not worry if it does not reach the stop at this point. Fill the remaining filters,

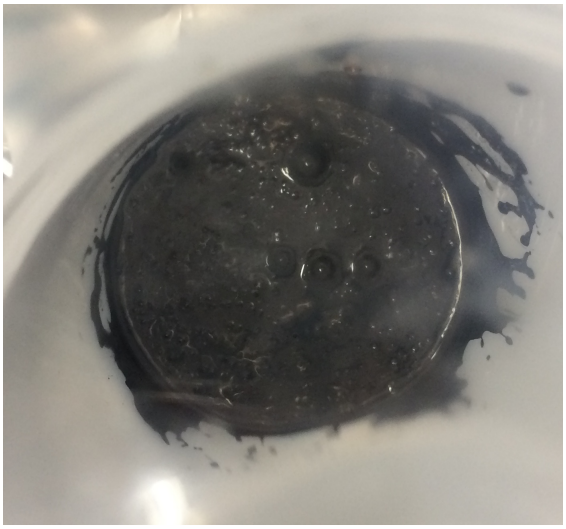

Figure A.5: Image of Eccosorb that is being degassed in a vacuum chamber. Note the bubbles indicating that gas is removed from the Eccosorb.

remove the water bath from the hotplate, place the aluminum U-channel on the hotplate, and increase the temperature to 120 °C.

Place the filters in the U-channel to heat up to this curing temperature. The Eccosorb is initially very fluid at this temperature, so it may start seeping out around the threads, appearing between the o-ring and filter body. At this point, use the pliers to apply force and get the β coupler to thread completely into the filter body. Clean up any leaking Eccosorb with paper towels and replace in the U-channel (see Figure A.8). In 10 min, when the leaking has stopped, cut away the o-rings to prevent them from being glued to the filter by small amounts of Eccosorb near the threads.

Allow the filters to cure at this temperature for two hours before removing them and allowing them to cool. Check that the unused Eccosorb is curing and then throw this away in the lab trash. Clean up all other equipment while the filters are curing.

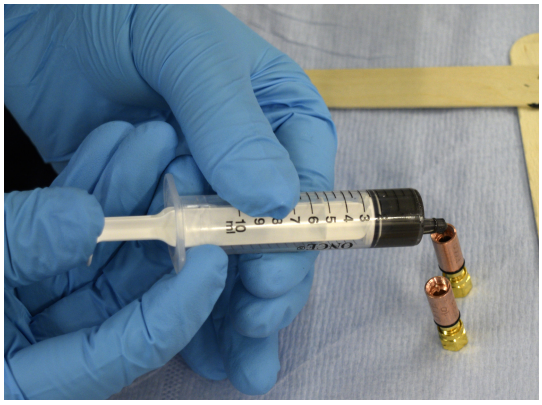

Figure A.6: Image of filters being filled with Eccosorb. Note that filter bodies have just been removed from the hotplate and are still warm.

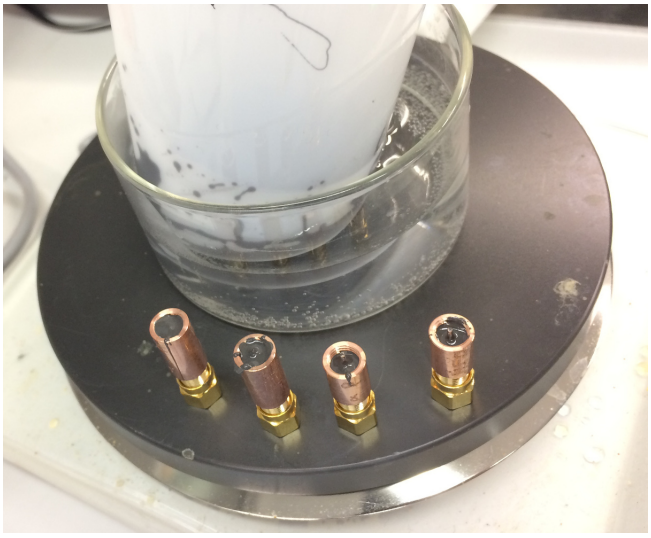

Figure A.7: Image of filter bodies filled with Eccosorb. Filters are sitting on the hotplate to warm up the Eccosorb before attaching the second coupler. Note the glass beaker for the water bath and the plastic beaker containing the Eccosorb mixture.

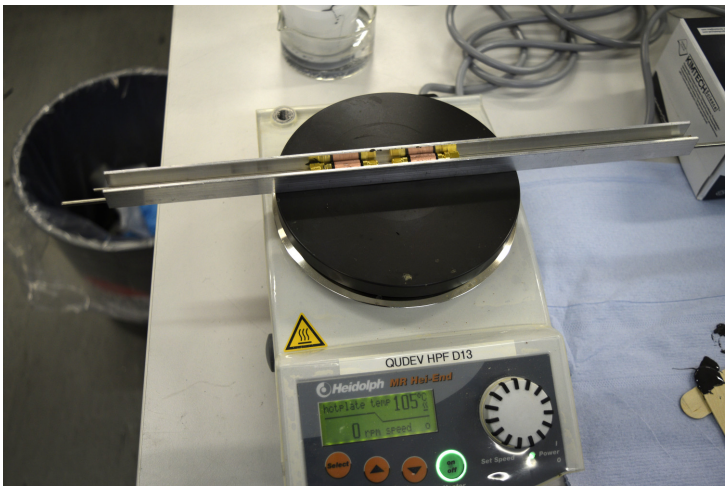

Figure A.8: Image of filter bodies curing in an aluminum U-channel. O-rings have not yet been removed, but the leaking Eccosorb has been wiped off of the filters.

Appendix B

Filter Autopsies

In order to check various hypotheses about the performance of the LF-FS36, LF-PS36, and LF-TE35 filters such as Eccosorb filling and center-conductor location, destructive autopsies of LF-FS36 01, LF-PS36 01 and LF-TE35 01 were performed. The filters were placed on the bottom of a 136 mm by 71 mm by 32 mm polycarbonate sample holder box purchased from the D-PHYS shop. This size was larger than ideal, but the correct size sample case was out of stock at the time.

In order to cover and support the filters, 192 g of Loctite Stycast 1266 was prepared in the mixing ratio of 28 parts B compound to 100 parts A compound. This was more than strictly necessary to cover the filters, but this was not obvious when preparing the Stycast. No vacuum degassing was performed.

The Stycast was initially smooth and completely flat in the container. However, as indicated in the data sheet, masses above 100 g generate significant heat due to the exothermic reaction that occurs during epoxy curing. This heat warped the sample holder and, two hours after mixing the epoxy, was such that it was not possible to hold the sample holder for more than a few seconds. This heat did have the benefit of curing the epoxy in approximately two hours rather than the 8 h to 16 h quoted for curing at 25 °C on the data sheet. The Stycast appears to have expanded slightly during curing, as part of the upper surface in the sample holder is raised, as are the corners. In addition, many bubbles appeared in the cured epoxy that were not visible immediately after pouring the mixed epoxy into the sample holder.

After waiting several more days, the milling was performed. The sample holder was mounted inverted in the vise such that the bottom side faced upwards. This minimized the amount of Stycast or polycarbonate that had to be milled before reaching the filter bodies. An approximately 8 mm wide, flat-bottomed milling bit was used to mill channels approximately 44 mm long and between 5 mm and 8 mm deep, centered on the body cavity of the filter. This length corresponds to the total length of the filter cavity and

part of the end connectors, and the depth was selected to reach the central conductors of the different filters. Each channel was slowly milled down 300 µm to 400 µm at a time while using cutting fluid. The block, with all three slots and filters clearly visible is presented in Figure B.1.

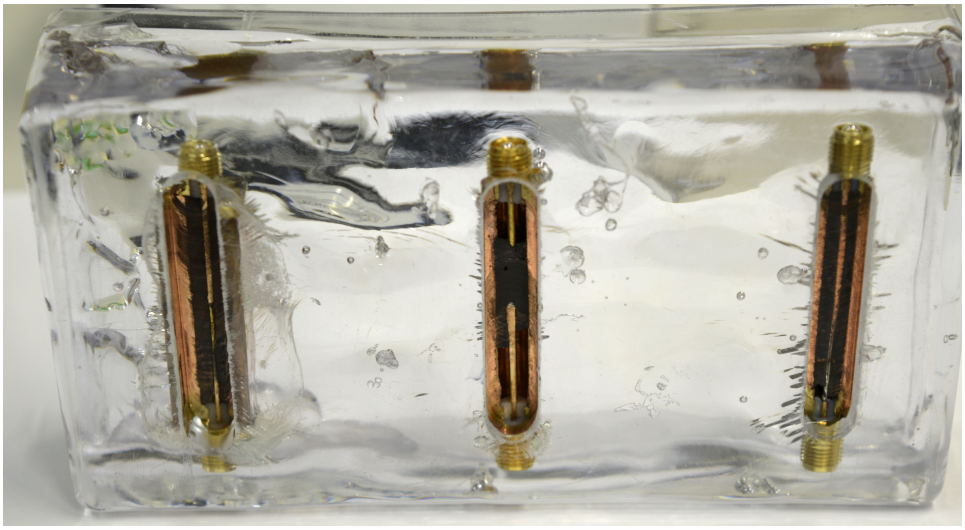

Figure B.1: Block of Stycast with embedded Eccosorb filters. *From left to right*: LF-FS36 01, LF-PS36 01, LF-TE35 01.

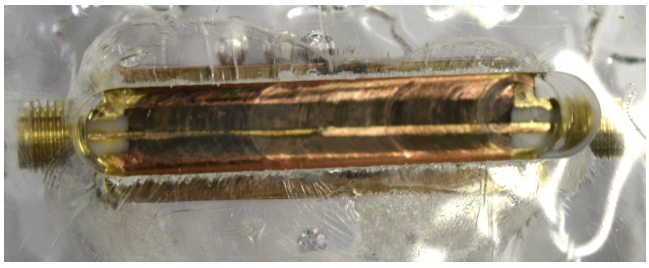

Figure B.2: LF-FS36 01 autopsy image. Cavity is completely filled with Eccosorb and the center conductors have met end-to-end.

LF-FS36 01 (see Figure B.2) appears completely filled with Eccosorb at the current depth (with no bubbles or voids), although some air bubbles may have been observed while milling to this depth. Additionally, the two central conductors have met almost perfectly end-to-end.

LF-PS36 01 (see Figure B.3) was only partially filled with Eccosorb, with the Eccosorb only occupying the central 1 cm to 1.5 cm near the fill hole. This was likely caused by the smaller side hole making filling more difficult and possibly by a filter body that was not sufficiently heated to allow the Eccosorb to flow freely. The remaining volume is empty. The central

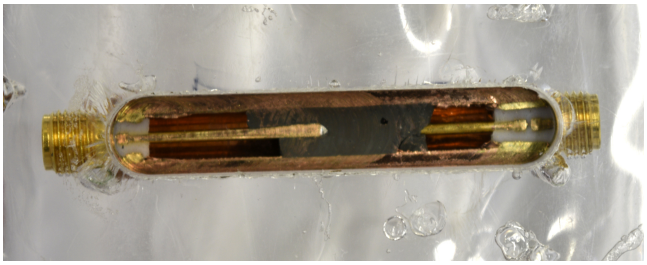

Figure B.3: LF-PS36 01 autopsy image. Cavity is only partially filled with Eccosorb and the center conductors have not met end-to-end (only one conductor is visible in the middle of the filter).

conductors appear to have met side-to-side, as the center conductor from one side is visible at the milled surface, but the other conductor is not. From the empty space to the side, it appears that this second central conductor is below the first central conductor at the joining location.

Figure B.4: LF-TE35 01 autopsy image. Cavity almost completely filled with Eccosorb (there is a small void near the left connector) and the center conductors largely remained in the middle of the cavity.

LF-TE35 01 (see Figure B.4) has a bubble near the end from which Eccosorb was filled, but is otherwise filled. The central conductor shows some slight bending, but is still nicely mated to the one connector in which it is visible.

Appendix C

COMSOL Simulations

I pursued COMSOL simulations of the LF-FS36 filter in order to determine the effect of side filling through a large hole on the scattering parameters of the filter.

C.1 Simulation Parameters

When preparing the COMSOL model, I matched the geometry of the model to the LF-FS36 filter. The length of the model is 36 mm, the inner diameter is 5.1 mm, and the diameter of the center conductor is 1.3 mm. The hole on the side of the model has a diameter of 5 mm. The center and outer conductor are specified as OFHC copper, while the space between the center conductor and the outer conductor, including the hole, is filled with a custom material that has dielectric data corresponding to Eccosorb CR-124. I imported the exact data points and then use linear interpolation between these points to get functions that are defined at all frequencies.

I performed the scattering parameters simulations within the "Electromagnetic Waves, Frequency Domain" (emw) module. All surfaces on the model that correspond to OFHC copper surfaces have an impedance matching boundary condition. The hole on the side of the model has a first-order plane-wave scattering boundary condition. Then, the input and output ports are specified as 50 Ω coaxial cable lumped ports, with wave excitation only at the input port.

The mesh was automatically generated by COMSOL, however, I specified the maximum element size as 3.33 mm and the minimum element size as 64.8 µm, such that the elements are always much smaller than the wavelength. The maximum element growth rate was 1.5, the curvature factor was 0.6, and the resolution of narrow regions was 0.5. The mesh is pictured below in Figure C.1.

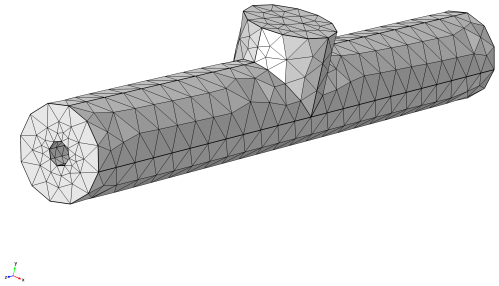

Figure C.1: COMSOL mesh for LF-FS36 filter including the hole. Due to how the COMSOL simulations work, the copper body of the filter is simply specified as a boundary condition, as we do not care how the outside of the filter interacts with far-field radiation.

C.2 Simulation Results

The primary metric I was interested in to compare a design with and without a hole was the scattering parameters. It would not matter if there was some difference in the electric field distribution between the filters as long as their overall performance was the same. I have given the scattering parameters of the design including the hole and the solid design without a side hole below in Figure C.2 and Figure C.3.

These plots are quite different from the measured scattering parameters (*cf.* Figure 4.1), but the two plots are extremely similar to each other, indicating that the hole plays only a minor difference, and that removing this hole should not drastically improve the performance of the filter. Comparing these plots to the measured data also reveals that most of the complexity in the observed S-parameters cannot be explained by the geometry of the filter or the electromagnetic properties of the Eccosorb, although it is surprising that the COMSOL simulation does not produce results that are more similar to the theoretical predictions (see Figure D.19).

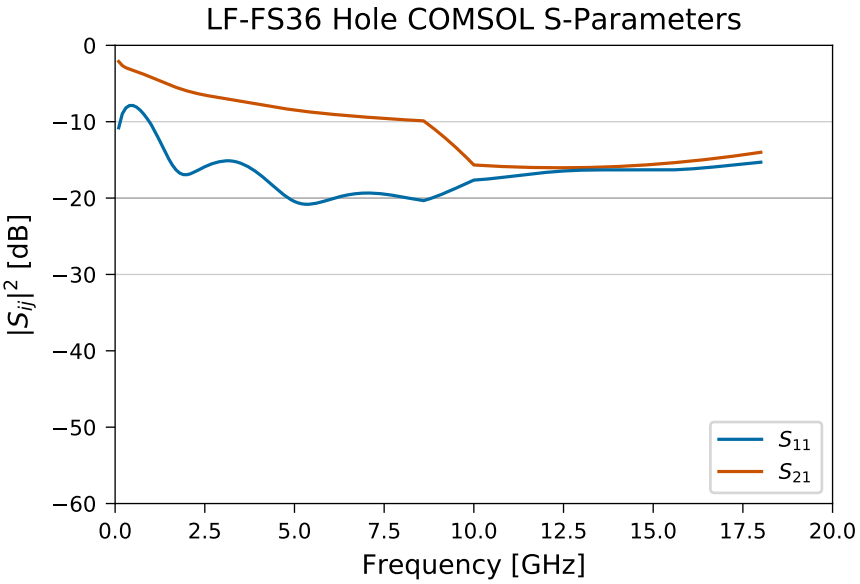

Figure C.2: COMSOL calculated scattering parameters for LF-FS36 including the side hole.

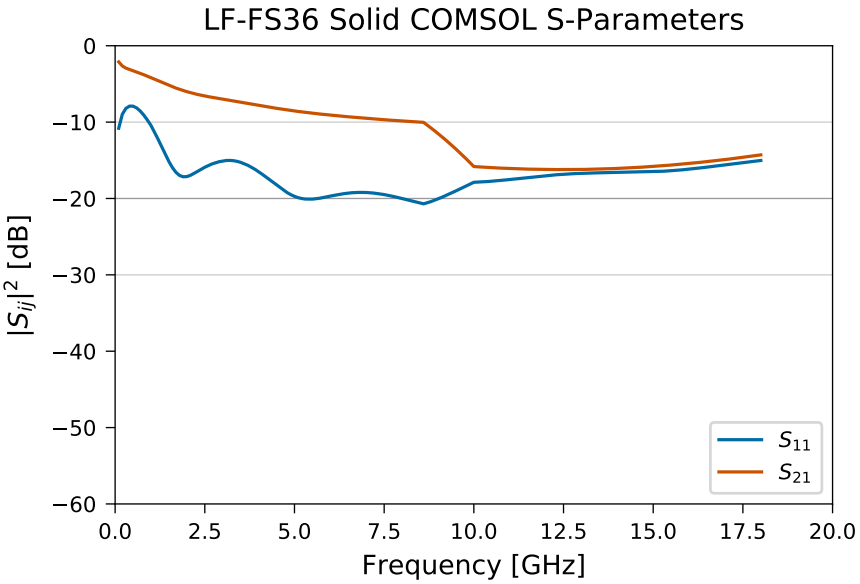

Figure C.3: COMSOL calculated scattering parameters for LF-FS36 without the side hole.

Appendix D

Eccosorb Properties

D.1 Physical Properties

D.2 Electromagnetic Properties

According to the Eccosorb CR Technical Bulletin, Eccosorb CR castable epoxies CR-XXX share electromagnetic properties with the machinable stock MF-XXX of the same number [20]. Therefore, all electromagnetic properties plotted below are listed for Eccosorb MF and derived from [21].

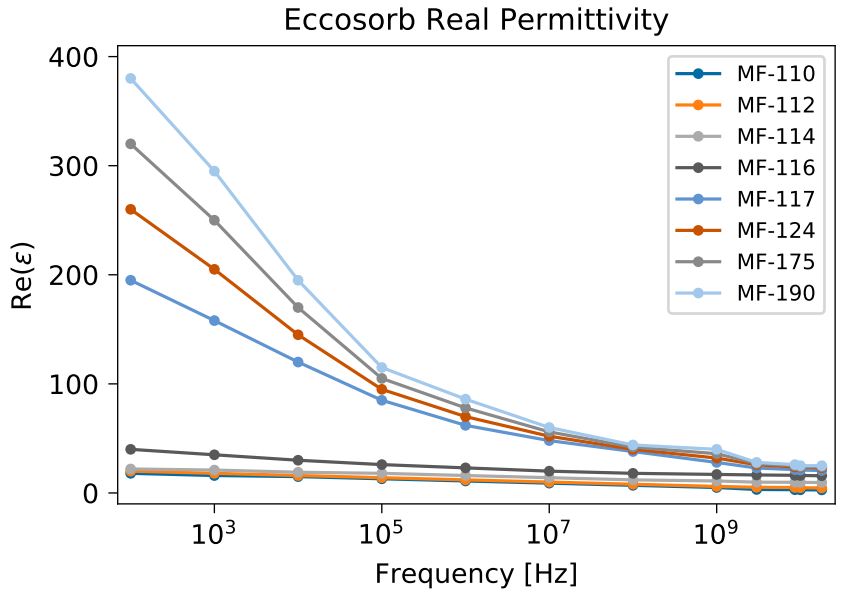

Figure D.1: Real component of permittivity of grades of Eccosorb from MF-110 to MF-190

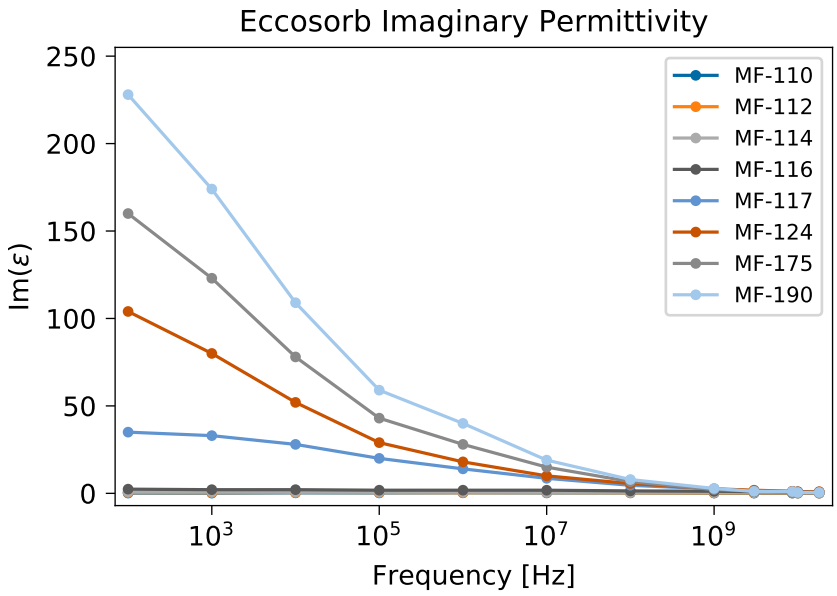

Figure D.2: Imaginary component of permittivity of grades of Eccosorb from MF-110 to MF-190

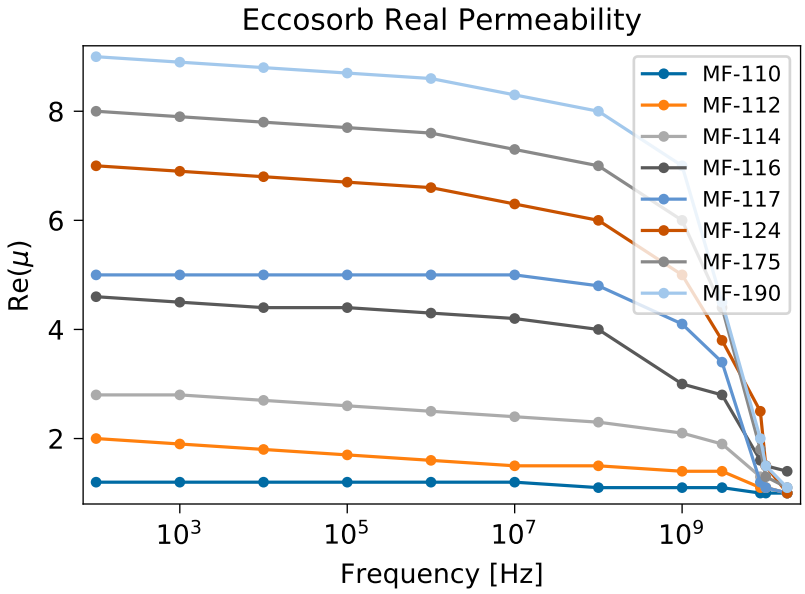

Figure D.3: Real component of permeability of grades of Eccosorb from MF-110 to MF-190

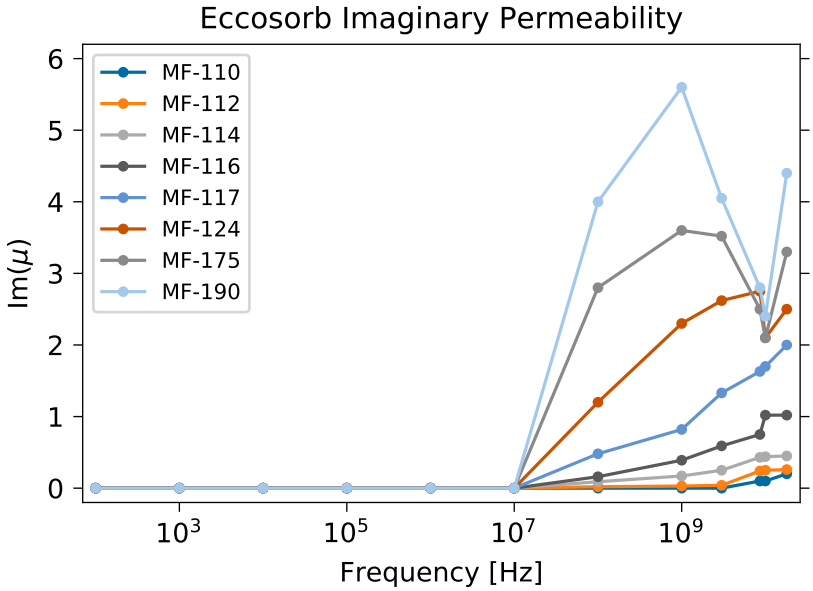

Figure D.4: Imaginary component of permeability of grades of Eccosorb from MF-110 to MF-190

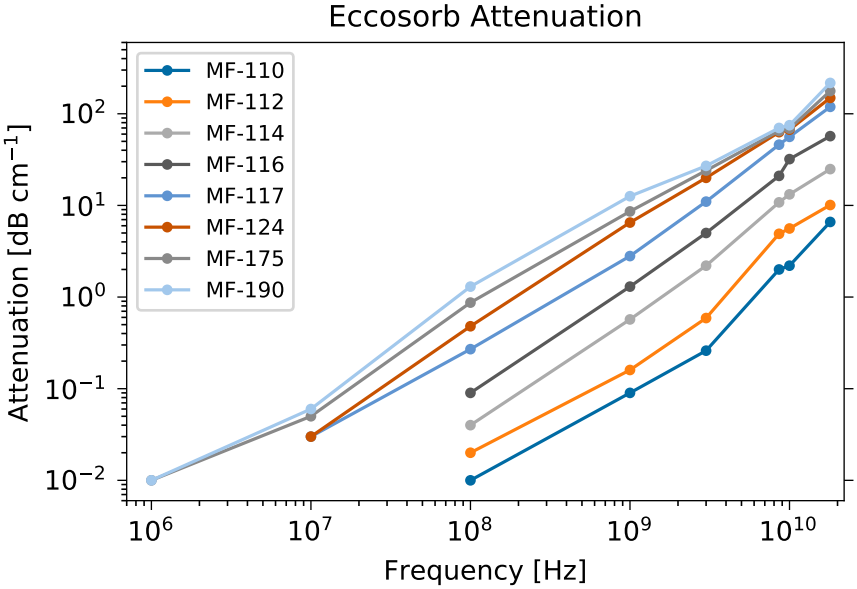

Figure D.5: Attenuation in $\mathrm{dB\,cm^{-1}}$ of grades of Eccosorb from MF-110 to MF-190 across frequencies from 1 MHz to 20 GHz. Note the change in the scale of the mantissa relative to the preceding Eccosorb plots (done such that the different grades would appear distinct; the units are still dB). None of the grades of Eccosorb have any attenuation of frequencies below 1 MHz.

D.3 Calculated Reflected Power versus Conductor Radius Ratio for Different Grades of Eccosorb

The following figures were all calcualted using the data provided by Laird along with Equation 2.4 and Equation 2.7, following the general procedures from that section.

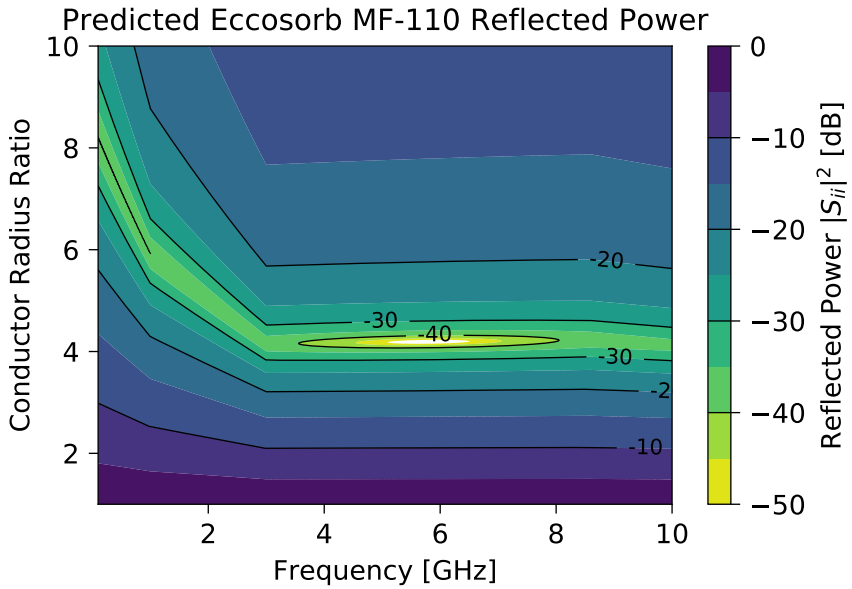

Figure D.6: Calculated reflected power of Eccosorb MF-110 plotted against outer-conductor inner-diameter to center-conductor outer-diameter ratios from 1 to 10 and frequencies from 1 GHz to 10 GHz.

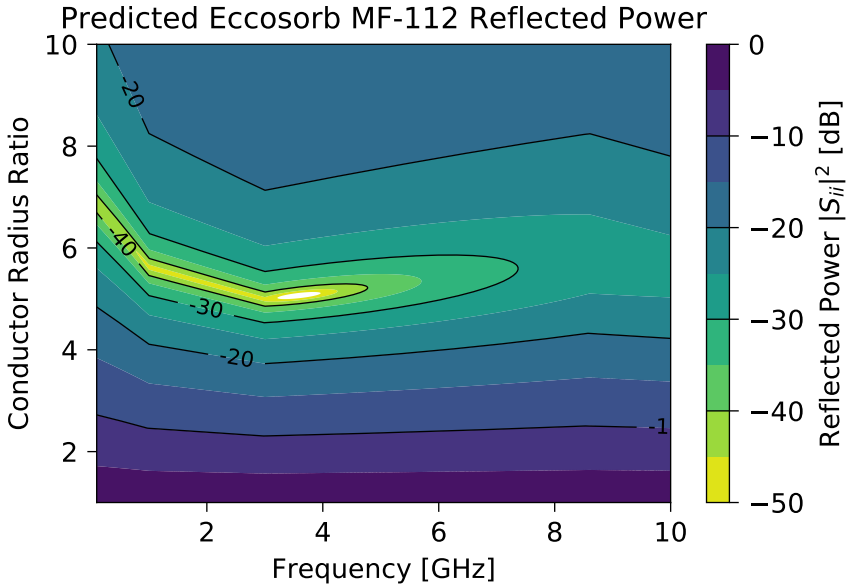

Figure D.7: Calculated reflected power of Eccosorb MF-112 plotted against outer-conductor inner-diameter to center-conductor outer-diameter ratios from 1 to 10 and frequencies from 1 GHz to 10 GHz.

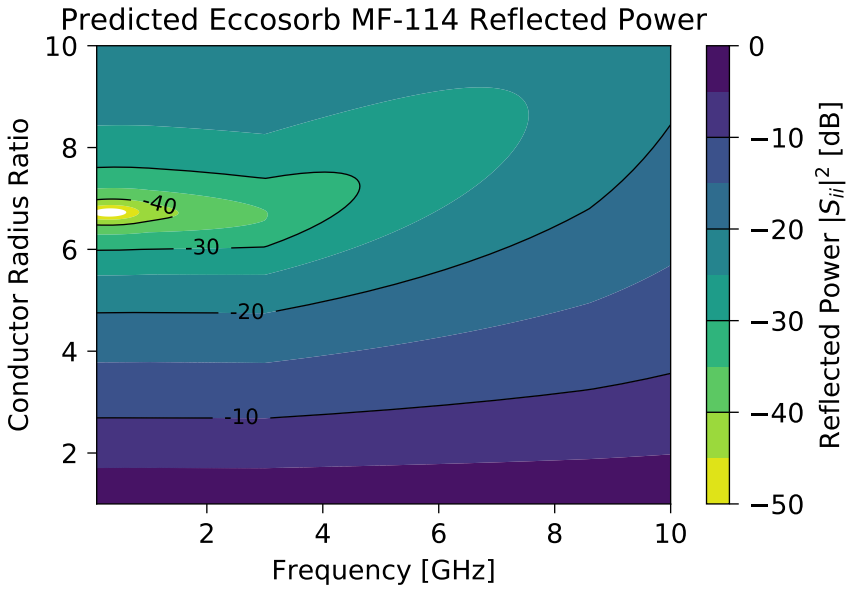

Figure D.8: Calculated reflected power of Eccosorb MF-114 plotted against outer-conductor inner-diameter to center-conductor outer-diameter ratios from 1 to 10 and frequencies from 1 GHz to 10 GHz.

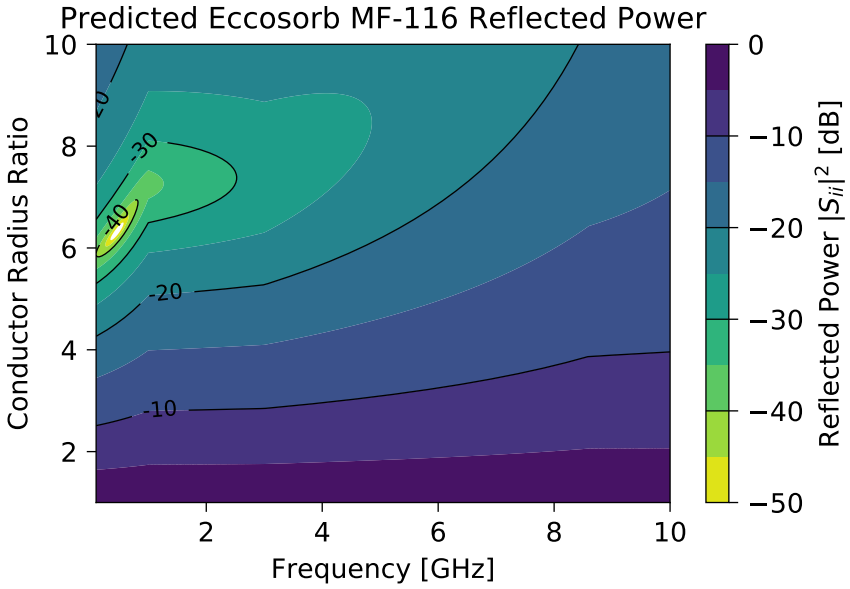

Figure D.9: Calculated reflected power of Eccosorb MF-116 plotted against outer-conductor inner-diameter to center-conductor outer-diameter ratios from 1 to 10 and frequencies from 1 GHz to 10 GHz.

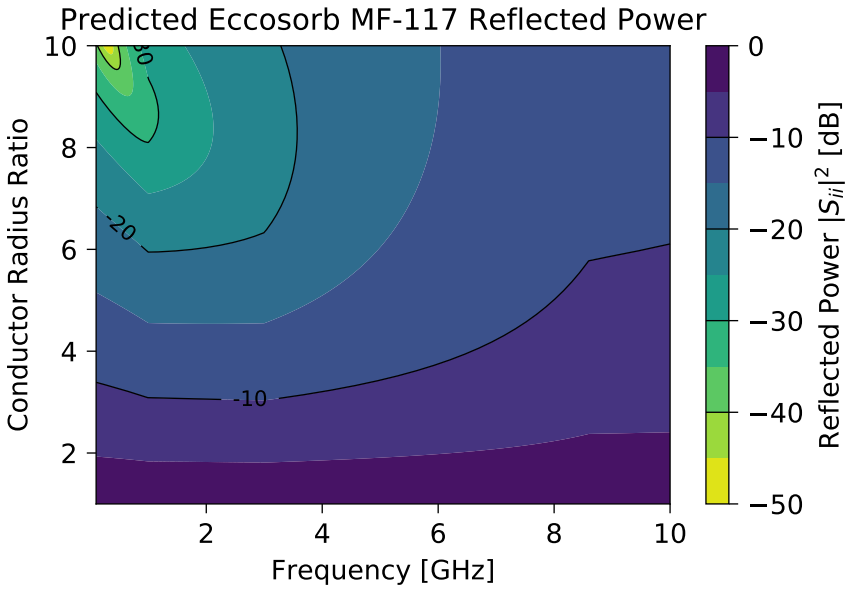

Figure D.10: Calculated reflected power of Eccosorb MF-117 plotted against outer-conductor inner-diameter to center-conductor outer-diameter ratios from 1 to 10 and frequencies from 1 GHz to 10 GHz.

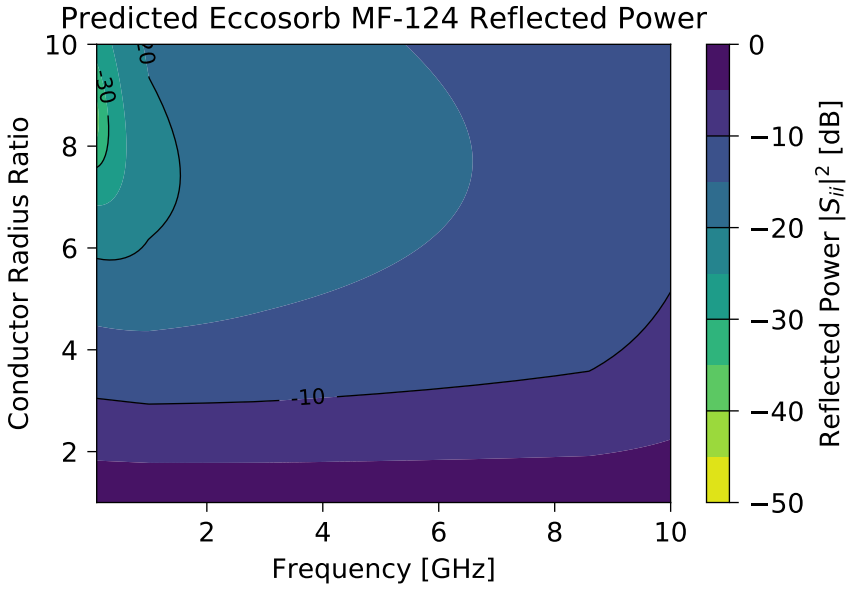

Figure D.11: Calculated reflected power versus outer conductor inner diameter to inner conductor outer diameter ratio and frequency for Eccosorb MF-124.

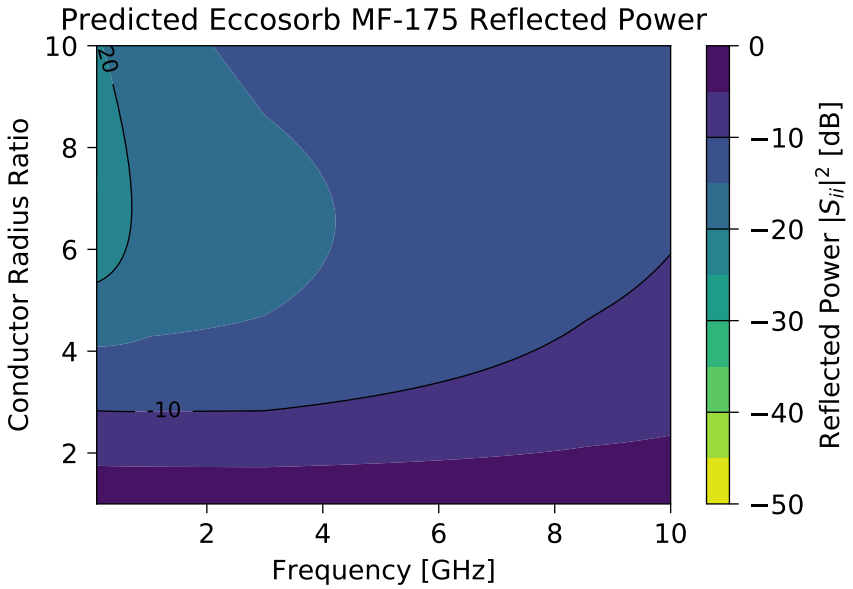

Figure D.12: Calculated reflected power of Eccosorb MF-175 plotted against outer-conductor inner-diameter to center-conductor outer-diameter ratios from 1 to 10 and frequencies from 1 GHz to 10 GHz.

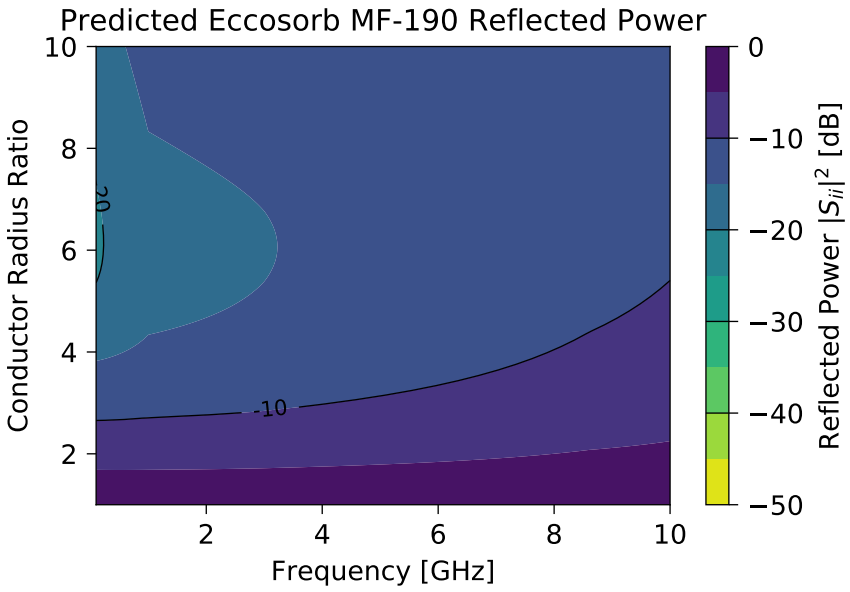

Figure D.13: Calculated reflected power of Eccosorb MF-190 plotted against outer-conductor inner-diameter to center-conductor outer-diameter ratios from 1 to 10 and frequencies from 1 GHz to 10 GHz.

D.4 Calculated Optimal Reflected Power for Different Grades of Eccosorb

The following figures were all calcualted using the data provided by Laird along with Equation 2.4 and Equation 2.7, following the general procedures from that section.

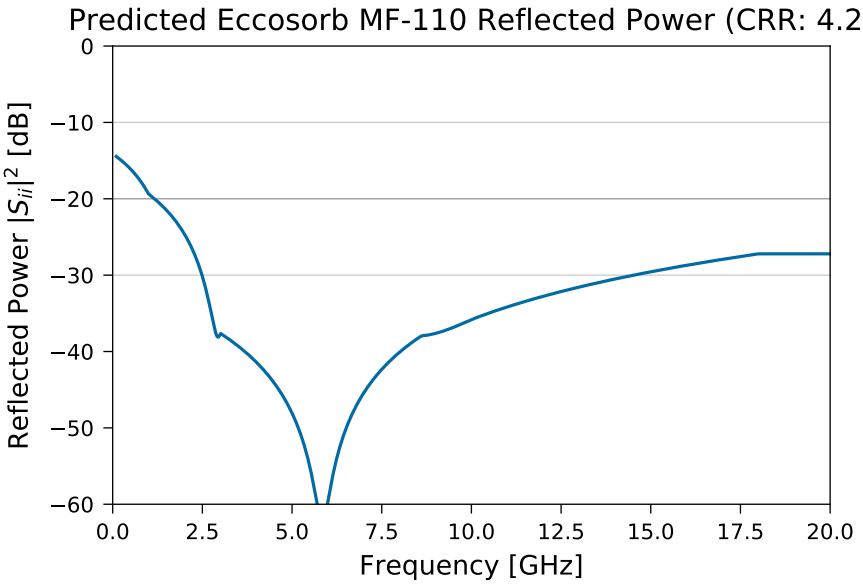

Figure D.14: Calculated reflected power of Eccosorb MF-110 at a conductor radius ratio of 4.2 and frequencies from 1 GHz to 10 GHz.

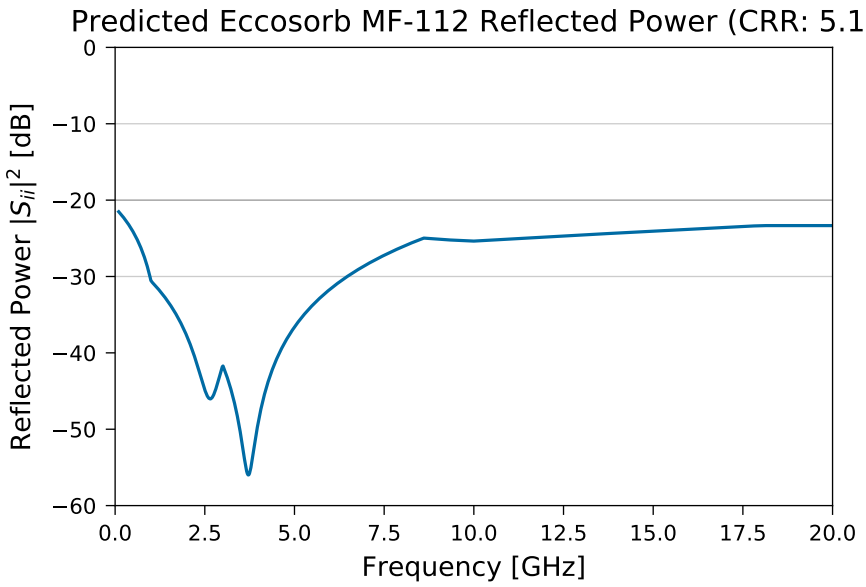

Figure D.15: Calculated reflected power of Eccosorb MF-112 at a conductor radius ratio of 5.1 and frequencies from 1 GHz to 10 GHz.

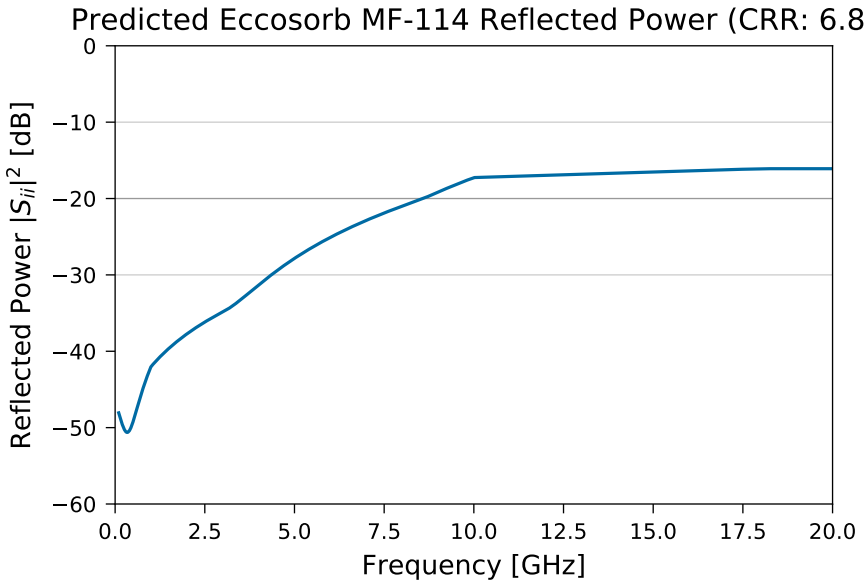

Figure D.16: Calculated reflected power of Eccosorb MF-114 at a conductor radius ratio of 6.8 and frequencies from 1 GHz to 10 GHz.

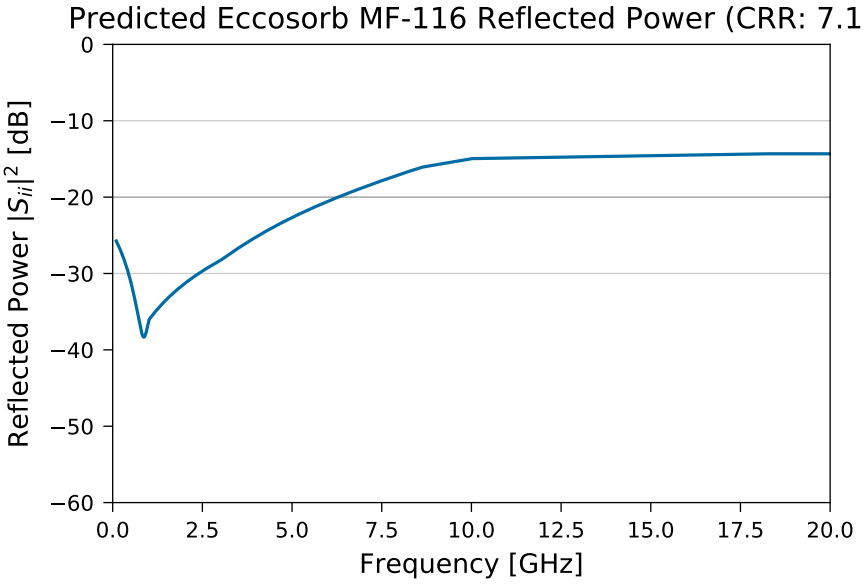

Figure D.17: Calculated reflected power of Eccosorb MF-116 at a conductor radius ratio of 7.1 and frequencies from 1 GHz to 10 GHz.

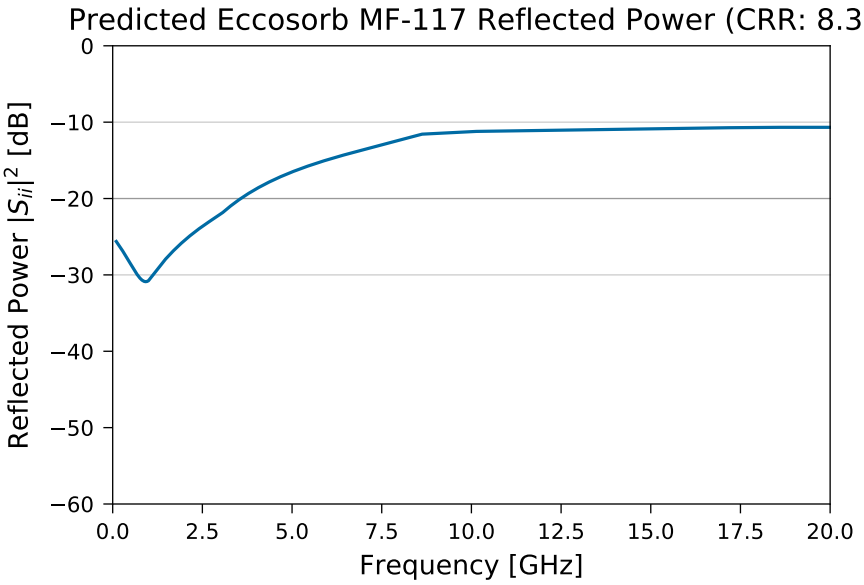

Figure D.18: Calculated reflected power of Eccosorb MF-117 at a conductor radius ratio of 8.3 and frequencies from 1 GHz to 10 GHz.

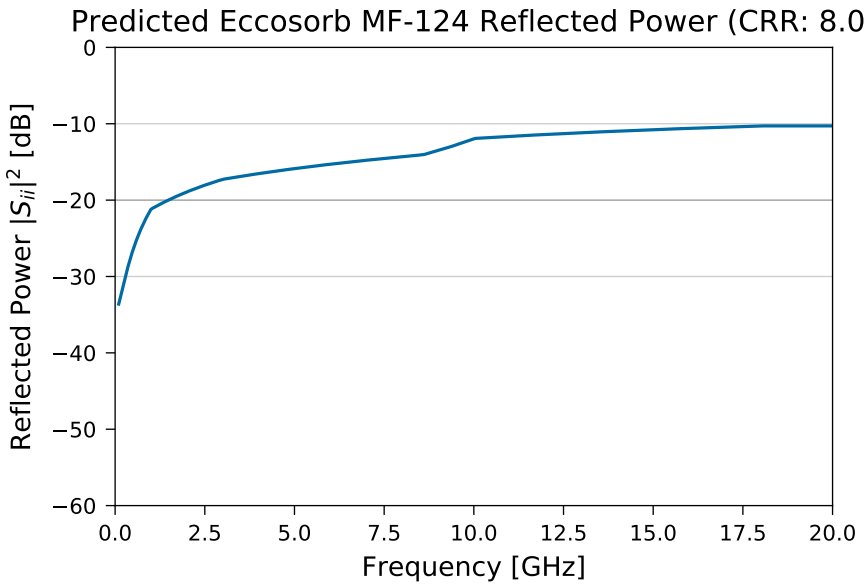

Figure D.19: Calculated reflected power of Eccosorb MF-124 at a conductor radius ratio of 8.0 and frequencies from 1 GHz to 10 GHz.

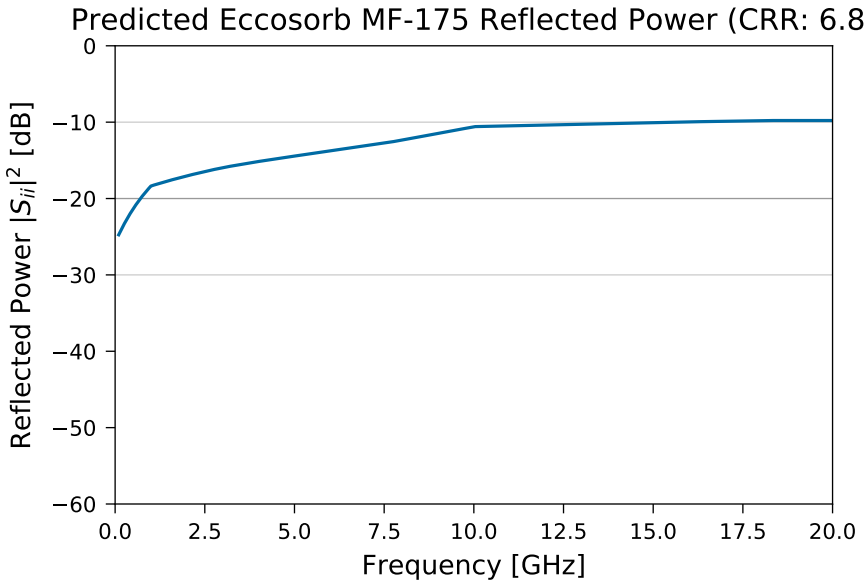

Figure D.20: Calculated reflected power of Eccosorb MF-175 at a conductor radius ratio of 6.8 and frequencies from 1 GHz to 10 GHz.

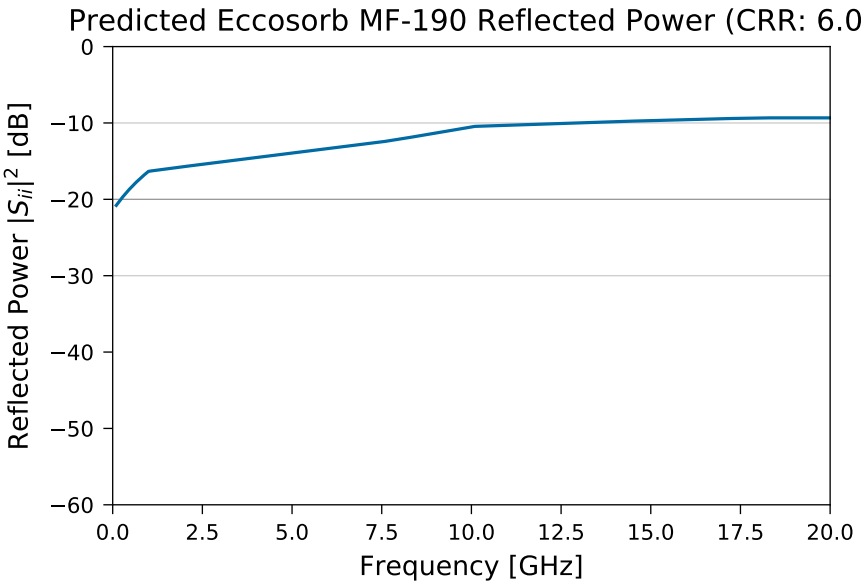

Figure D.21: Calculated reflected power of Eccosorb MF-190 at a conductor radius ratio of 6.0 and frequencies from 1 GHz to 10 GHz.

Appendix E

Thermal Photon Calculations

E.1 Theory of Continuous Beamsplitter Model

E.1.1 Temperature Calculations

The initial step in calculating the number of thermal photons is to calculate the temperature as a function of position of each of the cables. The most general possible way that we could do this would be to solve the heat equation:

$$\rho c_p \frac{\partial T}{\partial t} - \boldsymbol{\nabla} \cdot (\kappa \boldsymbol{\nabla} T) = \dot{q}_v \tag{E.1}$$

where ρ is the mass density of the material, c_p is the constant-pressure specific heat capacity of the material, T is the temperature, and $\dot{q}_v$ is the local volumetric heat flux (produced or consumed locally by say, chemical reactions or resistance) [27, p. 55].

However, this is somewhat complicated and beyond the scope of what we currently want to achieve, so I will start with the one-dimensional version of Fourier's law:

$$q(x) = -\kappa(T(x)) \frac{\mathrm{d}T}{\mathrm{d}x} \tag{E.2}$$

where $q(x)$ is the local heat flux in $\mathrm{W/m^2}$ and κ is the thermal conductivity of the material as a function of temperature (and hence position for a spatially varying temperature) in units of $\mathrm{W\,m^{-1}\,K^{-1}}$ [27, p. 10]. If we assume that there is no dissipation in the cable, then due to conservation of energy, the heat flux $q(x)$ must be independent of x and we have:

$$q \,\mathrm{d}x = -\kappa(T) \,\mathrm{d}T$$

or, in integral form:

$$\int q \,\mathrm{d}x = -\int \kappa(T) \,\mathrm{d}T,$$

which can be solved to give the heat flux in one cable:

$$q = \frac{1}{l} \int_{T_{\mathrm{cold}}}^{T_{\mathrm{hot}}} \kappa(T) \,\mathrm{d}T \tag{E.3}$$

where l is the length of the cable in meters and T_{hot} and T_{cold} are the temperature of the hot and cold side of the cable in Kelvins.

Using the heat fluxes, calculated using the above equation, we can solve Equation E.2 for the temperature profile using numerical methods. Next, we must address how the local temperature in the cable impacts the thermal photons that are present in the cable.

E.2 Continuous Beam Splitter Model

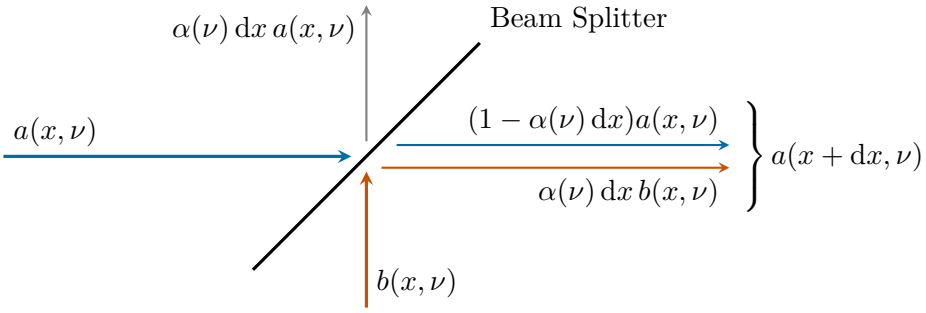

Figure E.1: Schematic of the continuous beam splitter model. Incoming photons in blue ($a(x,\nu)$), black body photons in red ($b(x,\nu)$), attenuated photons in gray ($\alpha(\nu)\,\mathrm{d}x\,a(x,\nu)$), output photons in both red and blue, reflecting the contribution of incoming and black body photons to the output.

I have provided the basic scheme of the continuous beam splitter model in Figure E.1 above. Focusing on an infinitesimal segment of cable of length $\mathrm{d}x$, we model the cable as a beam splitter. On one input port, we have $a(x,\nu)$, the photons that have reached the distance x down the cable. Some fraction of these, $\alpha(\nu)\,\mathrm{d}x$, are lost due to attenuation in this segment of the cable. The remaining fraction, $(1-\alpha(\nu)\,\mathrm{d}x)$, are transmitted to the output port. In addition to this, the cable produces local thermal black-body photons, $b(x,\nu)$. Due to the symmetry between absorption and emission, a fraction of these $\alpha(\nu)\,\mathrm{d}x$ are transmitted to the output port of the beam splitter. In this fashion, attenuation in the cable acts to "thermalize" the photons in the cable, reducing the number of photons produced by black body radiation elsewhere or intentionally added to the cable, replacing them with local black body photons.

By taking the output as the photon density at a position $x+\mathrm{d}x$, $a(x+\mathrm{d}x,\nu)$, we can convert the scheme above into a differential equation for the photon density,

$$a(x+\mathrm{d}x,\nu) = a(x,\nu) + [b(x,\nu) - a(x,\nu)]\alpha(\nu)\,\mathrm{d}x.$$

Rearranging, we get

$$\frac{a(x+\mathrm{d}x,\nu)-a(x,\nu)}{\mathrm{d}x}=b(x,\nu)-a(x,\nu),$$

which, in the limit of $\mathrm{d}x\to 0$ gives:

$$a'(x,\nu)+a(x,\nu)=b(x,\nu),$$

a first-order inhomogeneous differential equation with the solution:

$$a(x,\nu)=e^{-\alpha(\nu)x}\int_0^x \alpha(\nu)e^{\alpha(\nu)y}b(y,\nu)\,\mathrm{d}y+e^{-\alpha(\nu)x}C(\nu) \tag{E.4}$$

where $C(\nu)$ is a constant function of position. Taking $x=0$ reveals that $C(\nu)=a_0(\nu)$, the photons arriving at the beginning of the cable.

Now, we must link experimental parameters to the parameters in Equation E.4. The easiest way to do this is to ignore the black body photons. For a cable with an attenuation constant of $10\,\mathrm{dB\,m^{-1}}$ and a length of $1\,\mathrm{m}$, ten percent of the input photons should reach the end of the cable, *i.e.* $a(1,\nu)=\frac{1}{10}a_0(\nu)$. This gives:

$$\frac{1}{10}a_0(\nu)=e^{-\alpha(\nu)}a_0(\nu)$$

or $\alpha(\nu)=\log 10$. More generally, with an arbitrary attenuation in decibels per meter, $\beta(\nu)$,

$$\alpha(\nu)=\frac{\log 10}{10}\beta(\nu)$$

revealing that α is the attenuation in units of nepers per meter *and not* decibels per meter.

E.2.1 Black Body Photon Density

An important question when modeling the thermal photons of a coaxial cable is how to treat the black body photon density, in particular its dimensionality. In this case, because the electromagnetic modes of the coaxial cable are predominantly confined in one dimension and the length of the cable is generally long compared to the wavelength, I will treat the black body radiation density as a one-dimensional black body and treat the remaining degree of freedom by considering the number of modes present at each frequency. Following the method presented in [28], let us begin by assuming that we have a 1-D cavity of length L bounded by a perfectly conductive material. This boundary condition restricts the available wavelengths, requiring that $\omega_n=\frac{2\pi cn}{2L}$ where n indexes the available longitudinal modes. Treating each mode as a harmonic oscillator, we have that the energy of each mode is equal to

$$E_r=\left(r+\frac{1}{2}\right)\frac{hcn}{2L}$$

where r is an integer that denotes the number of excitations in each mode. Following the usual statistical physics procedures, the probability of being in any of the excitation levels, P_r, is:

$$P_r = \frac{e^{-\beta E_r}}{Z(\beta)}$$

where $\beta \equiv \frac{1}{k_B T}$ and $Z(\beta)$ is the partition function:

$$Z(\beta) \equiv \sum_{r=0}^{\infty} e^{-\beta E_r} = \frac{e^{-\frac{\beta}{2}\frac{hcn}{2L}}}{1 - e^{-\beta\frac{hcn}{2L}}}.$$

for a single mode n.

Denoting $\epsilon_n \equiv \frac{hcn}{2L}$, the average energy in a mode n, is given by the formula:

$$\langle E_n \rangle = -\frac{\partial \log(Z(\beta))}{\partial \beta} = \frac{\epsilon_n}{2} + \frac{\epsilon_n}{e^{\epsilon_n \beta} - 1},$$

where the Bose–Einstein distribution appears on the right-hand side. If we measure the energy relative to the ground state (which is reasonable since we can only ever measure energy differences), the total energy in the cavity is

$$U = \sum_{\mathrm{n}} \langle E_n \rangle - \frac{\epsilon_n}{2}.$$

As we take $L \to \infty$, the ϵ_n become continuous, and we can replace the sum above with an integral,

$$U = \int_0^{\infty} \frac{\epsilon}{e^{\epsilon\beta} - 1} g(\epsilon)\, \mathrm{d}\epsilon$$

where $g(\epsilon)$ is the density of states, which allows us to exchange an integral over modes for an integral over energy. $\epsilon = \frac{hc}{2L} n$, so $\mathrm{d}n = \frac{2L}{hc}\, \mathrm{d}\epsilon$ and $g(\epsilon) = \frac{2L}{hc}$. Therefore, the total internal energy in this cavity of length L is

$$U = \frac{2L}{hc} \int_0^{\infty} \frac{\epsilon}{e^{\epsilon\beta} - 1}\, \mathrm{d}\epsilon.$$

Per unit length, this becomes,

$$\frac{U}{L} = \frac{2}{hc} \int_0^{\infty} \frac{\epsilon}{e^{\epsilon\beta} - 1}\, \mathrm{d}\epsilon.$$

and so the spectral energy density, after converting the integral from energy to frequency, u_ν is given by:

$$u_\nu(T) = \frac{h^2 \nu}{hc} \frac{1}{e^{\frac{h\nu}{k_B T}} - 1}.$$

This light is emitted equally in both directions, and since we want to know the photons that pass through some imaginary surface in a given unit of time, we must multiply by the speed of light and divide by the number of directions that the light can be emitted into. Thus, the spectral radiance is

$$B_\nu(T) \equiv \frac{u_\nu(T)c}{2} = \frac{h\nu}{e^{\frac{h\nu}{k_B T}} - 1}$$

which has units of $\mathrm{J\,s^{-1}\,Hz^{-1}}$. Since for the calculations of the number of thermal photons, we care about the number of photons and not the power, we must divide by the energy of a single photon, $h\nu$, to get

$$B^P_\nu(T) = \frac{1}{e^{\frac{h\nu}{k_B T}} - 1},$$

the *photon flux spectral density* (Photon FSD or sometimes PFSD), in units of $\mathrm{photons\,s^{-1}\,Hz^{-1}}$. Again, in this one-dimensional case, the photon FSD is equivalent to the Bose–Einstein distribution.

To address the number of transverse modes that are available in the coaxial lines, I will then define the *coaxial black body photon flux spectral density* as

$$b(\nu, T) \equiv \frac{n(\nu)}{e^{\frac{h\nu}{k_B T}} - 1} \tag{E.5}$$

where $n(\nu)$ is a function that gives the number of modes available in the coaxial cable at frequency ν. This again has units of $\mathrm{photons\,s^{-1}\,Hz^{-1}}$.

E.2.2 Coaxial Higher-Order TE and TM Modes

We widely use coaxial cables to transmit microwave signals between two locations because they are very easy to use; up to a frequency determined by the geometry of the metal inner and outer conductors and the dielectric material, coaxial cables have only one mode, the TEM, or transverse electromagnetic mode. Above this frequency (usually called the *maximum frequency*, *moding frequency*, or *higher-order mode cutoff frequency*), however, coaxial cables have a number of TE (transverse electric) and TM (transverse magnetic) modes. According to [29], the solutions of the TM_{nm} modes are given by

$$J_n(ak)Y_n(bk) - J_n(bk)Y_n(ak) = 0 \tag{E.6}$$

while the TE_{nm} modes are given by

$$J'_n(ak)Y'_n(bk) - J'_n(bk)Y'_n(ak) = 0 \tag{E.7}$$

where J_n is the n-th order Bessel function of the first kind, J'_n is its derivative with respect to kx ($x = \{a, b\}$), Y_n is the n-th order Bessel function of the

second kind and Y_n' is its derivative, k is the wavenumber, b is the inner radius of the outer conductor, and a is the outer radius of the center conductor. The wavenumber solution is converted to frequency by

$$\nu = \frac{kc}{2\pi\sqrt{\epsilon_r}}$$

where c is the speed of light in a vacuum and ϵ_r is the relative dielectric constant. In both equations above, the m portion of the mode comes from taking the m-th solution of Equation E.6 or Equation E.7.

For the TE_{nm} modes, it is possible to describe the different modes somewhat intuitively. The n (azimuthal) parameter describes the number of times that the phase of the electric field winds around the center conductor. For example, for $n = 0$, the electric field will point inwards or outwards (but not both at the same time), for $n = 1$, one semicircle will have the electric field pointing inwards while the other semicircle will have the electric field pointing outwards. The m (radial) parameter describes the number of nodes in the electric field from the inner conductor to the outer conductor. For $m = 0$, the field points only in one direction radially, while for $m = 1$, the electric field will switch directions once radially. For the TM_{nm} modes, this sort of intuitive clarification is harder to give. The m parameter still describes the number of nodes in the magnetic field radially, but the n parameter is harder to describe.

E.3 Numerical Simulations

All numerical simulations were performed using Wolfram Mathematica. Currently, all simulation results are located in my USERS folder (`Q:▸USERS▸Graham▸Mathematica▸Simulations▸Bluefors Thermal Noise Photons`)

E.3.1 Coaxial Cable Properties

All information pertaining to the different types of coaxial cables that might be used in our lab are included in the `coaxialCableProperties.m` Mathematica library. This package depends on the group `ThermalCalculations` library. Inside, two main data structures are defined: `typeProperties` and `cableComponent`. `cableComponent` is a function that builds an association corresponding to a single part of a coaxial cable. Thus, it has an inner radius, an outer radius, and a material. The radii are given in meters and the materials are defined elsewhere in the document. `typeProperties` is a function that builds an association corresponding to a single type of coaxial cable. Thus, it has a name, a center conductor, a dielectric, an outer conductor, specified attenuation, specified higher-order mode frequencies, and a description. The cable names are based on manufacturer, cable type

(semirigid), nominal size, inner conductor material, dielectric material, and outer conductor material. `cableComponent`s are used for the inner conductor, dielectric, and outer conductor. Importantly, the attenuation and higher order mode frequencies are defined in the association as delayed-execution functions such that the data does not have to be available when the library is written, but is only required when the function is called for that specific cable type.

Materials within the `coaxialCableProperties` library are also associations in which the materials are given whatever properties are defined for them in `ThermalCalculations`, *e.g.* thermal conductivity, electrical resistivity, linear thermal expansion coefficient, specific heat capacity, and density. Dielectrics have dielectric constants and cutoff frequencies, to be discussed below.

In this way, `coaxialCableProperties` is a flexible library that can be used for a variety of numerical simulations and programming tasks related to fridge thermal design.

E.3.2 Cable Attenuation

For the attenuation of the coaxial cables, there is no specific notebook or library. Rather, the manufacturer specified attenuation of the cable type is stored in the main directory as a `csv` file with a name that correspons to the name of the cable type in `coaxialCableProperties`. Then the `loadAttenuationData` function of `coaxialCableProperties`, when it is called for this specific cable type, looks for this `csv` file and converts the data into a piecewise function of attenuation in dB versus frequency in GHz with linear interpolation between data points and a "clamping" of the attenuation at the highest (lowest) frequncy for all frequencies above (below) the limit value.

E.3.3 Coaxial Higher-Order Mode Minimum Frequencies

Table E.1: Micro-Coax UT-085SS-SS Properties

Parameter	**Value**
Center Conductor Outer Radius	0.255 mm
Outer Conductor Inner Radius	0.838 mm
Relative Dielectric Constant	2.03

The data in Table E.1, included in `coaxialCableProperties`, are sufficient to compute the frequencies of different modes in this coaxial cable. However, the dielectric of our cables, PTFE (commonly known as Teflon), can interact with these modes, absorbing or attenuating transmissions at

different frequencies. Fortunately, PTFE is widely used, and there are a number of studies of its properties in the far-infrared. Within this field, spectra are often presented in terms of the "spectroscopic" wavenumber, which is defined as $\tilde{\nu} \equiv \frac{1}{\lambda}$ where λ is the wavelength and $\tilde{\nu}$ is expressed in units of inverse cm. To convert to frequencies in Hz, the following formula can be used:

$$\nu = 100 \cdot c \cdot \tilde{\nu}$$

where c is the vacuum speed of light in $\mathrm{m\,s^{-1}}$.

Halpern *et al.* find that PTFE had negligible losses below $40\,\mathrm{cm^{-1}}$ (below 1200 GHz), the limits of their device [24]. Birch shows that, due to a strong absorption peak at $202\,\mathrm{cm^{-1}}$ (6060 GHz), PTFE becomes strongly attenuating above approximately $190\,\mathrm{cm^{-1}}$ (5700 GHz), with an attenuation coefficient greater than $20\,\mathrm{cm^{-1}}$ (without specifying if this is a Napierian or decadic coefficient) [31]. McCarthy also found that the transmission of a 1.6 mm sample of PTFE was negligible for wavenumbers between $190\,\mathrm{cm^{-1}}$ and $800\,\mathrm{cm^{-1}}$ (5700 GHz to 24 000 GHz) [32]. Therefore, I assume that the dielectric does not attenuate modes at all until 5700 GHz, when I assume that the absorption is so strong that no modes above this frequency propagate (hence I often refer to it as the dielectric cutoff frequency).

All calculations related to the number of higher order modes were performed in the `coaxial_mode_calculations.nb` notebook. The cutoff frequencies, the frequency at which a mode can begin propagating in the coaxial cable, of the different TM and TE modes were computed by numerically solving Equation E.6 and Equation E.7 for different orders n and considering all solutions up to frequencies beyond the upper limit set by the dielectric (thus including the different m modes). It was found to be important to give `NSolve` good bounds for the acceptable wavenumbers to reduce the time spent looking for solutions, and solutions using `ParallelTable` could still take several hours to find all solutions up to 6000 GHz for 0.085"-class cables (smaller cables with greater mode spacing are faster). The TE modes required orders, n, up to 150, while the TM modes required orders up to 70 to provide a buffer beyond the cutoff frequency of the dielectric. This notebook exports the cutoff frequencies for TE and TM as separate text files for use by `loadHigherOrderModeData` in `coaxialCableProperties`.

Plotting the number of modes available at different frequencies (Figure E.2) reveals quadratic behavior. This could be explained if, for example, the wavenumbers of different radial and azimuthal components are evenly spaced. Then, as the total wavenumber, which could be divided between these, increased, it would include quadratically more modes (see Figure E.3). *Note*: when fitting the number of modes, it is important to use a function of $a\nu^2 + b\nu + 1$ and not $a\nu^2 + b\nu + c$, as there is always at least one mode available in the coaxial cable.

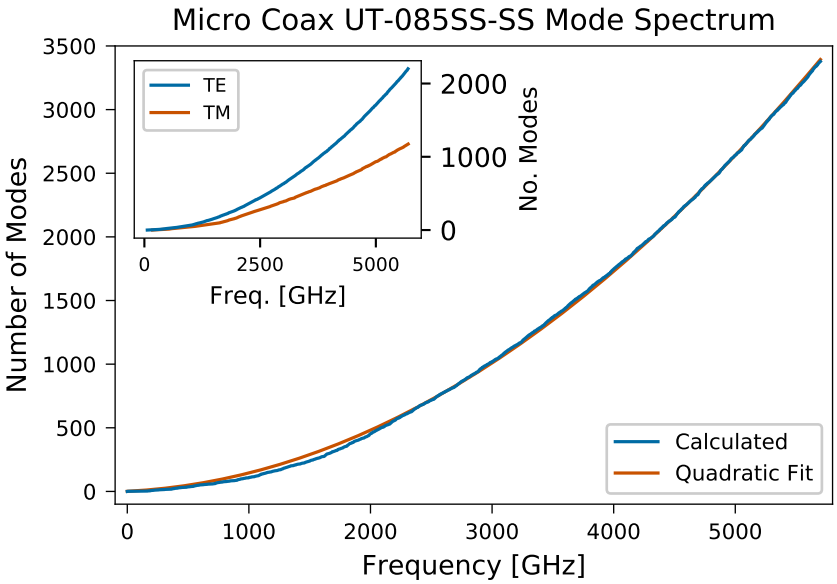

Figure E.2: Number of modes (TE_{nm} and TM_{nm}) available at different frequencies for a Micro-Coax UT-085SS-SS cable. Calculated data presented in blue, quadratic fit of the form $a\nu^2 + b\nu + 1$ presented in orange. *Inset*: Number of calculated TE (blue) and TM (orange) modes as a function of frequency. Both TE and TM modes show quadratic dependence on frequency.

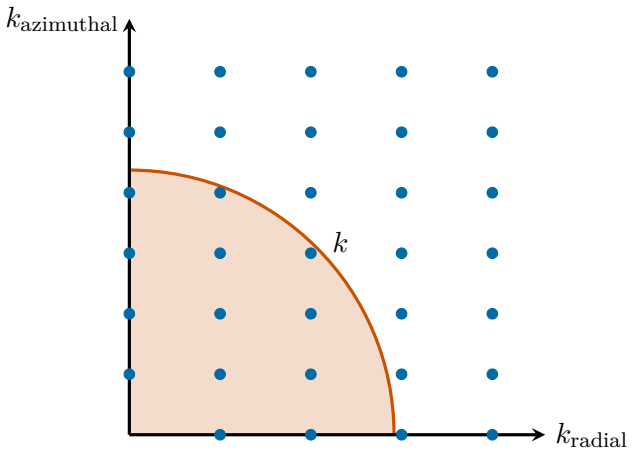

Figure E.3: Rough image of motivation for finding a quadratically increasing number of modes. Possible modes plotted as blue dots, available wavenumber range plotted in red-orange.

E.3.4 Main Simulation

Table E.2: Stage parameters for numerical simulation. Cable length is from the previous stage to the current stage.

Stage	Temperature [K]	Cable Length [m]	Attenuator
0	293		
1	45	0.226	
2	3	0.321	XMA 20 dB
3	0.9	0.280	
4	0.100	0.199	XMA 20 dB
5	0.010	0.198	
6	0.010	0.300	XMA 20 dB

The main simulation is contained in `bluefors_coaxial_thermal_photons_simulation.nb` and which relies heavily on the `CoaxialThermalPhotonCalculations` library. Here, the input data structure is a list of associations called `stageParameters` that has a temperature, cable length, cable type, and attenuator for each stage (included above in Table E.2). Importantly, cable length is the length from stage $n-1$ to stage n (*i.e.* stage 0 is just present to provide the room temperature boundary condition). The cable lengths above were chosen to correspond to those predicted for the BlueFors XLD system and all cables are assumed to be Micro-Coax UT-085SS-SS semi-rigid coaxial cable, which has the properties listed in Table E.1 [30].

In the beginning, I solve for the temperature profile of each of the cables using `cableTemperatureSolution`. This function first solves for the heat flux in each cable using Equation E.3 and `NIntegrate` (`heatFlux`). Then, it solves Equation E.2 using this flux (and assuming that it is the same at all points in the cable, based on conservation of energy) with `NDSolve` (`temperatureProfile`). The temperature profile of the first cable from stage 0 (293 K) to stage 1 (45 K) is plotted in Figure E.4. The calculated temperature profile is nonlinear because the thermal conductivity of 304 stainless steel is not constant across this temperature range. Similarly nonlinear results hold for all of the stages with a finite temperature difference.

With this data, I can finally solve for the photon densities at the different stages using Equation E.4 and other equations from the continuous beam splitter model section. From the temperature profile, I can calculate the local blackbody photon flux spectral density (`blackbodyPhotonDensity`), the photon FSD in a coaxial cable (`cablePhotonDensity`), and the photon FSD in an attenuator (`attenuatorPhotonDensity`). These functions are wrapped in a higher level function, `stageCalculation`, which automates inserting the correct arguments and parsing `coaxialCableProperties` for the correct parameters. Finally, `stageCalculation` itself is wrapped in

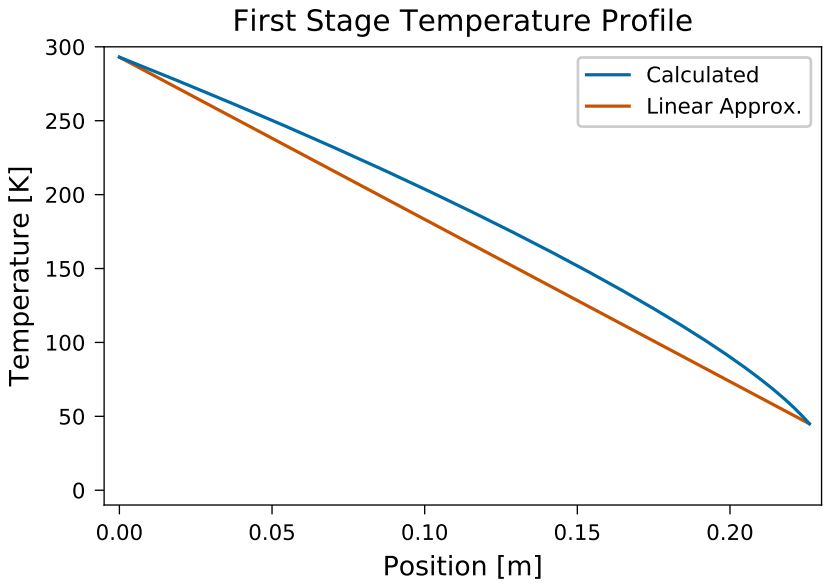

Figure E.4: Temperature profile for the cable from stage 0 (293 K) to stage 1 (45 K). Calculated profile in blue, linear approximation in red-orange. Calculated profile is non-linear due to non-constant temperature dependence of $\kappa(T)$ for 304 stainless steel.

the highest-level function, `calculateStagePhotonDensities` so that users only have to provide the `stageParameters` list in order to perform calculations. For more information, look at the library usage information or `coaxial_tpc_testing.nb`.

One note is that calculations using the calculated temperature profile, calculated number of modes, and specified attenuation are extremely slow (taking more than an hour just to plot the PFSD from 1 GHz to 5700 GHz). This is probably due to the fact that my current simulations are entirely functional, always passing functions on, and thus the overhead of function calls rapidly builds up. However, in order to make the calculations faster, there is an approximate version that assumes constant attenuation, a linear temperature profile between stages, and a quadratic form for the mode spectrum. For the number of modes at a given frequency, the quadratic fit is quite close to the calculated data (see Figure E.2), with a region where the quadratic fit overestimates the data somewhat between 800 GHz and 2000 GHz. The temperature profile shows the largest difference. The non-linear profile increases the average temperature of the calculated versus the linear temperatures. For example, for the first cable, as shown in Figure E.4, the average calculated temperature is 185 K, while the average

linear temperature is 124 K. This means that the approximate calculations will under-estimate the actual number of blackbody photons.

A comparison between the calculated and the approximate methods (temperature, attenuation, number of modes) is presented in Figure E.5. The approximate methods overestimate the photon FSD at frequencies up to 1800 GHz and then underestimate the photon FSD. The overestimate at intermediate frequencies may be due to the difference in the number of modes between the calculated values and the quadratic fit. At high frequencies, the underestimate is largely due to the difference in average temperatures between the exact and approximate methods. The difference between the normal and the approximate methods in the number of photons between the gap energy of aluminum and the cutoff frequency of the dielectric is roughly 10%, well within the order-of-magnitude estimate that we are seeking.

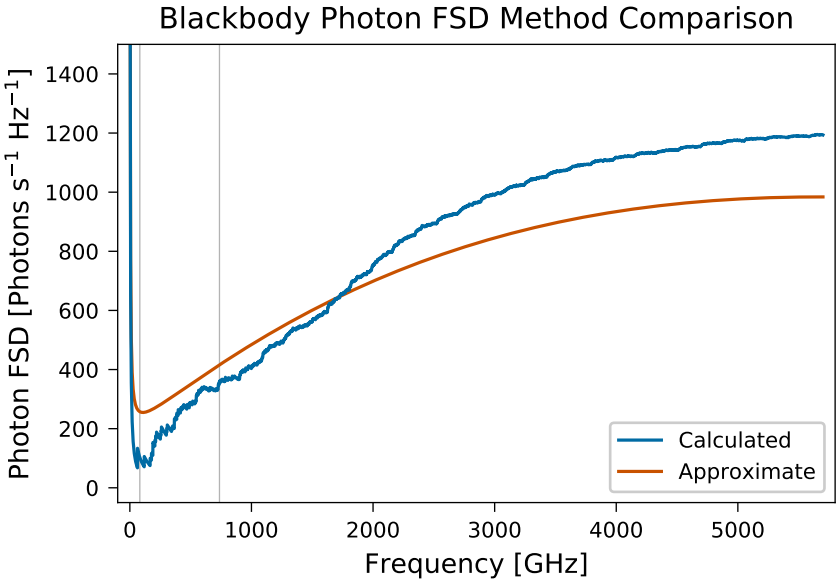

Figure E.5: Comparison of calculated and approximate methods for producing the blackbody photon flux spectral density. Temperature corresponds to the temperature 10 cm into the first cable. Calculated results plotted in blue, approximate results plotted in red-orange. Vertical gray bars are the frequencies corresponding to the gap energies of aluminum (*left*) and niobium (*right*).

The divergent photon flux spectral density at zero frequency visible in Figure E.5 (and other photon density plots below) is physical. Although, at low frequencies, the interstage cable length may not be significantly greater than the wavelength, our cables are not shorted at the ends, but continue on or are 50 Ω terminated. Thus, we work in the semi-infinite cable regime, and the cables are electrically long even at low wavelengths. This divergence in

photon comes purely from the one-dimensionality of the coaxial cable at low frequencies. However, since the power in these photons also scales as $h\nu$, an infinite number of photons at 0 Hz corresponds to a fixed DC offset.

In Figure E.6, the photon FSD is plotted at the end of the cable from stage 0 to stage 1, using the precise computed functions and the approximate functions, discussed above, for the number of modes, the temperature profile of the cable, and the attenuation of the cable. The photon FSD is reduced slightly compared to the blackbody plot above (Figure E.5), but the same general features are present. The difference between the specified attenuation and the approximate attenuation should only matter for frequencies below 50 GHz, which we ignore.

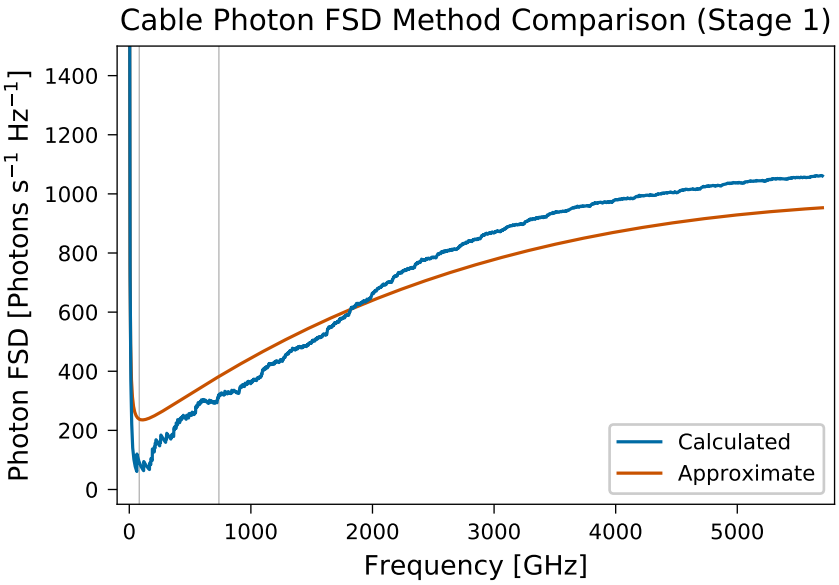

Figure E.6: Comparison of photon flux spectral density at the end of the cable from stage 0 to stage 1 when using the computed and the approximate functions for the number of modes, temperature, and cable attenuation. Calculated results plotted in blue, approximate results plotted in red-orange. Vertical gray bars are the frequencies corresponding to the gap energies of aluminum (*left*) and niobium (*right*).

Some stages also have XMA resistive attenuators. I currently assume that they attenuate by the stated value at all frequencies. They are rated to at least 50 GHz, but it is not clear how they behave at higher frequencies. The resistive elements inside these filters (for an example discussing the construction of these cryogenic filters, see [33]) should continue to function, but stray capacitances might allow the filter to become transparent at high frequencies.

E.3.5 Summary of Assumptions

These calculations have a number of limitations, so I think that it is good to be very clear about the assumptions that I make in order to be clear about the domain of validity of the simulation.

1. General Assumptions
   (a) *Coaxial cables are perfectly thermalized.* Inner and outer conductor have the same temperature, and the temperature at the ends of the cable corresponds to the stage temperatures.
   (b) *Local heat flux due to dissipation of signal photons can be ignored.* Difficult to include in a general manner and this will mostly matter at high-temperature stages. The only sources of heat for the cable are the two stages to which it is connected.
   (c) *Coaxial cable only acts as 1D conductor.* Needed to treat the blackbody photon density from a 1D object with a number of modes.
   (d) *Each TE and TM mode does not propagate at all below its cutoff frequency and propagates without loss above its cutoff frequency.* The only source of attenuation is that specified by the cable manufacturer.
   (e) *Coaxial cable is much longer than the wavelength.* Required to make the sum to integral transition. Usually fulfilled becuase signal generators, etc. are all $50\,\Omega$ terminated, meaning that they act as a semi-infinite cable.
   (f) *Attenuation of coaxial cable at high frequencies is equivalent to attenuation for highest specified frequency.* Data beyond this frequency is unknown. Assuming that it remains constant appears to be the safest option.
   (g) *Dielectric does not attenuate signal below its cutoff frequency and completely absorbs photons above its cutoff frequency.*
   (h) *XMA attenuators are perfectly broadband.* Performance outside the specified range is unknown
   (i) *Electric field couples equally at all points.* No standing waves, *etc.* that would change how the blackbody photons are emitted into the cable.
2. Performance Assumptions (Approximate Methods)
   (a) *Cable has equal attenuation at all frequencies.* Used to speed up simulation.
   (b) *Temperature profile can be approximated as linear.* Used to speed up calculation.

(c) *Number of modes can be approximated by a quadratic fit of the form* $a\nu^2 + b\nu + 1$. Used to speed up calculation.

E.3.6 Results

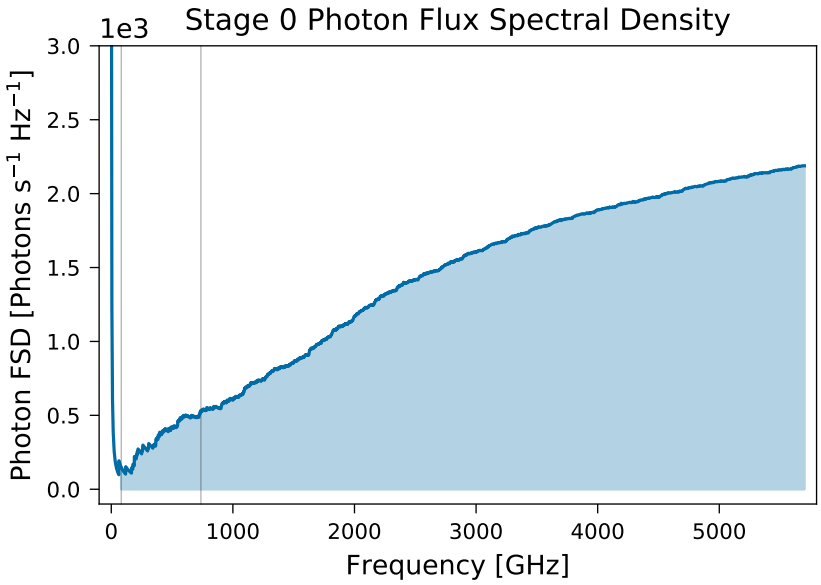

Figure E.7: Spectral density of photon flux at stage 0 (input to dilution refrigerator, 293 K). Vertical gray bars are the frequencies corresponding to the gap energies of aluminum (*left*) and niobium (*right*).

The stage 0 photon flux spectral density, Figure E.7, shows the input blackbody radiation photon density. Due to the one-dimensional nature of the system, the photon FSD diverges at low frequencies and then increases with a characteristic shape due to the interaction of the quadratic number of modes term with the exponential term in the denominator of Equation E.5. The photon FSD at this stage is in the thousands of photons $\mathrm{s}^{-1}\,\mathrm{Hz}^{-1}$.

Cable attenuation brings the stage 1 photon FSD (Figure E.8) down to hundreds of photons $\mathrm{s}^{-1}\,\mathrm{Hz}^{-1}$. However, the overall picture is similar to stage 0.

Stage 2 brings the first significant difference. With a 20 dB attenuator present, this stage starkly reduces the number of photons present (to roughly 1 % of the previous value) while adding black body photons at a temperature of 3 K, causing the sharp peak of photon density to move from the left of the aluminum gap energy line to the right of it. The photon FSD is down to single photons $\mathrm{s}^{-1}\,\mathrm{Hz}^{-1}$.

Stages 3 (Figure E.10), 4 (Figure E.11), 5 (Figure E.12), and 6 (Figure E.13) largely display the same behavior as the stage 2 photon density,

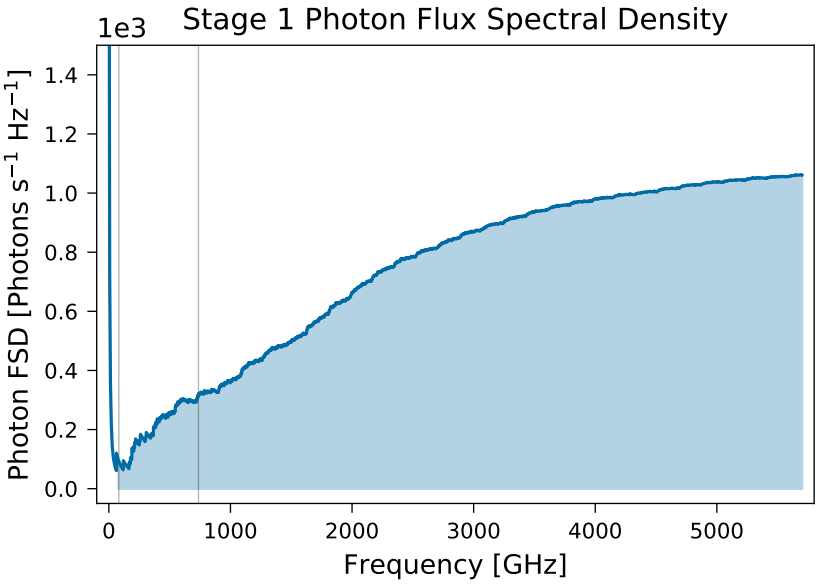

Figure E.8: Spectral density of photon flux at stage 1 (45 K). Vertical gray bars are the frequencies corresponding to the gap energies of aluminum (*left*) and niobium (*right*).

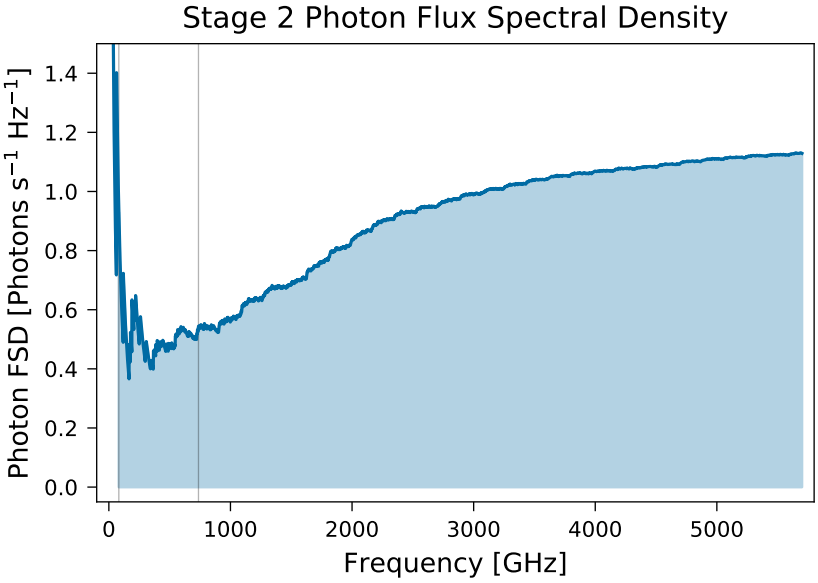

Figure E.9: Spectral density of photon flux at stage 2 (still, 3 K). Vertical gray bars are the frequencies corresponding to the gap energies of aluminum (*left*) and niobium (*right*).

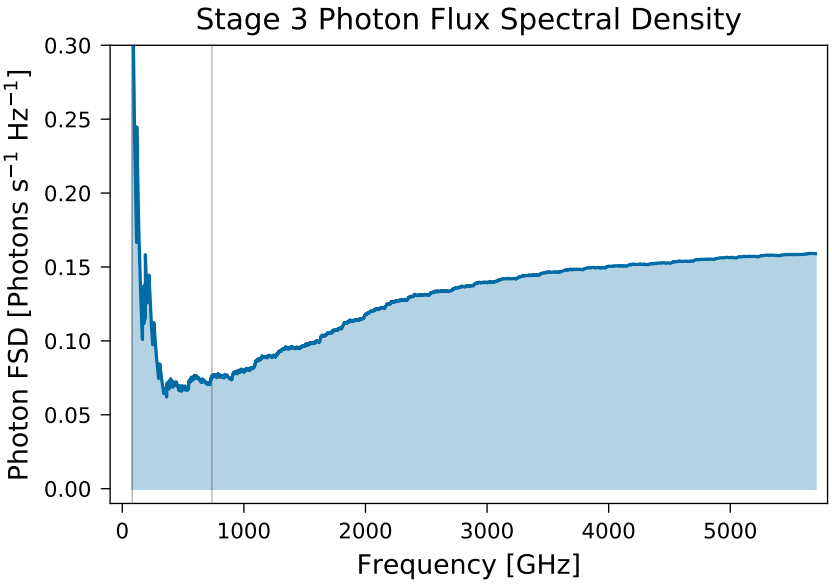

Figure E.10: Spectral density of photon flux at stage 3 (0.9 K). Vertical gray bars are the frequencies corresponding to the gap energies of aluminum (*left*) and niobium (*right*).

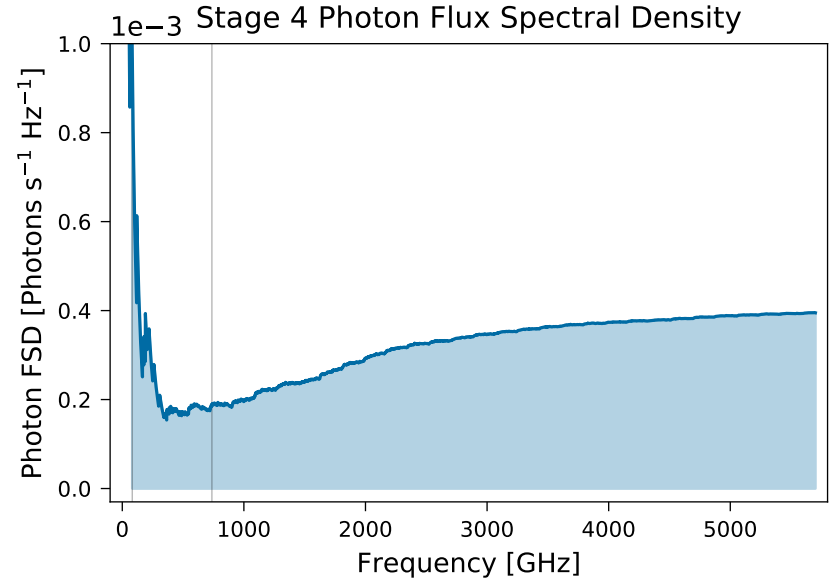

Figure E.11: Spectral density of photon flux at stage 4 (100 mK). Vertical gray bars are the frequencies corresponding to the gap energies of aluminum (*left*) and niobium (*right*).

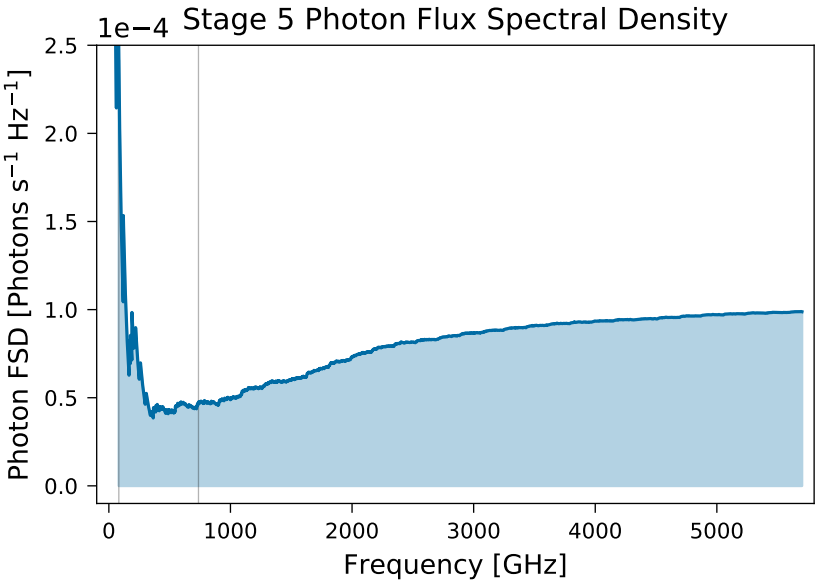

Figure E.12: Spectral density of photon flux at stage 5 (base plate, 10 mK). Vertical gray bars are the frequencies corresponding to the gap energies of aluminum (*left*) and niobium (*right*).

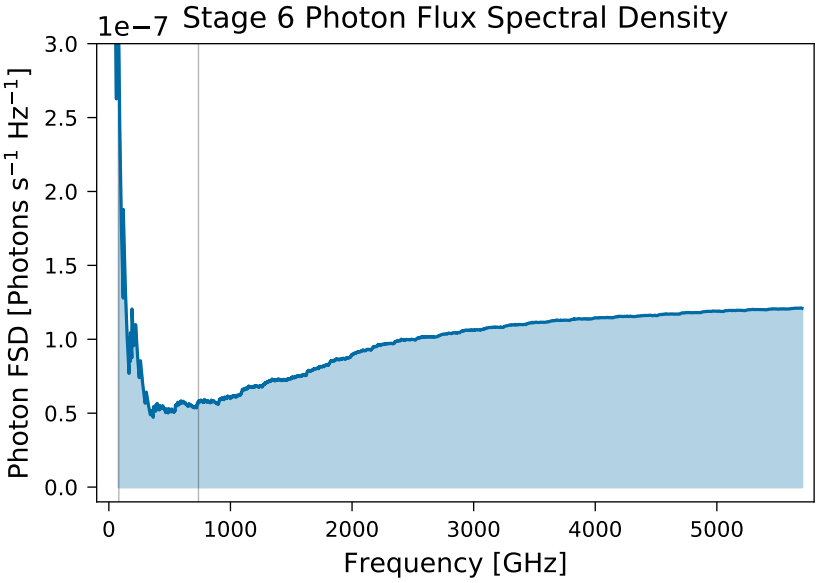

Figure E.13: Spectral density of photon flux at stage 6 (sample, 10 mK). Vertical gray bars are the frequencies corresponding to the gap energies of aluminum (*left*) and niobium (*right*).

but with ever-decreasing photon FSDs. By stage 6, the photon FSD has been reduced to hundreds of nphotons s^{-1} Hz^{-1}. Final photon number and photon power calculations reveal that the total number of thermal photons between the gap-energy frequency of aluminum and the cutoff frequency of the PTFE dielectric are in the order of 500 000 photons per second (see Table E.3). Based on this result, I can say that, assuming all of the assumptions made above hold, Eccosorb filters are crucial for rejecting thermal photons.

With these calculations it is also possible to test a more pessimistic experimental setup. Assuming that the center conductor is not perfectly thermalized at the low temperature stages, but remains at 100 mK, this could be modeled by specifying the base-plate and sample temperature, as say 50 mK. Simulations that encompassed these parameters showed an increase in the number of quasiparticle-inducing thermal photons from $5.2 \times 10^5\,s^{-1}$ previously to $5.3 \times 10^5\,s^{-1}$ in this case (approximate calculations). Therefore, the majority of the quasiparticle inducing photons arrive at the sample due to insufficient attenuation rather than insufficient thermalization of the cables, at least, according to my results.

Table E.3: Number and power of photons between gap-energy frequency of aluminum and cutoff frequency of PTFE dielectric

Stage	**Photon Number [photons s^{-1}]**	**Photon Power [W]**
Input	7.9×10^{15}	1.9×10^{-5}
Sample	5.5×10^{5}	1.2×10^{-15}

In general, the approximate and "exact" methods produce similar final results. The approximate estimated the photon flux density at the sample to within 6% of the value of the more rigorous calculations. However, the "exact" methods took 20 times longer to complete (5064 vs. 25 seconds to plot the final stage photon FSD). Therefore, I recommend using the approximate methods when possible, as this minor difference is well within the uncertainty due to the other assumptions.

Bibliography

[1] M. H. Devoret, A. Wallraff, and J. M. Martinis. *Superconducting Qubits: A Short Review*. Version 1. Nov. 7, 2004. arXiv: cond-mat/0411174v1 [cond-mat.mess-hall].

[2] Charles Kittel. *Introduction to solid state physics*. 7th ed. John Wiley & Sons, Inc., 1996. Chap. 12. ISBN: 0-471-1181-3.

[3] D. Risté, C. C. Bultink, M. J. Tiggelman, R. N. Schouten, K. W. Lehnert, and L. DiCarlo. "Millisecond charge-parity flucuations and induced decoherence in a superconducting transmon qubit". In: *Nature Communications* 4 (May 28, 2013), p. 1913. DOI: 10.1038/ncomms2936.

[4] L. Sun, L. DiCarlo, M. D. Reed, G. Catelani, Lev S. Bishop, D. I. Schuster, B. R. Johnson, Ge A. Yang, L. Frunzio, L. Glazman, M. H. Devoret, and R. J. Schoelkopf. "Measurements of Quasiparticle Tunneling Dynamics in a Band-Gap-Engineered Transmon Qubit". In: *Physical Review Letters* 108 (June 8, 2012), p. 230509. DOI: 10.1103/PhysRevLett.108.230509.

[5] G. Catelani, J. Koch, L. Frunzio, R. J. Schoelkopf, M. H. Devoret, and L. I. Glazman. "Quasiparticle Relaxation of Superconducting Qubits in the Presence of Flux". In: *Physical Review Letters* 106 (Feb. 18, 2011), p. 077002. DOI: 10.1103/PhysRevLett.106.077002.

[6] J. M. Kreikebaum, A. Dove, W. Livingston, E. Kim, and I. Siddiqi. "Optimization of infrared and magnetic shielding of superconducting TiN and Al coplanar microwave resonators". In: *Superconductor Science and Technology* 29 (Aug. 12, 2016). DOI: 10.1088/0953-2048/29/10/104002.

[7] R. Barends, J. Wenner, M. Lenander, Y. Chen, R. C. Bialczak, J. Kelly, E. Lucero, P. O'Malley, M. Mariantoni, D. Sank, H. Wang, T. C. White, Y. Yin, J. Zhao, A. N. Cleland, John M. Martinis, and J. J. A. Baselmans. "Minimizing quasiparticle generation from stray infrared light in superconducting quantum circuits". In: *Applied Physics Letters* 99 (Sept. 13, 2011), p. 113507. DOI: 10.1063/1.3638063.

[8] Jeffrey Scott Birenbaum. "The C-Shunt Flux Qubit: A New Generation of Superconducting Flux Qubit". PhD. Thesis. University of California, Berkeley, 2014. eprint: http://eprints.cdlib.org/uc/item/3gg7j6rh.

[9] Fei Yan, Simon Gustavsson, Archana Kamal, Jeffrey Birenbaum, Adam P. Sears, David Hover, Ted J. Gudmundsen, Danna Rosenberg, Gabriel Samach, S. Weber, Jonilyn L. Yoder, Terry P. Orlando, John Clarke, Andrew J. Kerman, and William D. Oliver. "The flux qubit revisited to enhance coherence and reproducibility". In: *Nature Communications* 7 (Nov. 3, 2016), p. 12964. DOI: 10.1038/ncomms12964.

[10] D. Vion, P. F. Orfila, P. Joyez, D. Esteve, and M. H. Devoret. "Miniature electrical filters for single electron devices". In: *Journal of Applied Physics* 77 (Mar. 15, 1995), pp. 2519–2524. DOI: 10.1063/1.358781.

[11] John M. Martinis, Michael H. Devoret, and John Clarke. "Experimental tests for the quantum behavior of a macroscopic degree of freedom: The phase difference across a Josephson Junction". In: *Physical Review B* 35 (Apr. 1, 1987), pp. 4682–4698. DOI: 10.1103/PhysRevB.35.4682.

[12] Christopher Eichler. "Experimental Characterization of Quantum Microwave Radiation and its Entanglement with a Superconducting Qubit". PhD. Thesis. ETH Zürich, 2013. eprint: http://e-collection.library.ethz.ch/view/eth:6886.

[13] K. Bladh, D. Gunnarsson, E. Hüfeld, S. Devi, C. Kristoffersson, B. Smålander, S. Pehrson, T. Claeson, and P. Delsing. "Comparison of cryogenic filters for use in single electronics experiments". In: *Review of Scientific Instruments* 74 (Mar. 2003), pp. 1323–1327. DOI: 10.1063/1.1540721.

[14] E. J. Wollack, D. J. Fixsen, R. Henry, A. Kogut, M. Limon, and P. Mirel. "Electromagnetic and Thermal Properties of a Conductively Loaded Epoxy". In: *Journal of Infrared, Millimeter, and Terahertz Waves* 29 (Oct. 27, 2007), pp. 51–61. DOI: 10.1007/s10762-007-9299-4.

[15] D. F. Santavicca and D. E. Prober. "Impedance-matched low-pass stripline filters". In: *Measurement Science and Technology* 19 (June 30, 2008), p. 087001. DOI: 10.1088/0957-0233/19/8/087001.

[16] Michael Fang. "Development of Hardware for Scaling Up Superconducting Qubits and Simulations of Quantum Chaos". Bachelor's Honor Thesis. University of California, Santa Barbara, June 12, 2015.

[17] Michael Peterer. "Investigating the suppression of external sources of decoherence on transmon qubits". Master's Thesis. ETH Zürich, June 17, 2012.

[18] Mintu Mondal and Yves Salathé. "Impedance-matched coaxial low-pass Eccosorb filters". Mar. 29, 2016.

[19] David M. Pozar. *Microwave Engineering*. 4th ed. J. Wiley & Sons, Inc., 2012. ISBN: 978-0-470-63155-3.

[20] *Eccosorb CR. Two Part Castable Load Absorber Series*. Technical Bulletin. Laird Technologies, Inc. URL: http://www.eccosorb.com/Collateral/Documents/English-US/CR.pdf (visited on Feb. 17, 2017).

[21] *Eccosorb MF. Lossy, Magnetically Loaded, Machinable Stock*. Technical Bulletin. Laird Technologies, Inc. URL: http://www.eccosorb.com/Collateral/Documents/English-US/RFP-DS-MF%20092115.pdf (visited on Feb. 17, 2017).

[22] Eino J. Luoma. *Energy propagation in dielectric and magnetic materials*. Laird Technologies, Inc. 1977. URL: http://www.eccosorb.eu/energy-propagation-dielectric-and-magnetic-materials (visited on Feb. 20, 2017).

[23] *Eccosorb MFS. High-Loss, Non-Rigid, Magnetically Loaded Stock*. Technical Bulletin. Laird Technologies, Inc. URL: http://www.eccosorb.com/Collateral/Documents/English-US/RFP-DS-MFS%20100915.pdf (visited on Feb. 20, 2017).

[24] Mark Halpern, Herbert P. Gush, Edward Wishnow, and Vittorio De Cosmo. "Far infrared transmission of dielectrics at cryogenic and room temperatures: glass, Fluorogold, Eccosorb, Stycast, and various plastics". In: *Applied Optics* 25.4 (Feb. 15, 1986), pp. 565–570. DOI: 10.1364/AO.25.000565.

[25] Hamid Hemmati, John C. Mather, and William L. Eichorn. "Submillimeter and millimeter wave characterization of absorbing materials". In: *Applied Optics* 24.24 (Dec. 15, 1985), pp. 4489–4492. DOI: 10.1364/AO.24.004489.

[26] Patrick Wikus, Kevin A. McCarthy, Scott A. Hertel, Yelena S. Bagdasarova, Enectalí Figueroa-Feliciano, Steven W. Leman, John M. Rutherford, Sarah N. Trowbridge, and Scott W. Vasquez. "The specific heat and thermal conductivity of Eccosorb CR-124 between 800 mK and 6 K". In: *Cryogenics* 49.8 (Aug. 2009), pp. 421–424. DOI: 10.1016/j.cryogenics.2009.06.002.

[27] John H. Lienhard IV and John H. Lienhard V. *A Heat Transfer Textbook*. 4th ed. Cambridge, Massachusetts, U.S.A.: Phlogiston Press, Jan. 8, 2017. URL: http://ahtt.mit.edu (visited on Mar. 9, 2017).

[28] *Planck's Law*. Wikimedia Foundation, Inc. URL: https://en.wikipedia.org/wiki/Planck%27s_law (visited on Apr. 24, 2017).

[29] Stellan Ekberg. *Mathematical analysis of coaxial cables*. Göteborg: Elander, 1956.

[30] *UT-085SS-SS Specifications*. Revision B1. Micro-Coax, Inc. 206 Jones Blvd., Pottstown, PA 19464, U.S.A.

[31] J. R. Birch. "The far-infrared optical constants of polypropylene, PTFE and polystyrene". In: *Infrared Physics* 33.1 (1992), pp. 33–38. DOI: 10.1016/0020-0891(92)90052-U.

[32] M. E. McCarthy. "Reflection and Transmission Measurements in the Far Infrared". In: *Applied Optics* 10.11 (Nov. 1971), pp. 2539–2541. DOI: 10.1364/AO.10.002539.

[33] Jen-Hao Yeh, Jay LeFebvre, Shavindra Premaratne, F. C. Wellstood, and B. S. Palmer. "Microwave attenuators for use with quantum devices below 100 mK". In: *ArXiv e-prints* (Mar. 3, 2017). arXiv: 1703.01285 [physics.ins-det].

Colophon

This document was typeset in 11 point Latin Modern using LaTeX2e, a typesetting system based on Leslie Lamport's LaTeX, which is a collection of macros to make working with Donald Knuth's TeX typesetting and layout engine easier. Compilation was performed with Hàn Thế Thành's pdfLaTeX which adds a large number of microtypographic improvements to the output text.

Figures were prepared using matplotlib version 2.0.0, python 3.4, and Tableau's Color Blind 10 color scheme or the Viridis color map included with matplotlib.